

INAUGURAL - DISSERTATION

submitted to the
Combined Faculties for the Natural Sciences and for Mathematics
of the Ruperto-Carola University of Heidelberg, Germany
for the degree of
Doctor of Natural Sciences

Put forward by
Dipl.-Phys. Moritz Bernhard Mie
born in Kiel

Oral examination: June 15, 2011

Quantification of Brain Tissue Oxygenation:
Comparison of Different Gradient Echo/Spin Echo
MRI Techniques at 3 Tesla

Referees: Prof. Dr. Lothar Schad
Prof. Dr. Peter Bachert

To my parents

Quantification of Brain Tissue Oxygenation: Comparison of Different Gradient Echo/Spin Echo MRI Techniques at 3 Tesla

In this work, an established tissue model was used to calculate the venous blood fraction (λ), the irreversible relaxation rate (R_2) and the reversible relaxation rate (R'_2) on the basis of a three-parameter fit of the MR signal (white matter: $\lambda = (1.9 \pm 0.9) \%$, $R_2 = (14.9 \pm 1.4) \text{ Hz}$, $R'_2 = (2.3 \pm 0.7) \text{ Hz}$; gray matter: $\lambda = (2.8 \pm 2.1) \%$, $R_2 = (11.6 \pm 3.2) \text{ Hz}$, $R'_2 = (3.5 \pm 2.4) \text{ Hz}$). These parameters enable the quantification of the susceptibility difference ($\Delta\chi$) between venous blood and surrounding tissue and, therewith, the oxygen extraction fraction (OEF, white matter: $(42.9 \pm 16.3) \%$; gray matter: $(43.9 \pm 14.4) \%$). The focus of this work was on the development of different methods to reduce the number of required fit parameters by separate measurements of the parameters to increase the fit accuracy. This was achieved with a separate calculation of the cerebral blood volume (CBV) by a dynamic susceptibility contrast (DSC) measurement. This value could be used as an input parameter of the signal equation resulting in a two-parameter fit. This method yielded OEF values of $(37.5 \pm 4.6) \%$ in healthy white matter and $(27.8 \pm 4.3) \%$ in tumorous brain tissue. Another approach was the determination of the other two other parameters (R_2 and R'_2) in separate measurements (white matter: $R_2 = (14.4 \pm 0.8) \text{ Hz}$, $R'_2 = (7.3 \pm 1.4) \text{ Hz}$; gray matter: $R_2 = (12.8 \pm 1.8) \text{ Hz}$, $R'_2 = (8.0 \pm 2.2) \text{ Hz}$) and a subsequent correction and validation using different phantom measurements. This technique was finally employed for *in vivo* experiments. The separate fitting approach promises a high fit certainty and yielded OEF values of $(22.0 \pm 3.4) \%$ and $(26.9 \pm 6.5) \%$ for white and gray matter, respectively. In this work, another method for OEF calculation is described based on the separation of the signal components originating from the veins from the remaining signal. The subsequent measurement of the transverse relaxation rate - $(13.1 - 18.9) \text{ Hz}$ in the investigated regions - and a calibration of the oxygenation level enable the OEF calculation. Furthermore, susceptibility weighted imaging (SWI), a method with an imaging contrast depending on the oxygenation status of the veins, was transferred from brain to renal imaging. The implemented technique improved the average contrast-to-noise ratio by 33% compared to the standard SWI method. After the reconstruction of SWI images of the kidneys, the change of the contrast due to oxygenation variation was qualitatively observed.

The presented methods yielded promising results for the determination of the OEF, which is an indicator for tissue viability. This determination might be used in radiotherapy for irradiation planning and therapy monitoring.

Quantifizierung der Gewebeoxygenierung im Gehirn: Vergleich von unterschiedlichen MRI-Gradientenecho/Spinecho-Techniken bei 3 Tesla

In dieser Arbeit wurde ein etabliertes Gewebemodell benutzt, um das venöse Blutvolumen (λ), die irreversible Relaxationsrate (R_2) und die reversible Relaxationsrate (R'_2) mit Hilfe eines Drei-Parameter-Fits des MR-Signals zu berechnen (weiße Hirnsubstanz: $\lambda = (1.9 \pm 0.9) \%$, $R_2 = (14.9 \pm 1.4) \text{ Hz}$, $R'_2 = (2.3 \pm 0.7) \text{ Hz}$; graue Hirnsubstanz: $\lambda = (2.8 \pm 2.1) \%$, $R_2 = (11.6 \pm 3.2) \text{ Hz}$, $R'_2 = (3.5 \pm 2.4) \text{ Hz}$). Diese Parameter ermöglichen die Quantifizierung des Suszeptibilitätsunterschieds ($\Delta\chi$) zwischen venösem Blut und dem umgebenen Gewebe, und damit des Sauerstoffextraktionsanteils (OEF, weiße Hirnsubstanz: $(42.9 \pm 16.3) \%$; graue Hirnsubstanz: $(43.9 \pm 14.4) \%$). Der Fokus dieser Arbeit lag auf der Entwicklung verschiedener Methoden, um die Anzahl der benötigten Fitparameter durch separate Parametermessungen zu reduzieren und damit die Fitgenauigkeit zu erhöhen. Dies wurde durch eine separate Berechnung des zerebralen Blutvolumens (CBV) durch eine dynamische Suszeptibilitätskontrast-Messung (DSC) erreicht. Dieser Wert konnte als Inputparameter für die Signalgleichung verwendet werden, was zu einem Zwei-Parameter-Fit führte. Diese Methode bestimmte OEF-Werte von $(37.5 \pm 4.6) \%$ in gesunder weißer Hirnsubstanz und $(27.8 \pm 4.3) \%$ in tumoröser Hirnsubstanz. Ein anderer Ansatz bestand aus der Bestimmung der beiden anderen Parameter (R_2 und R'_2) in separaten Messungen (weiße Hirnsubstanz: $R_2 = 14.4 \pm 0.8 \text{ Hz}$, $R'_2 = 7.3 \pm 1.4 \text{ Hz}$; graue Hirnsubstanz: $R_2 = 12.8 \pm 1.8 \text{ Hz}$, $R'_2 = 8.0 \pm 2.2 \text{ Hz}$) und einer anschließenden Korrektur und Validierung mit Hilfe von Phantomexperimenten. Diese Technik wurde schließlich für *in vivo* Experimente verwendet. Diese separate Fitmethode verspricht eine hohe Fitgenauigkeit und brachte OEF-Werte von $(22.0 \pm 3.4) \%$ und $(26.9 \pm 6.5) \%$ für weiße und graue Hirnsubstanz hervor. In dieser Arbeit wird eine weitere Methode zur OEF-Berechnung beschrieben, die auf der Trennung des vom venösen Blut hervorgerufenen Signals vom restlichen Signal basiert. Eine anschließende Messung der transversalen Relaxationsrate - $(13.1 - 18.9) \text{ Hz}$ in den untersuchten Regionen - und eine Kalibrierung der Oxygenierung ermöglichen die OEF-Berechnung. Außerdem wurde die suszeptibilitätsgewichtete Bildgebung (SWI), deren Bildkontrast auf der Oxygenierung der Venen basiert, von der Kopf- auf die Nierenbildgebung übertragen. Die implementierte Technik verbesserte das Kontrast-zu-Rausch-Verhältnis um 33% im Vergleich zur Standard-SWI-Technik. Nachdem die SWI-Bilder der Niere rekonstruiert waren, konnte eine Kontraständerung nach induzierter Oxygenierungsänderung qualitativ beobachtet werden.

Die präsentierten Methoden brachten vielversprechende Ergebnisse zur Bestimmung des OEF hervor, welches ein Indikator für die Gewebektivität ist. Diese Bestimmung könnte in der Strahlentherapie für die Bestrahlungsplanung und die Therapieüberwachung verwendet werden.

Contents

1	Introduction	1
2	Basic Principles	5
2.1	Basic Principles of Nuclear Spin	5
2.1.1	Nuclear Spin and Magnetic Moment	5
2.1.2	Zeeman-Effect	6
2.2	Basic Principles of Nuclear Magnetic Resonance	7
2.2.1	Macroscopic Magnetization	7
2.2.2	Motion of Magnetic Moments in an External Field	8
2.2.3	Radio Frequency Fields and Rotating Frame of Reference	9
2.2.4	Free Relaxation in a Homogeneous Magnetic Field: Bloch Equations	9
2.2.4.1	Spin-Lattice Relaxation	10
2.2.4.2	Spin-Spin Relaxation	11
2.2.5	NMR-Signal Detection	12
2.2.6	Relaxation in Inhomogeneous Magnetic Fields	13
2.2.7	Signal Decay for Particular Magnetic Field Distributions	14
2.2.8	T_2 and T_2^* Relaxation	15
2.2.9	Spin Echo	15
2.3	Magnetic Resonance Imaging	18
2.3.1	Spatial Encoding	18
2.3.1.1	Slice Selection	18
2.3.1.2	Phase Encoding	20
2.3.1.3	Frequency Encoding	21
2.3.2	k-space and Image Reconstruction	22
2.3.3	Discrete Sampling of k-Space	23
2.3.4	Image Resolution	25
2.3.5	Imaging Methods	26
2.3.5.1	Spin Echo Sequence	27
2.3.5.2	Gradient Echo Sequence	27
2.3.5.3	Echo Planar Imaging (EPI)	28
2.3.6	Image Contrast	29
2.3.6.1	T_1 -Weighted Contrast	30
2.3.6.2	T_2 -Weighted Contrast	30
2.3.6.3	Spin Density Contrast	30
2.4	Physiological Properties of Blood	31
2.4.1	Oxygen Transport in the Blood	31
2.4.2	Tissue Oxygen Consumption	32
2.4.3	Oxygenation Dependent Magnetic Properties of Blood	34
2.4.4	Microscopic Vascular Anatomy of the Brain	35

2.5	Susceptibility Weighted Imaging (SWI) of the Kidney	36
2.5.1	Physiological Background and Clinical Applications	36
2.5.2	SWI-Theory	37
2.5.3	Data Processing	38
2.5.3.1	Standard SWI Reconstruction / Phase Masks	38
2.5.3.2	Enhanced SWI Reconstruction for Kidney Imaging	38
3	Materials and Methods	41
3.1	Modeling Blood Vessels in the Brain	41
3.1.1	Single Vessel in Homogeneous Tissue	41
3.1.2	Partial Volume Effect	42
3.1.3	Analytical Solution for MR Signal Decay in the Presence of a Para- magnetic Cylinder	42
3.1.4	Blood Vessel Network in Homogeneous Tissue	43
3.2	MR Techniques	46
3.2.1	MR Scanners	46
3.2.2	MR Sequences	46
3.2.2.1	Gradient Echo Sampled Spin Echo (GESSE)	46
3.2.2.2	Multi-Slice Multi-Echo Gradient Echo (MMGE)	46
3.2.2.3	Carr-Purcell-Meiboom-Gill (CPMG)	48
3.2.3	Measurement Phantoms	48
3.2.3.1	Relaxation Phantom	48
3.2.3.2	Tissue Phantom	48
3.2.3.3	Flow Phantom	48
3.3	Macroscopic Inhomogeneity Correction	49
3.4	Measurement of Tissue Oxygenation: Analytical Methods	52
3.4.1	Three-Parameter Fit (TPF) Approach	52
3.4.2	Semi-Quantitative (SQ) Approach	53
3.4.2.1	Determination of the CBV Using a DSC-Perfusion Mea- surement	54
3.4.2.2	Combination of DSC with GESSE Measurement	56
3.4.3	Three-Sequence-Combination (TSC) Approach	56
3.5	Measurement of Tissue Oxygenation: Venous Blood Isolation Method	57
3.5.1	Isolation of Venous Blood Signal	57
3.5.1.1	Velocity Encoding	57
3.5.1.2	Capillary Model	58
3.5.1.3	Statistical Analysis for the Capillary Model	59
3.5.1.4	Different Flow Types	60
3.5.1.5	Development of the Velocity-Selective Module (VSM)	62
3.5.1.6	Velocity-Selective Spin Labeling (VSSL)	62
3.5.1.7	Sequence Design: Consideration of T_1 Relaxation	64
3.5.1.8	Sequence Design: TI -Variation	65
3.5.1.9	Sequence Design: Variation of v_{cut}	66
3.5.2	Echo Time Variation	66
3.5.3	OEF Calibration	66

4	Results	69
4.1	TPF-Method	69
4.1.1	OEF Calculation	73
4.2	SQ-Method	75
4.3	TSC-Method	77
4.3.1	Phantom Measurements: Sequence Correction	79
4.3.2	Phantom Measurements: Correction Validation	83
4.3.3	<i>in vivo</i> Correction	85
4.4	Velocity-Selective Spin Labeling	87
4.4.1	Phantom Measurements	88
4.4.2	<i>in vivo</i> Measurements	89
4.5	Comparison of the Different Techniques	92
4.6	SWI of the Kidney	93
4.6.1	Contrast-to-Noise Ratio (CNR) Calculation	94
4.7	Kidney SWI under Oxygenation Variation	96
4.8	OEF and SWI	97
5	Discussion	99
5.1	Analytical Methods for OEF Calculation	99
5.1.1	Magnetic Field Inhomogeneities	99
5.1.2	TPF-Method	100
5.1.3	SQ-Method	100
5.1.4	TSC-Method	101
5.1.5	Oxygenation Quantification	103
5.2	Venous Blood Isolation Method	103
5.3	SWI of the Kidney	104
5.3.1	Kidney SWI under Oxygenation Variation	106
6	Conclusion and Outlook	107
	Bibliography	109
	List of Figures	117
	List of Tables	119

1 Introduction

In the course of the last few years, Magnetic Resonance Imaging (MRI) has become one of the most important imaging methods in clinical procedures. Both, research as well as the clinical diagnostics benefit from the wide spread of possibilities enabled by MRI. The MRI images can be created by means of a strong magnetic field and coils able to emit radio waves and detect the signal. The hydrogen nuclei in the body can be compared to small static magnets that align themselves with the streamlines of the external field. If a radio wave with a certain frequency is irradiated, the nuclei become excited and leave the alignment. If the radio wave is switched off, the hydrogen nuclei return to their initial state. During this return, each proton emits a weak signal that can be acquired by the coils. Fourier analysis of the signal yields the localization of the origin of the signal. The protons of hydrogen in the body are well suited for this imaging method because the water content in the body of an adult person is about 70 – 80 %. The high abundance of water is the main reason why the highest signal can be achieved with proton MRI.

One of the most interesting features of MRI is the possibility to create specific image contrasts depending on the choice of the pulse sequence, which is the handling tool of the operator. This is why, especially for imaging soft tissue in the human body, MRI has become irreplaceable. In MRI, the radiation exposure is not harmful to health, which is the main advantage compared to x-ray or computer tomography (CT) scans, where very high energetic radiation is used, which leads to DNA damage. Nevertheless, there are several reasons why in a certain situation an x-ray/CT scan is more useful than a MR scan. For example, bone injuries and fine lung structures are much better presentable with a CT scan. Moreover, the investigation time is usually shorter in a CT scanner. Another disadvantage of MRI is the limited applicability of persons with metallic implants or cardiac pacemakers. Because both techniques have great advantages in certain application areas, these two techniques will always exist beside each other.

In MRI, the local magnetic field determines the relaxation rate - the reciprocal value of the relaxation time - of the investigated nucleus. The local magnetic field is not only given by the applied external magnetic field, but also influenced by the surrounding tissue, blood flow, diffusion and other physiological phenomena. Therefore, the choice of the correct technique enables the illustration of physiological properties and changes. Hence, MRI does not only offer a very good tool for morphological imaging, but also for determining physiological parameters, the most prominent example being the illustration of activated brain regions. During the last 30 years, there were many publications in the area of neurofunctional research. The pioneer work in this field was made and presented by Ogawa et al. [1990]. This work is based on the fact that the image contrast depends on the oxygenation of the blood. Therefore, this phenomenon is called Blood Oxygenation Level Dependent (BOLD) effect. The origin of this effect can be found in the susceptibility change of the blood during its circulation through the body. While arterial blood

is diamagnetic just like the surrounding tissue, the blood changes its magnetic properties by oxygen delivery in the capillary bed and becomes paramagnetic in the veins. Quantification of the magnetic field distortion offers information of the oxygenation status of the tissue. The technique of the measurement of neuronal activation with MRI is called functional MRI (fMRI), and has been widely studied. In contrast to that, the field of work of the oxygen consumption during the resting state has not received much attention yet.

The central parameter in this work is the oxygen extraction fraction (OEF), which is the ratio between consumed oxygen and delivered oxygen in the tissue. This work concentrates on the calculation of tissue oxygen supply during the resting state. The knowledge about this provides important information about the viability of the tissue [Schmidt and Thews, 1995]. Because the viability of cells depends on the tissue oxygen supply, this information is of great interest for clinical diagnostics.

For the oncology, the measurement of oxygenation is of interest because tumor oxygenation is an indicator for aggressiveness and affinity to metastasization [Brown and Giaccia, 1998]. Moreover, the chance of success of a radiotherapy or chemotherapy depends on the oxygen partial pressure of the tumorous tissue [Molls et al., 1998]. That is the reason why hypoxia is a large obstacle to tumor therapy [Vaupel and Mayer, 2007]. The aim of research of many scientists was to increase the tumor's sensitivity to chemotherapeutics and radiotherapy by increment of the tumor oxygenation during the treatment [Kaanders et al., 2004, Harrison and Blackwell, 2004].

There exist some invasive and non-invasive techniques that allow determination of tissue oxygenation, but all of them have certain disadvantages. For example, the usage of oxygen electrodes is strongly invasive. Another technique requires the usage of a toxic contrast agent (^{19}F). Therefore, these techniques are basically applicable for animal studies. A non-invasive technique like Magnetic Resonance Susceptometry (MRS) does not enable the illustration of oxygenation maps but allows only to extract one global value from a large draining vein [Fernández-Seara et al., 2006]. Another technique, that enables determination of blood oxygenation non-invasively is near infrared spectroscopy (NIRS). The disadvantage of this technique is the fact that only cortical tissue can be scanned [Ferrari et al., 2004]. Positron Emission Tomography (PET) is a nuclear medical technique which enables determination of cerebral blood oxygenation (Y), cerebral blood volume (CBV), cerebral blood flow (CBF) and cerebral metabolic rate of oxygen (CMRO_2). The main problems of this technique are the short half-life time and the radioactivity of the tracer ^{15}O [Ito et al., 2004]. Moreover, this technique is very expensive and time-consuming in a clinical workflow.

MRI does not present any of the mentioned problems but has the potential to spatially resolve the tissue oxygenation of a blood network embedded in a tissue. The measured MR signal decay has an irreversible contribution from the spin-spin interaction, also called T_2 decay and a reversible contribution resulting from static field inhomogeneities, called T_2' decay. In the mentioned model, the signal decay depends only on the volume fraction of the deoxygenated blood volume and the oxygenation of the blood. Yablonskiy and Haacke [1994] first described the theory of the signal behavior in such a blood vessel network. Recently, this technique has been applied in healthy volunteers [He and Yablonskiy, 2007].

In this work, three different analytical approaches of the calculation of the OEF are presented. All methods are based on the tissue model presented by Yablonskiy and Haacke [1994]. The central sequence of all these methods is a gradient echo sampled spin echo sequence (GESSE) [Yablonskiy and Haacke, 1997], which enables the measurement of the signal relaxation rates before and after a spin echo. In a two-compartment model, the signal behavior buries information about the volume fraction of the compartment that is responsible for the characteristic signal decay and the magnitude of this compartment. For *in vivo* measurements, these two parameters are the volume fraction of the deoxygenated blood λ and the susceptibility difference between the deoxygenated blood and the surrounding tissue $\Delta\chi$. In the signal fit, there exist three free parameters: λ , the (tissue specific) irreversible relaxation rate R_2 and the reversible relaxation rate R'_2 , that depends on $\Delta\chi$. The knowledge of λ and R'_2 yields together with known values (hematocrit, susceptibility difference between fully oxygenated and fully deoxygenated blood, magnetic field strength, gyromagnetic ratio) a possibility to calculate an OEF value that is representative for the investigated voxel. This method is also known as *q-Bold* (quantitative BOLD) and has already afforded interesting *in-vivo* results [He and Yablonskiy, 2007, He et al., 2008, Solin, 2009].

The main problem with this technique is the fact that three parameters in the signal equation are determined by only one fit resulting in an uncertainty of the parameter estimation depending on the signal-to-noise ratio (SNR) [Solin, 2009].

The first part of the result section of this work deals with *in vivo* measurements and data postprocessing of this TPF-method (*three-parameter fit*) and the big challenge to improve fit stability to produce more reliable parameter maps.

Another analytical method, that is developed in this work, uses an external calculation method for the blood volume. This method uses the advantage of a contrast agent injection, that enables the pixel-wise determination of the cerebral blood volume (CBV) by perfusion data postprocessing. This information was used as an input parameter for the data fit of the previously presented method. The fit reduces to a two-parameter-fit that leads to a higher fit stability and certainty. The fact that this technique yields a value for the whole blood volume but not the deoxygenated part prohibits a quantitative determination of the OEF. Hence, this method is called *semi-quantitative* (SQ) method. This method was only applied on patients in clinical routine but not on volunteers because of the application of a contrast agent injection.

The third method developed in this work is called *three-sequences-combination* (TSC) method. The aim of this method is to reduce the three-parameter fit of the TPF-method into three one-parameter fits. This enables a reliable calculation of all three parameters and, therefore, a reliable determination of the OEF. For the calculation of the three parameters, several sequences have to be applied. The problems that occur with this technique were investigated, understood and eliminated with the help of different phantom experiments and correction methods. Initial occurring parameter determination errors could be removed by the developed technique. Since the correction method is also applicable to *in vivo* data, the TPF-method is able to produce very reliable OEF maps under clinical conditions.

Another completely different technique is used for quantitative oxygenation measure-

ment, that can be separated into three steps [Bolar et al., 2009]. The first step is the separation of the signal originating from the veins from the total signal. The second step is the calculation of the relaxation time T_2 of the separated venous blood. The third step consists of the calculation of the oxygenation by an existing calibration curve [Zhao et al., 2007]. In this work, this technique was implemented, tested in a phantom experiment and, finally, applied to *in vivo* experiments.

In addition to that, this work includes an excursion to abdominal imaging, where the - for brain imaging established - technique of susceptibility weighted imaging (SWI) was implemented, and the problems and first results of the implementation of this technique at the kidney are presented. In addition to that, the change of the SWI contrast under oxygenation variation in the kidney was investigated. This was realized by water uptake during the experiment.

2 Basic Principles

2.1 Basic Principles of Nuclear Spin

In 1891, the hyperfine structure of atomic spectral lines was first observed by Albert Abraham Michelson. This new splitting was several orders of magnitude smaller than the fine structure and could be detected only thanks to the, at that time, newly developed interferometric techniques. In 1897, Charles Fabry and Alfred Perot published the fundamental work on their interferometer. Some years later, in 1924, Wolfgang Pauli explained this splitting of the spectral lines as due to the interaction of the nuclear magnetic moment with the magnetic field at the nucleus caused by the atomic electrons. The first experiment, that verified the theory of the magnetic moment of an atomic nucleus was performed by the physicist Isidor Isaac Rabi (1939). Five years later, he was awarded the Nobel Price in Physics for this discovery.

2.1.1 Nuclear Spin and Magnetic Moment

The atomic nucleus consists of two different nucleons: Protons and neutrons. All nuclei with an uneven number of nucleons have an inherent angular momentum, also called *nuclear spin*, \vec{I} . The total angular momentum \vec{J} of a nucleus consists of the nuclear spin \vec{I} and the orbital angular momentum \vec{L} , which is zero for the basic state. In this case, \vec{J} is equal to \vec{I} , which is related to the magnetic moment

$$\vec{\mu} = \frac{g_I \mu_K}{\hbar} \cdot \vec{I}, \quad (2.1)$$

where \hbar is Planck's constant ($\hbar = \frac{h}{2\pi} = 1.0545 \cdot 10^{-34}$ Js) and g_I , the so-called *gyromagnetic factor*, is a nucleus specific constant. $\vec{\mu}$ can be orientated parallel or antiparallel to \vec{I} . The nuclear magnetic moment is expressed in units of the nuclear magneton,

$$\mu_K = \frac{e\hbar}{2m_p}, \quad (2.2)$$

where e is the elementary charge ($1.602 \cdot 10^{-19}$ C) and m_p the mass of a proton. The constants of Eq. 2.1 can be combined to a nucleus specific factor, the gyromagnetic ratio

$$\gamma = \frac{g_I \mu_K}{\hbar}. \quad (2.3)$$

The gyromagnetic ratio is characteristic for the investigated nucleus. In this work, the nucleus of hydrogen is investigated, which has, compared to other nuclei, a large gyromagnetic ratio and a large abundance in the human body (Tab. 2.1). That is why the following discussion will focus on imaging hydrogen protons. For ^1H , the following constants are valid: $\gamma = 42.576821$ MHz/T, $\gamma = 2\pi \cdot \gamma = 267.518056$ MHz/T and $g_I = +5.5856$.

Table 2.1 List of different nuclei with corresponding spins (in units of \hbar), magnetic moments (in units of a nuclear magneton, μ_m) and gyromagnetic ratios (in units of MHz/T) and relative body abundances. The low concentration of oxygen can be explained by the low abundance of the isotope ^{17}O compared to ^{16}O . Table adopted from Haacke et al. [1999].

Nucleus	Spin	Magnetic moment	γ	Abundance in human body
^1H	1/2	2.793	42.58	88 M
^{23}Na	3/2	2.216	11.27	80 mM
^{31}P	1/2	1.131	17.25	75 mM
^{17}O	5/2	-1.893	-5.77	16 mM
^{19}F	1/2	2.672	40.08	4 μM

2.1.2 Zeeman-Effect

The magnitude of the nuclear spin is directly related to the spin quantum number s by

$$|\vec{I}| = \sqrt{s \cdot (s + 1)}\hbar, \quad (2.4)$$

where s can be non-negative integers or half integers. In addition to the spin quantum number there is another dimensionless quantum number that characterizes the nuclear spin: The orientation of the spin is characterized by the spin magnetic quantum number m_s . Assuming an external field in z -direction, there is a quantized projection of the z -component of the nuclear spin,

$$I_z = m_s\hbar. \quad (2.5)$$

The spin magnetic quantum number m_s ranges from $-s$ to s with $\Delta m_s = 1$, resulting in $2s + 1$ nuclear spin states. Without an external field these states are degenerated, i.e. they are the same. By applying an external field different spin states are induced and the degeneracy disappears. The reason for this quantization can be found in the quantum mechanics, where discrete energy states of a system can be found. The interaction of the nuclear spin with an external magnetic field leads to the corresponding Hamiltonian

$$H = -\vec{\mu} \cdot \vec{B} = -\gamma\vec{I} \cdot \vec{B}. \quad (2.6)$$

Assuming a homogeneous, time-independent external magnetic field orientated in the z -direction $\vec{B}_0 = (0, 0, B_0)$, the Hamiltonian can be written as

$$H = -\gamma I_z B_0. \quad (2.7)$$

The solution of this eigenvalue equation of the Hamiltonian are $2s + 1$ discrete, equidistant energy levels

$$E_m = -m_s\hbar\gamma B_0, \quad (2.8)$$

where m_s being one of $2s + 1$ possible values. To calculate the Energy gap ΔE_m for two adjacent energy levels, one has to subtract the energy of a state with m_s from the energy of a state with $m_s + 1$,

$$\Delta E = -m_s\hbar\gamma B_0 + (m_s + 1)\hbar\gamma B_0 = \hbar\gamma B_0. \quad (2.9)$$

In the case of hydrogen ($I = 1/2$), two energy levels are present. The lower energy state is called *spin up*-state, the higher energy state is called *spin down*-state. The energy gap between these two levels is proportional to the main magnetic field B_0 . The splitting of the energy level by an external magnetic field is called *Zeeman effect* (Fig. 2.1) and transitions in both directions are possible. In the case of absorption and emission, the photon energy of $\hbar\omega$ is absorbed and emitted respectively. By application of a - to the main field perpendicular - alternating magnetic field with the angular frequency

$$\omega_0 = \gamma B_0, \quad (2.10)$$

the so-called *Larmor frequency*, a transition from the lower to the higher energy level is possible. This frequency denotes the resonance frequency of a nucleus. The interaction between the nuclear magnetic moment and an external high frequency field is called *nuclear magnetic resonance* (NMR).

2.2 Basic Principles of Nuclear Magnetic Resonance

NMR is the study of magnetic properties of the nuclei. It was independently discovered by Purcell et al. [1946] and Bloch [1946]. It could be observed that electromagnetic radiation was absorbed and emitted by nuclei that were placed in a strong magnetic field. Six years later, Bloch and Purcell shared the Nobel Prize in Physics for their pioneer work on the field of NMR. The classical description of the NMR phenomena are only valid for a large amount of decoupled or weakly coupled spins with a spin quantum number of $I = 1/2$, which is the case for ^1H . A more detailed description can be found in the standard works of Abragam [1961] and Slichter [1963].

2.2.1 Macroscopic Magnetization

In MRI, the typical size of a measured volume is in the order of cubic millimeters. Assuming an investigated volume of 1 mm^3 that mainly consists of water with a hydrogen nuclei density of 0.111 mMol . Multiplication with the Avogadro constant ($N_A = 6.022142 \cdot 10^{23} \text{ mol}^{-1}$) leads to a total number of $6.69 \cdot 10^{19}$ protons. This large number of spins allows the introduction of a macroscopic magnetization \vec{M}_0 , which is the sum of the expected values for the single magnetic moments, $\langle \mu_i \rangle$, of all N spins per unit volume V ,

$$\vec{M}_0 = \sum_{i=1}^N \frac{\langle \mu_i \rangle}{V} = \frac{N}{V} \cdot \sum_{m_s=-s}^{+s} p_m \gamma \hbar m_s, \quad (2.11)$$

where p_m denotes the population probability of the respective Zeeman levels. Assuming thermal equilibrium at an absolute temperature T , the population probabilities are described by a Boltzmann distribution,

$$p_m = \frac{1}{Z} e^{-\frac{E_m}{k_B T}}, \quad (2.12)$$

where k_B is the Boltzmann constant ($1.381 \cdot 10^{-23} \text{ J/K}$) and Z denotes the state sum

$$Z = \sum_m e^{-\frac{E_m}{k_B T}}. \quad (2.13)$$

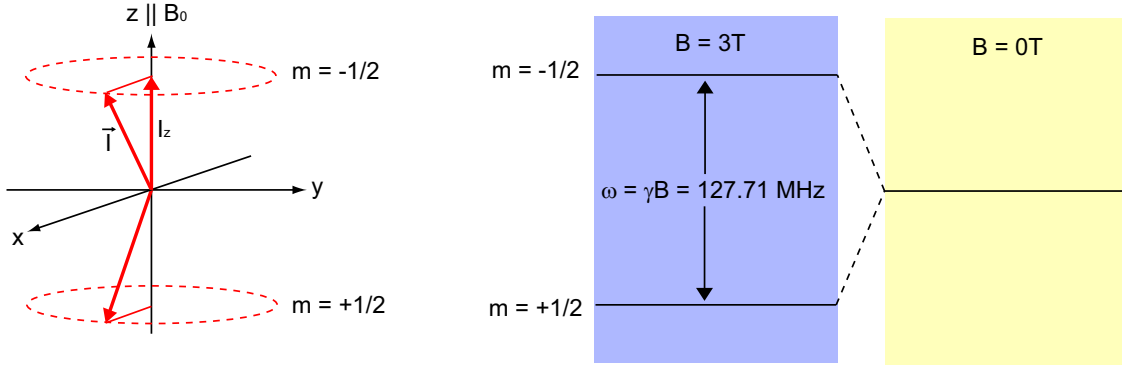


Figure 2.1 Zeeman effect for a hydrogen nucleus ($I = 1/2$) in a magnetic field. **Left:** Quantization of the nuclear spin in the direction of the magnetic field. **Right:** Splitting of the energy levels. Without a magnetic field the energy is degenerated, this degeneracy vanishes when an external magnetic field is applied.

The two possible energy states are populated according to Boltzmann statistics,

$$\frac{n_{-1/2}}{n_{+1/2}} = \frac{p_{-1/2}}{p_{+1/2}} = e^{-\frac{1}{2} \frac{\hbar\gamma B_0}{k_B T}} \cdot e^{-\frac{1}{2} \frac{\hbar\gamma B_0}{k_B T}} = e^{-\frac{\hbar\gamma B_0}{k_B T}}, \quad (2.14)$$

where $n_{-1/2}$ and $n_{+1/2}$ are the absolute populations of the anti-parallel and the parallel spin alignment, respectively. For the case of a human being (body temperature $T = 310$ K) in a clinical MRI magnetic field with a field strength $B_0 = 3$ T, it results in a much larger thermal energy than the magnetic energy. This results in a population ratio of 0.999997, which means that there are just 3 ppm more spins orientated parallel than anti-parallel to the magnetic field. With $N = n_{+1/2} + n_{-1/2}$ and $\Delta n = n_{+1/2} - n_{-1/2}$, the surplus of spins in parallel direction can be written as

$$\Delta n = N \tanh\left(\frac{1}{2} \frac{\gamma \hbar B_0}{k_B T}\right). \quad (2.15)$$

In thermal equilibrium at room temperature, where $\gamma \hbar B_0 \ll k_B T$, the macroscopic magnetization can be written as

$$\vec{M}_0 = \vec{\mu} \cdot \Delta n \approx \vec{\mu} N \frac{\gamma \hbar B_0}{2 k_B T}. \quad (2.16)$$

2.2.2 Motion of Magnetic Moments in an External Field

The macroscopic magnetization \vec{M} is directed along the main magnetic field. By using the Ehrenfest theorem, the time evolution of \vec{M} in a magnetic field can be determined,

$$\frac{d\vec{M}(t)}{dt} = \vec{M} \times \gamma \vec{B}(t). \quad (2.17)$$

Equation 2.17 is the analogon to the equation of motion of a spinning top in the gravitation field and implies that if $\vec{M}(t)$ and $\vec{B}(t)$ are not parallel, there is a precession of \vec{M} about \vec{B} .

2.2.3 Radio Frequency Fields and Rotating Frame of Reference

Transitions between the Zeeman levels can be induced by applying an electromagnetic, time-dependent field \vec{B}_1 . Assuming the main magnetic field \vec{B}_0 in z -direction, a circular polarized magnetic field perpendicular to B_0 and oscillating with the Larmor frequency, ω_0 , can be written as

$$\vec{B}_1(t) = \begin{pmatrix} B_1 \cos(\omega_0 t) \\ B_1 \sin(\omega_0 t) \\ 0 \end{pmatrix}. \quad (2.18)$$

This results in a change of the macroscopic magnetization

$$\frac{d\vec{M}(t)}{dt} = \vec{M} \times \gamma \begin{pmatrix} B_1 \cos(\omega_0 t) \\ B_1 \sin(\omega_0 t) \\ B_0 \end{pmatrix}. \quad (2.19)$$

It is useful to introduce a new frame of reference because the simultaneous precession about the \vec{B}_0 and the \vec{B}_1 field results in a very complicated equation of motion. The most suitable frame is a rotating frame with a rotation axis in \vec{B}_0 -direction and the rotation frequency ω_0 . In this case, the precession of the macroscopic magnetization \vec{M}' about \vec{B}_0 is compensated and only the precession about the \vec{B}_1 field (B_1 is directed in x -direction, without loss of generality) can be observed:

$$\frac{d\vec{M}'(t)}{dt} = \vec{M}' \times \gamma \begin{pmatrix} B_1 \\ 0 \\ 0 \end{pmatrix} = \vec{M}' \times \gamma \vec{B}_{\text{eff}}. \quad (2.20)$$

The irradiated electromagnetic field causes a tipping of the magnetization from the direction of B_0 about the effective magnetic field B_{eff} (Fig. 2.2). The resulting angle α between B_0 and \vec{M}' is called *flip angle* and depends on the amplitude and the duration of the irradiated field:

$$\alpha = \gamma \int_0^t B_1(t') dt'. \quad (2.21)$$

The magnetization is usually flipped about multiples of 90° , e.g. 90° for an excitation pulse and 180° for an inversion pulse.

2.2.4 Free Relaxation in a Homogeneous Magnetic Field: Bloch Equations

In the following, the z -direction is defined as the direction of the main magnetic field B_0 . The component of the magnetization vector in z -direction is called *longitudinal magnetization* M_z , the component of the magnetization vector perpendicular to M_z is called *transverse magnetization* M_\perp . Equation 2.20 says that if the magnetization is completely in the transverse plane, it stays in this plane. This is only the case for an ideal ensemble of spins. In 1946, Felix Bloch formulated a set of equations that describe the behavior of nuclear spins in a magnetic field after irradiation of RF pulses. He modified Eq. 2.20 to account for the observation that nuclear spins *relax* to equilibrium values. Bloch assumed, that the spins relax along the z -axis and in the xy -plane at different rates, designated $1/T_1$ and $1/T_2$ for the z -axis and the xy -plane, respectively, and postulated the famous Bloch equations:

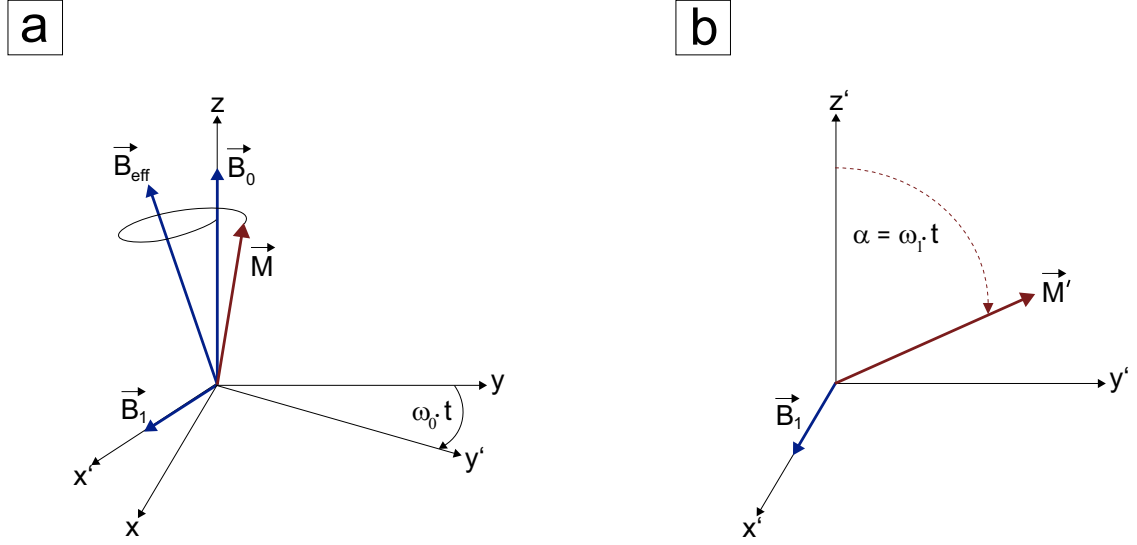


Figure 2.2 Motion of the magnetization vector. a) Precession of the macroscopic magnetization \vec{M} about the effective magnetic field \vec{B}_{eff} in the laboratory frame of reference. b) Precession of the macroscopic magnetization \vec{M}' about the magnetic field vector \vec{B}_1 in the rotating frame of reference.

$$\frac{dM_x}{dt} = \gamma (\vec{M} \times \vec{B})_x - \frac{M_x}{T_2}, \quad (2.22a)$$

$$\frac{dM_y}{dt} = \gamma (\vec{M} \times \vec{B})_y - \frac{M_y}{T_2}, \quad (2.22b)$$

$$\frac{dM_z}{dt} = \gamma (\vec{M} \times \vec{B})_z - \frac{M_0 - M_z}{T_1}, \quad (2.22c)$$

where M_x , M_y , M_z are the magnetization in x -, y - and z -direction, respectively, and M_0 is the equilibrium value of the longitudinal magnetization.

2.2.4.1 Spin-Lattice Relaxation

Assuming a longitudinal magnetization M_z which was flipped by a B_1 -field with a 90° -pulse, the spin system exchanges excess energy with the surrounding (i.e. the lattice). Therefore this process is called *spin-lattice relaxation*. Equation 2.22c states that the rate of change of the longitudinal magnetization is proportional to the difference between M_0 and M_z . The reciprocal of the proportional constant, T_1 , is called *longitudinal* or *spin-lattice relaxation time* and is empirically determined. Typical values for different tissues are shown in Tab. 2.2.

Assuming a homogeneous magnetic field in z -direction, Eq. 2.22c can be simplified to a first order linear differential equation,

$$\frac{dM_z}{dt} = \frac{1}{T_1} (M_0 - M_z), \quad (2.23)$$

which can be solved resulting in the following time-dependent expression for the longitudinal magnetization,

$$M_z(t) = M_0 \left(1 - e^{-t/T_1}\right) + M_z(t_0)e^{-t/T_1}. \quad (2.24)$$

$M_z(t_0)$ is the longitudinal magnetization, immediately after the excitation pulse. The thermal movement of the molecules causes fluctuating magnetic fields which spectral components induce transitions of the spin states for the case of consistency with the resonance frequency. The so-called *spin-lattice relaxation rate* $R_1 = 1/T_1$ is a quantity for the transition probability between Zeeman levels [Slichter, 1963]. Figure 2.3 schematically shows the relaxation process.

2.2.4.2 Spin-Spin Relaxation

The relaxation of the transverse component of the magnetization is based on the dephasing of the spins caused by the so-called *spin-spin* interaction. Brownian motion of the molecules causing quick variations of the magnetic field in the vicinity of every spin in the investigated probe. These fluctuating magnetic fields lead to a wider distribution of the resonance frequency around ω_0 . Therefore the phase coherence of the transverse magnetization will be lost over time resulting in a loss of the transverse component of the magnetization. In NMR experiments the x - and y -component of the transverse magnetization (Eq. 2.22a and 2.22b) are acquired simultaneously by coupled coils. For this reason it is useful to write the transverse magnetization as a complex number:

$$M_{\perp} = M_x + iM_y = |M_{\perp}| \cdot e^{i\phi}. \quad (2.25)$$

This equation and the assumption of a homogeneous magnetic field B_0 in z -direction simplifies the Bloch equations (Eq.2.22a and 2.22b) into

$$\frac{dM_{\perp}}{dt} = -i\gamma B_0 M_{\perp} - \frac{M_{\perp}}{T_2}. \quad (2.26)$$

Solving this first order linear differential equation leads to

$$M_{\perp}(t) = M_{\perp}(0)e^{-i\gamma B_0 t} e^{-\frac{t}{T_2}}. \quad (2.27)$$

Table 2.2 Longitudinal and transverse relaxation times for ^1H at 1.5 T. Table adopted from Haacke et al. [1999].

Tissue	T_1 (ms)	T_2 (ms)
gray matter (GM)	950	100
white matter (WM)	600	80
muscle	900	50
cerebrospinal fluid (CSF)	4500	2200
fat	250	60
blood	1200	100-200

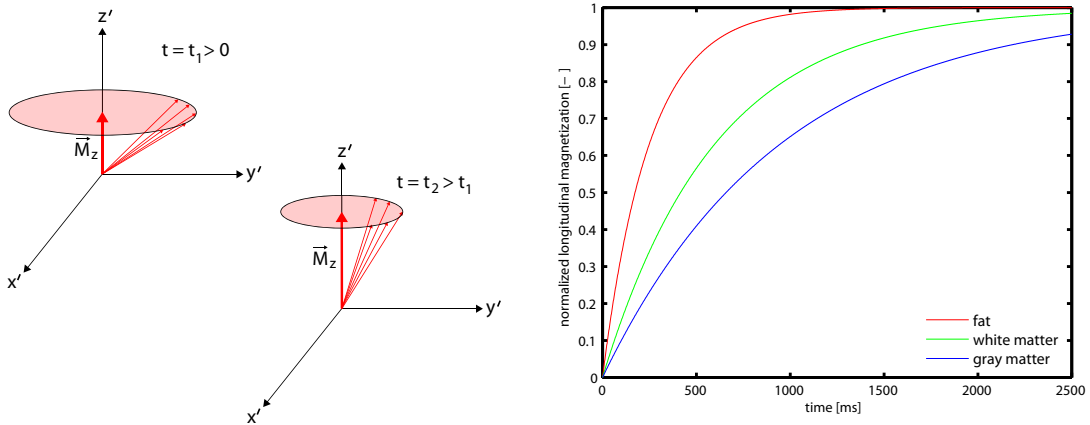


Figure 2.3 Spin-lattice relaxation. **Left:** At $t = 0$ after a 90° exciting pulse no longitudinal magnetization is present. Afterwards, it starts to relax to its equilibrium state. **Right:** Relaxation of the longitudinal magnetization for different kind of tissues at 1.5T (T_1 values taken from Tab. 2.2)

The first exponential term of Eq. 2.26 describes the precessing of the transverse component of the magnetization vector with the Larmor frequency ω_0 around the axis of the external magnetic field. The second exponential term describes the reduction of the transverse magnetization due to the mentioned interaction of the spins among each other, the so-called *spin-spin relaxation* or T_2 relaxation (Fig. 2.4). The transverse magnetization decay is referred to as free induction decay (FID).

2.2.5 NMR-Signal Detection

The measured signal in a NMR experiment is directly proportional to the transverse component of the magnetization. It induces a voltage in a receiving coil that is positioned transversely to the main magnetic field, typically in the range of μV . The detection of the complex signal (Eq. 2.26) can be realized by two coupled coils with a constant phase coherency. After detection the signal can be demodulated by multiplication with a sine and a cosine function, both synchronized with the Larmor frequency. The longitudinal component of the magnetization M_z does not induce a current because of the particular installation of the coils. Therefore the signal can be written as a result of Eq. 2.26,

$$S(\vec{r}, t) \propto M_{\perp}(\vec{r}, 0) \cdot e^{-i\gamma B_0 t} \cdot e^{-\frac{t}{T_2}}. \quad (2.28)$$

Because the magnitude of the magnetization depends on the spin density, which can fluctuate spatially, the signal is a function of the position vector \vec{r} . Since the acquired signal results from the whole measuring volume, an integration over the whole volume of interest is necessary:

$$S(t) = S_0 \cdot \int_V M_{\perp}(\vec{r}, 0) d\vec{r} \cdot e^{-i\gamma B_0 t} \cdot e^{-\frac{t}{T_2}}, \quad (2.29)$$

where S_0 is the proportional factor between the magnetization and the signal. Equation 2.29 shows that the temporal progress of the signal depends not only on the spin-spin

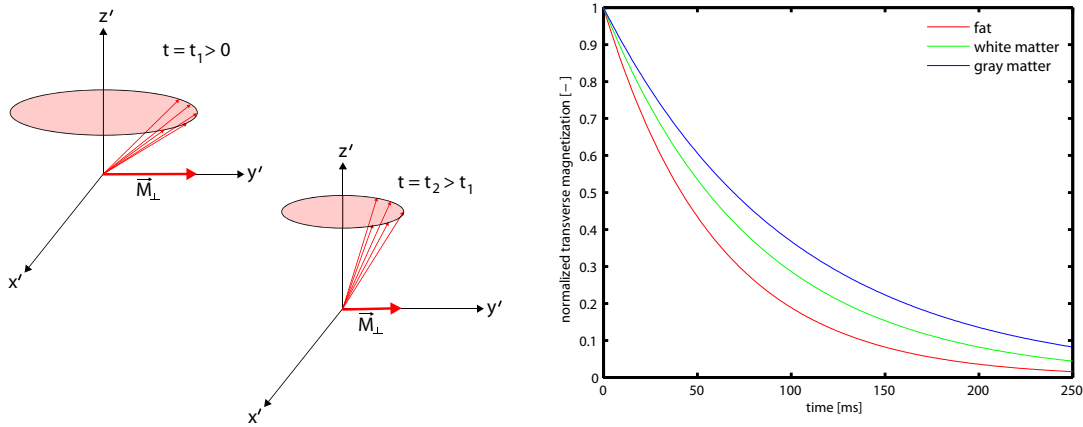


Figure 2.4 Spin-spin relaxation. **Left:** After the 90° excitation pulse the transverse magnetization decreases with a tissue-specific T_2 time. **Right:** Relaxation for three kinds of tissue is shown (T_2 values taken from Tab. 2.2).

relaxation but also on the local phase of the magnetization at the point of time of the measurement. For the case of a homogeneous magnetic field this phase is constant and the signal decays with T_2 . If there are additional inhomogeneous magnetic fields the phase factor becomes time- and position-dependent resulting in an additional contribution to the signal decay. For example, these fields are generated and used in MRI for spatial encoding of the signal. An additional phase can also be accumulated by main magnetic field inhomogeneities or inhomogeneities inside the probe. A magnetic field distribution inside the probe leads to an additional dephasing of the spins, further investigated in section 2.2.6.

2.2.6 Relaxation in Inhomogeneous Magnetic Fields

For a magnetic heterogeneous probe the relaxation time can be further reduced compared to the T_2 relaxation time. Local inhomogeneities are caused by local susceptibility differences resulting from different magnetic flow densities. The magnetic susceptibility χ is the proportionality factor of the magnetization \vec{M} and the magnetic field strength \vec{B}_0 .

$$\vec{M} = \chi \cdot \vec{B}_0 \quad (2.30)$$

Probes consisting of different compartments with different magnetic properties (i.e. different susceptibilities) cause a magnetic field distribution $B_s(\vec{r})$ inside the probe. The field distribution is also dependent on the position and the orientation of the different compartments inside the probe. Therefore it can be written as a function of the position \vec{r} and the magnetic susceptibility differences $\Delta\chi$ of the compartments,

$$B_s(\vec{r}) = f(\vec{r}, \Delta\chi). \quad (2.31)$$

For the transverse magnetization, these field variations cause an additional phase which is proportional to the local magnetic field B_s and - by neglecting diffusion effects - proportional to the time:

$$\phi(\vec{r}, t) = \gamma \cdot B_s(\vec{r}) \cdot t. \quad (2.32)$$

According to Eq. 2.29 there is another decaying factor in addition to single T_2 decay in an inhomogeneous medium:

$$S(t) = S_0 \cdot \int_V M_{\perp}(0) \cdot e^{-i\gamma B_s(\vec{r})t} d\vec{r} \cdot e^{-\frac{t}{T_2}}. \quad (2.33)$$

2.2.7 Signal Decay for Particular Magnetic Field Distributions

Equation 2.33 shows that the knowledge about the spatial distribution of the B_s field is necessary to calculate the signal progress. This knowledge is usually not available. Therefore an analytical solution of the integral in Eq. 2.33 is not possible. Here, two analytically solvable cases for a magnetic field distribution are considered to get an idea of the principle progress of the signal for the FID in inhomogeneous materials. To realize this, the integration over the volume can be transformed into an integral over a magnetic field distribution of the magnetic field in this volume. Introducing the probability density function $p(B_s)$ of the magnetic field strength B_s leads -by integrating- to the probability to find a field strength between B_s and ΔB in the probe volume,

$$P(\Delta B) = \int_{B_s}^{B_s+\Delta B} p(B_s) dB_s. \quad (2.34)$$

Using the substitution of the term $|M_{\perp}|dr$ by the term $p(B_s)dB_s$ in Eq. 2.33, the signal equation can be written as:

$$S(t) = S_0 \cdot \int_{-\infty}^{+\infty} p(B_s) \cdot e^{-i\gamma B_s t} dB_s \cdot e^{-\frac{t}{T_2}}. \quad (2.35)$$

It can be seen that the time-dependency of the signal can be calculated with the Fourier transform of the probability density function $p(B_s)$. Assuming the simple case of randomized distributed dipoles in a homogeneous medium [Brown, 1961], these dipoles locally experience a magnetic field B_s deviating from the main magnetic field described by a Lorentzian shape of the density of states:

$$p(B_s) = \frac{1}{\pi} \cdot \left(\frac{\sigma_B}{\sigma_B^2 + B_s^2} \right), \quad (2.36)$$

where σ_B is a quantity for the width of the distribution similar to the full width at half maximum (FWHM). This width is dependent on the assumed distribution of the dipoles in the model and on the strength of their magnetic moments. Therefore the temporal behavior of the signal can be expressed (by neglecting constant terms) by the Fourier transform of Eq. 2.36:

$$\mathcal{F}(p(B_s)) = \frac{1}{2} e^{-i\gamma\sigma_B|t|}. \quad (2.37)$$

This leads to an exponential decay of the signal:

$$S(t) = S_0 \cdot e^{-\frac{t}{T_2'}} \cdot e^{-\frac{t}{T_2}}, \quad (2.38)$$

with a decay constant

$$\gamma\sigma_b = \frac{1}{T_2'} \quad (2.39)$$

The second example for a magnetic field distribution inside a probe volume is a Gaussian distribution with the probability density function

$$p(B_s) = \frac{1}{\sqrt{2\pi}\sigma_B} e^{-\frac{B_s^2}{2\sigma_B^2}} \quad (2.40)$$

By applying the Fourier transform, this density function turns into a biexponential signal decay:

$$S(t) = S_0 \cdot e^{-\frac{\gamma^2\sigma_B^2 t^2}{2}} \cdot e^{-\frac{t}{T_2}} \quad (2.41)$$

Summing up, in practice a monoexponential signal decay is a good approximation to describe the signal progress resulting from a Lorentzian B_s distribution in the investigated volume. Nevertheless, a more detailed investigation of the signal yields that there is a superposition of a Lorentzian and a Gaussian distribution resulting in an additional biexponential signal decay. Both, probability density distributions and corresponding signal functions are illustrated in Fig. 2.5.

2.2.8 T_2 and T_2^* Relaxation

As mentioned in section 2.2.7, randomized dipoles in a homogeneous magnetic field cause an additional exponential factor for the relaxation of the transverse component of the magnetization. *In vivo*, the theory of the exponential decay is in good agreement with the measured data. Therefore the envelope of the signal decay can be written as a product of two exponential functions (Eq. 2.38). In this signal equation, the relaxation rate due to fluctuating magnetic fields and the relaxation rate due to local static fields are labeled as $R_2 = 1/T_2$ and $R_2' = 1/T_2'$, respectively. Commonly, these two relaxation rates are summarized to one relaxation rate

$$R_2^* = R_2 + R_2', \quad (2.42)$$

and the corresponding relaxation time

$$\frac{1}{T_2^*} = \frac{1}{T_2} + \frac{1}{T_2'} \quad (2.43)$$

According to Eq. 2.39, for narrow distributions (i.e. $\sigma_b \rightarrow 0$) the relaxation rate R_2' converges to zero and the relaxation time T_2^* converges to T_2 (Fig. 2.6).

2.2.9 Spin Echo

The two dephasing processes in Eq. 2.38 are fundamentally different. The fluctuating inhomogeneities originating from the fluctuating fields due to Brownian molecular motion cause an irreversible T_2 decay of the signal (Eq. 2.33). In contrast to that, constant inhomogeneities cause static field inhomogeneities. In the beginning of MR, it was a big difficulty to get a measurable signal due to very short T_2^* relaxation times caused by large field inhomogeneities. Hahn [1950] presented the first results of a spin echo

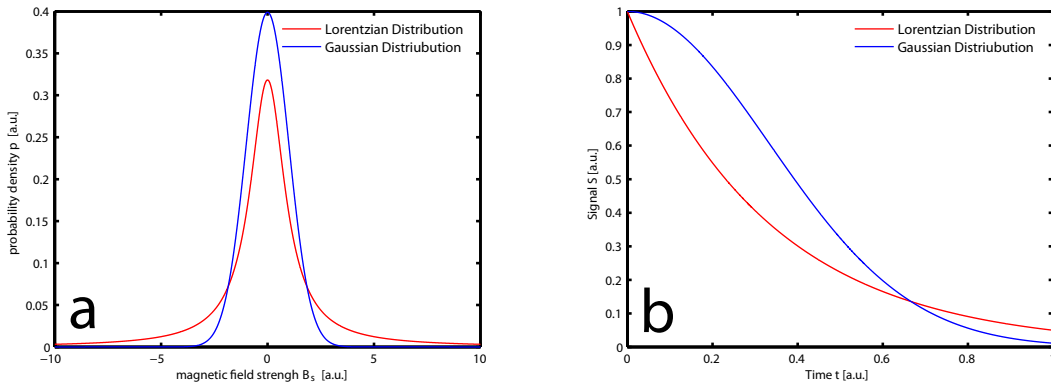


Figure 2.5 Lorentzian and Gaussian density of state of the magnetic field and the resulting signal decay. **a)** Density of state for a Lorentzian and Gaussian magnetic field distribution ($\sigma_b = 1$). The integral is normalized to 1. **b)** From a) calculated signal relaxation due to the respective magnetic field distributions (Eq. 2.36 to Eq. 2.41).

(SE) experiment where he was eliminating the spin dephasing process due to static field inhomogeneities. The theory of this work is that after a certain time delay after the excitation pulse, $TE/2$, a second HF pulse with a flip angle of 180° is applied. After another time delay of $TE/2$, the part of the signal that was dephased at the point of time of the second HF pulse due to static field inhomogeneities, is then rephased again resulting in a so-called *spin echo* at the time TE . This results in a dependency of the measured signal on the local T_2 value in the investigated probe. The result is that the measurement signal is dependent on the local T_2 value of the investigated probe. The spin echo experiment is described in detail in Fig. 2.7 and section 2.3.5.1.

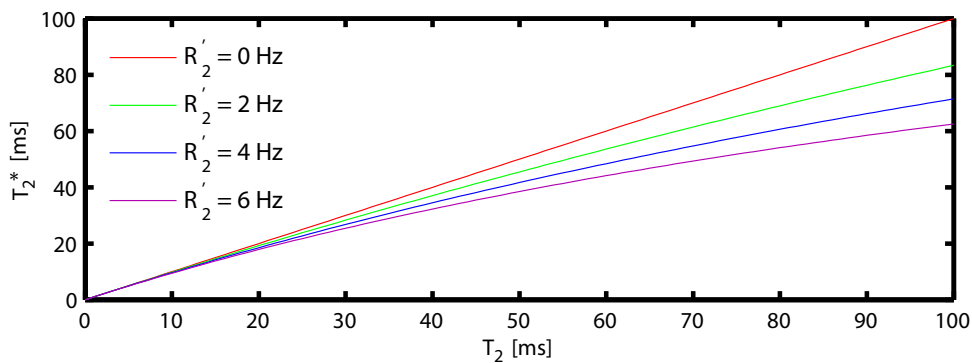


Figure 2.6 Dependency of T_2^* on T_2 and R_2' . R_2' depends on the magnetic field strength B_0 and the homogeneity of the field. For $B_0 = 3\text{T}$ and ^1H , typical values are between 1 Hz and 3 Hz. In certain areas even R_2' -values of 7 Hz can be found. For small R_2' -values and small T_2 -values, T_2^* converges to T_2 .

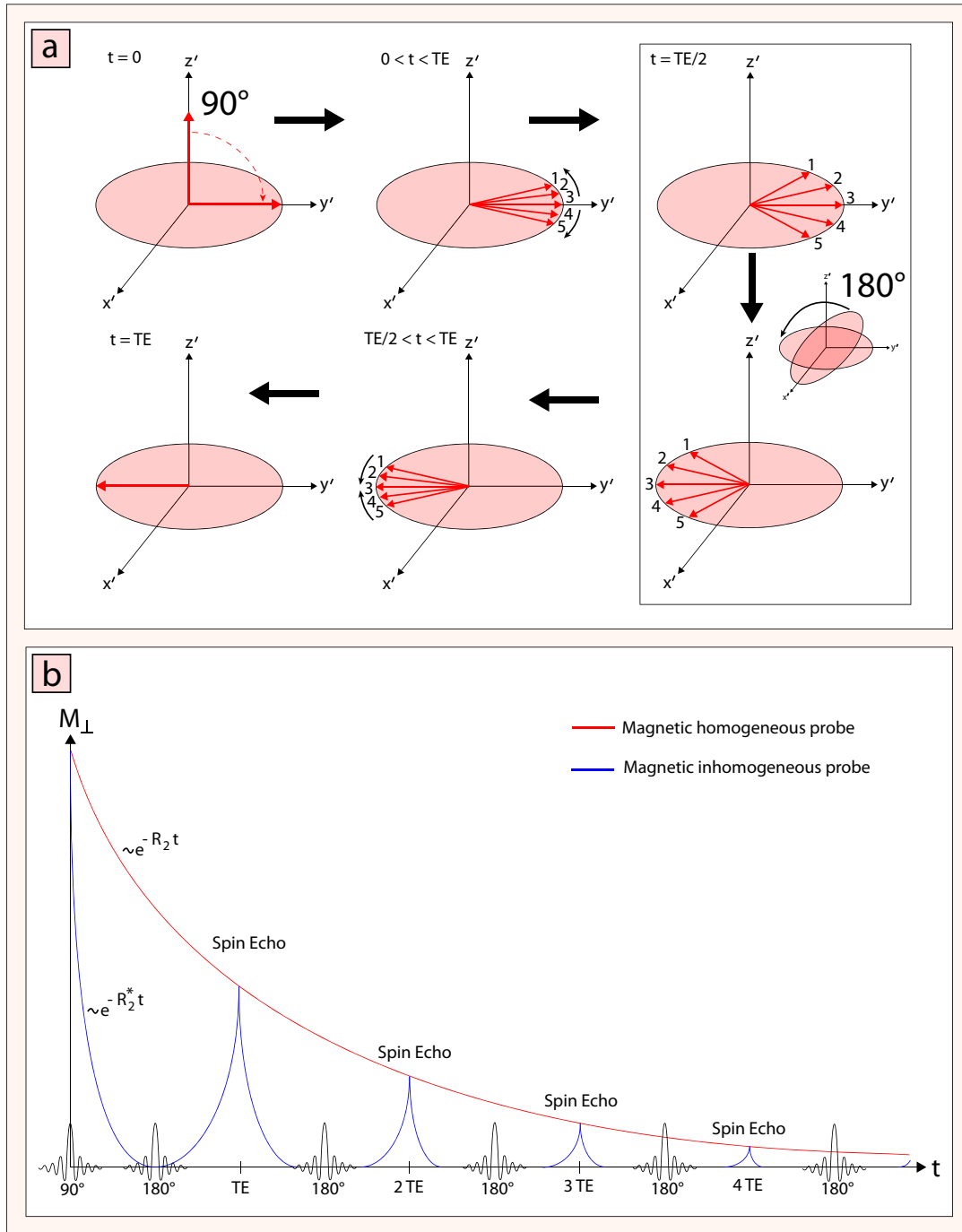


Figure 2.7 Spin echo. a) Formation: At $t = 0$, a 90° excitation pulse is applied to flip the longitudinal magnetization into the transverse plane. After dephasing of the spins, caused by T_2^* relaxation, another HF pulse with a flip angle of 180° is applied at $t = TE/2$ (here in x' -direction). After the time TE , the spins that were dephased due to static inhomogeneities are rephased again. This is called a *spin echo*. b) Applying further 180° pulses in equidistant time intervals of $\Delta t = TE$ creates further spin echoes.

2.3 Magnetic Resonance Imaging

The basics for magnetic resonance imaging (MRI) were developed in the 1970s. In 1971, Raymond V. Damadian discovered that healthy and tumorous tissues have different relaxation times. In 1973 and 1977, Paul Lauterbur and Peter Mansfield published two fundamental works in the field of MRI about the *Zeugmatography* [Lauterbur, 1973] and the *echo planar imaging* [Mansfield, 1977], respectively. Many years later, in 2003, Lauterbur and Mansfield received the Nobel Prize in Medicine *for their discoveries concerning magnetic resonance imaging*.

In this section the basics of MRI, especially spatial encoding, image reconstruction and some of the existing imaging methods, are explained. For further reading the books of Haacke et al. [1999] and Bernstein et al. [2004] are suggested.

2.3.1 Spatial Encoding

In section 2.2.5 was explained how to get a NMR signal. To create images, it is important to know which region of the investigated probe volume is responsible for which fraction of the signal. Therefore, a spatial encoding of the signal is desirable. Equation 2.10 tells us that the precession frequency is linear dependent on the external field. By using additional magnetic fields, a modification of the local frequency and phase can be achieved. Here, linear magnetic field gradients \vec{G} are used that are superimposed on the main magnetic field. The used electromagnetic fields are parallel to the main magnetic field, but have a field strength gradient in one spatial direction. For MRI experiments, three magnetic field gradients are used that change the magnetic field strength along all three spatial directions,

$$\vec{G} = \left(\frac{\partial B_z}{\partial x}, \frac{\partial B_z}{\partial y}, \frac{\partial B_z}{\partial z} \right). \quad (2.44)$$

According to Eq. 2.10, the precession frequency becomes spatial dependent

$$\omega(\vec{r}) = \gamma B(\vec{r}) = \gamma(B_0 + \vec{r} \cdot \vec{G}(\vec{r})). \quad (2.45)$$

Equation 2.45 implies, that each single volume element (voxel) can be spatially encoded. By using frequency analysis of the NMR signal, the signal of each voxel can be reconstructed. That is the reason why this imaging method is also called *Fourier imaging*. For 2D Fourier imaging, three spatial encoding steps are used, often referred to as slice selection, phase encoding and frequency encoding.

2.3.1.1 Slice Selection

For a selective excitation of a two-dimensional slice, a slice selection gradient G_z perpendicular to the desired slice plane (here z -direction) is applied. The local magnetic field strength can be written as

$$B_z(z) = B_0 + z \cdot G_z. \quad (2.46)$$

Simultaneously, a radio frequency (RF) pulse with the Larmor frequency ω_0 is applied. In analogy to Eq. 2.45, the precession frequency depends on the position along the z -axis,

$$\omega(z) = \omega_0 + \omega_G(z) = \gamma \cdot (B_0 + z \cdot G_z). \quad (2.47)$$

The result is a shift of the magnetization of only protons in the plane where the resonance condition is fulfilled. Protons outside the selected plane are not excited and will therefore not emit a signal. The RF pulse in combination with the slice selective gradient is called *selective pulse*. A RF pulse with the frequency ω_0 leads to an excitation of spins inside an infinitesimally thin slice. In practice this is not the case because a required RF pulse of infinite length is not realizable. The temporal limitation of the pulse leads to an selection profile $P(\omega)$ deviating from the Dirac delta function:

$$\begin{aligned}
 P(\omega) &= \mathcal{F} \left[B_1 \cos(\omega_0 t) \cdot \Pi \left(\frac{t}{\tau} \right) \right] \\
 &= B_1 \mathcal{F} [B_1 \cos(\omega_0 T)] * \mathcal{F} \left[\Pi \left(\frac{t}{\tau} \right) \right] \\
 &= B_1 \delta(\omega - \omega_0) * \tau \operatorname{sinc} \left(\frac{\omega \tau}{2} \right) \\
 &= B_1 \tau \operatorname{sinc} \left(\frac{(\omega - \omega_0) \tau}{2} \right),
 \end{aligned} \tag{2.48}$$

where τ is the duration of the pulse and Π is the rectangular function with

$$\Pi(t) = \begin{cases} 0 & \text{if } |t| > \frac{1}{2} \\ \frac{1}{2} & \text{if } |t| = \frac{1}{2} \\ 1 & \text{if } |t| < \frac{1}{2} \end{cases}. \tag{2.49}$$

Equation 2.48 shows that the frequency profile of the excitation is given by the Fourier transform of the time interval for the excitation, i.e. a sinc function (Fig. 2.8). In practice, a slice of a certain thickness Δz is excited. Since the RF pulse is not of infinite length, it does not have only one frequency but covers a certain bandwidth $\Delta \omega_{RF}$ that is dependent on the shape of the pulse and the duration of it. It can be seen from Fig. 2.9 that the resonance condition is satisfied for spins that precess with a frequency that is contained in the bandwidth of the excitation pulse. Figure 2.9 schematically shows that the thickness of the selected slice is dependent on the amplitude of the gradient field G_z and the bandwidth of the RF pulse. The selected slice thickness can be expressed as

$$\Delta z = \frac{|\omega(z_1) - \omega(z_2)|}{\gamma G_z} = \frac{\Delta \omega_{RF}}{\gamma G_z} \tag{2.50}$$

According to Eq. 2.48, for a rectangular slice profile, a sinc pulse of infinite length has to be applied. The temporal limitation of the pulse leads to a convolution in the frequency domain of the rectangular frequency profile with a sinc function. The shape of the resulting frequency distribution $P(\omega)$ depends on the duration τ of the HF pulse, and the slice thickness depends on the width of the sinc function $1/\tau_w$, where τ_w is the time between the two zero crossings on the left and the right side of the main maximum. For a sinc shaped pulse with a duration of four periods, the frequency distribution can be written as:

$$P(\omega) = \frac{1}{2} B_1 \tau \tau_w \Pi \left(\frac{t}{2\tau_w} \right) * \operatorname{sinc} \left(\frac{\omega \tau}{2} \right). \tag{2.51}$$

Figure 2.10 shows the dependency of the slice thickness on the window function and radiation frequency. If there is no slice selection gradient applied during the RF pulse, the excitation is called *global excitation*. In MRI measurements, a second slice selection

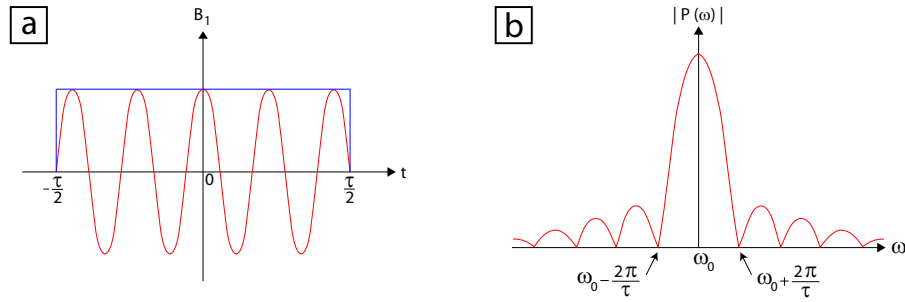


Figure 2.8 Excitation of the magnetization and excitation profile. **a)** Excitation by a temporally limited cosine-shaped impulse with a frequency ω_0 (red). The rectangular function (blue) represents the time interval of the length τ . **b)** Excitation profile of the pulse. The location of the minima depends on the duration of the pulse τ .

gradient lobe is applied directly after the first one along the same axis but in the opposite direction and a moment (amplitude \times time) equal to the half of the initial gradient lobe. This can be explained by the fact that the first slice selection gradient has a spin dephasing effect inside the selected slice. These dephasing spins are rephased again by the slice selection rephase gradient. After slice selection the MR signal of the excited slice has to be encoded in two directions.

2.3.1.2 Phase Encoding

For spatial encoding of the two remaining directions, a so-called *phase encoding* performed as a first step. Therefore a gradient G_y is applied in one direction (here y -direction) in the selected slice. This leads to a spatial dependency of the precession frequency

$$\omega(y) = \gamma(B_0 + G_y \cdot y). \quad (2.52)$$

Assuming a gradient G_y switched on for the time t_y , the magnetization accumulates a phase factor

$$\phi(y) = \phi_0 + \gamma G_y y t_y. \quad (2.53)$$

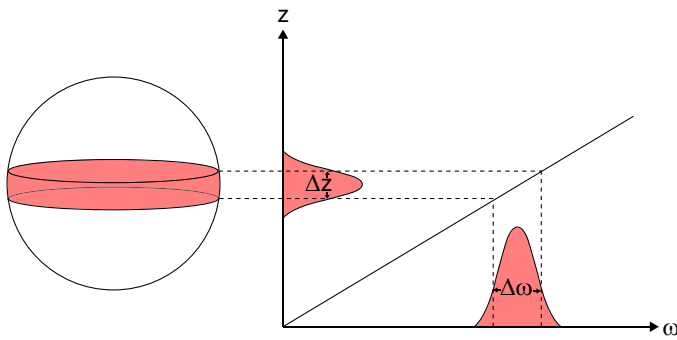


Figure 2.9 Slice selection I. By applying a HF pulse of a bandwidth $\Delta\omega$ together with a slice selection gradient G_z , a slice of a thickness of Δz is excited.

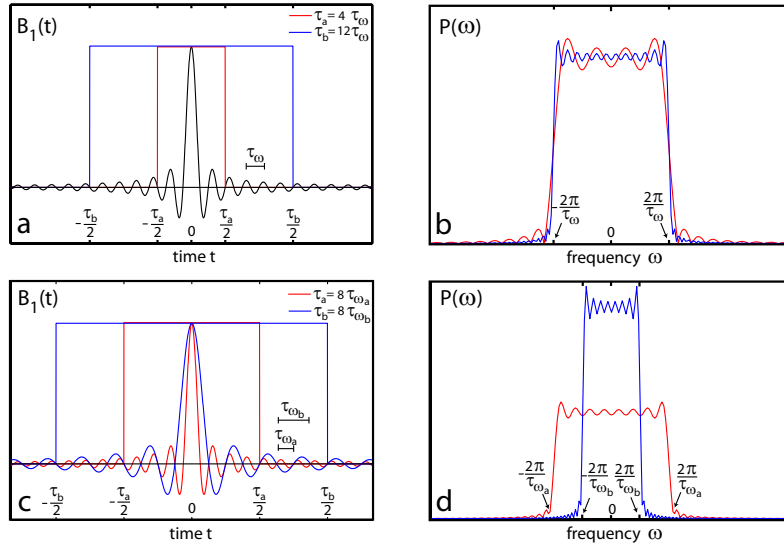


Figure 2.10 Slice selection II. a) The sinc-shaped HF pulse is multiplied with a rect function (Eq. 2.51). b) Depending on the number of side lobes of the sinc function the slice profile changes. The more side lobes are considered, the more the slice profile turns into a rectangular profile. c) If the number of considered side lobes is kept constant but the frequency of the irradiation is changed, d) the slice thickness changes.

After the gradient is switched off, the magnetization keeps on precessing with the Larmor frequency, but the accumulated phase remains,

$$M_{\perp} = |M_{\perp}| \cdot e^{i \int_0^{t_y} \omega(t) dt} = |M_{\perp}| \cdot e^{i\phi}. \quad (2.54)$$

The signal can be expressed as

$$S(t_y, G_y) = S(t) \int_y e^{i\gamma \int_0^{t_y} G_y(\tau) y d\tau} dy, \quad (2.55)$$

where $S(t)$ is given by Eq. 2.29. After this phase encoding step, the MR signal is encoded in phase direction. Since the signal does not contain different frequencies in y -direction, the phase encoded step has to be repeated several times with different G_y .

2.3.1.3 Frequency Encoding

As a last encoding step, a gradient is applied in the remaining uncoded direction (here x -direction) during data readout resulting in a spatial dependent frequency in x -direction,

$$\omega(x) = \gamma(B_0 + G_x \cdot x). \quad (2.56)$$

By using Fourier analysis of the signal, it is possible to determine the origin of the signal along the x -axis (Fig. 2.11). The signal $S(t)$ is acquired during the readout time t_x , and

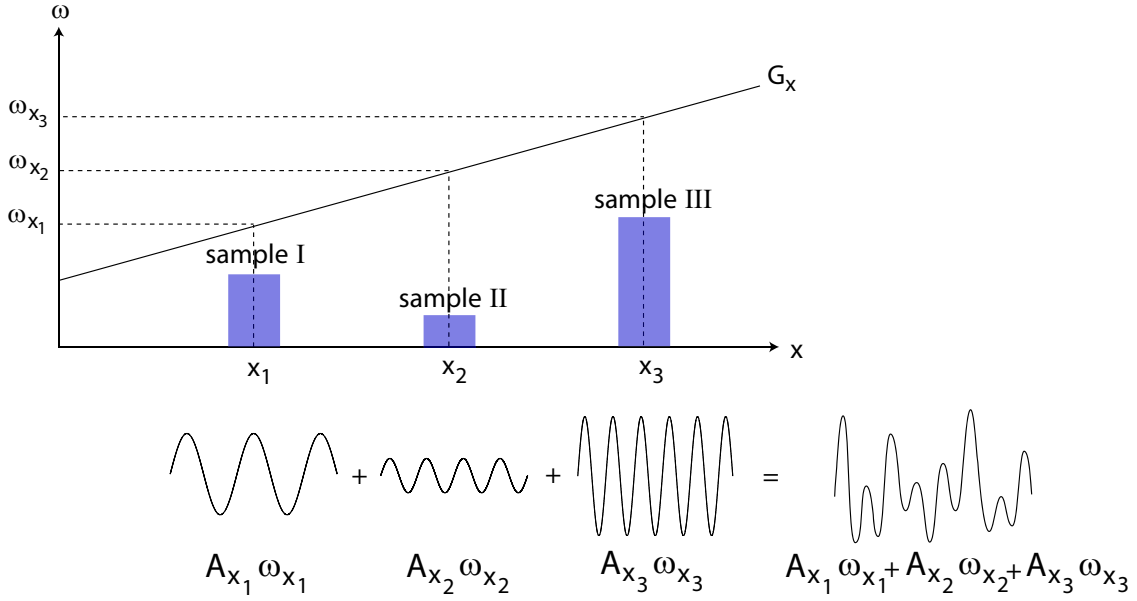


Figure 2.11 Frequency encoding. The blue rectangles represent homogeneous samples. The amplitude A_{x_i} of the signal of each sample is proportional to the amount of protons in the respective sample. By applying the frequency encoding gradient in x -direction, the frequency of the signal depends on the location along this direction.

can be expressed in analogy to Eq. 2.55 as

$$S(t_x, G_x) = S(t) \int_x e^{i\gamma \int_0^{t_x} G_x(\tau) d\tau} dx. \quad (2.57)$$

2.3.2 k-space and Image Reconstruction

In analogy to the signal decay in a NMR experiment (Eq. 2.29), the measured signal in a slice selective 2D imaging experiment can be described. First, the measured volume is limited by the slice selective gradient to a slice of a certain thickness. Then, the magnetization gets a spatial- and time-dependent phase factor by applying different gradients in a defined way. Considering Eqs. 2.55, 2.57 and 2.29 the signal in a 2D MRI experiment can be written as

$$S(t, G) = S_0 \int_x \int_y M_{\perp}(\vec{r}, 0) e^{i\gamma \left(\int_0^{t_x} G_x(\tau) x d\tau + \int_0^{t_y} G_y(\tau) y d\tau \right)} dx dy. \quad (2.58)$$

Assuming temporal constant gradient fields G_x and G_y , the exponential terms for frequency and phase encoding can be written as $\gamma G_x t x$ and $\gamma G_y t y$, respectively. These terms can be understood as wave numbers of a Fourier transform. Introducing two wave numbers,

$$k_x = \gamma \int_0^{t_x} G_x(\tau) d\tau \quad (2.59)$$

and

$$k_y = \gamma \int_0^{t_y} G_y(\tau) d\tau, \quad (2.60)$$

simplifies Eq. 2.58 to

$$S(t, \vec{k}) = S_0 \int_x \int_y M_{\perp}(0)^{i(k_x \cdot x + k_y \cdot y)} dx dy. \quad (2.61)$$

The sampled data in this experiment can be interpreted as sampling of the wave numbers k_x and k_y in the Fourier space, usually referred to as k-space [Ljunggren, 1983, Twieg, 1983]. By varying the area under the gradient-time-curve different points in the k-space can be reached and sampled. Therefore the trajectory in k-space is determined by the modulation of the gradients (Eqs. 2.59 and 2.60). To visualize the modulation of gradients and RF-pulses in MRI-sequences, so-called *pulse diagrams* are used (Fig. 2.14). To calculate the transverse magnetization, an inverse Fourier transform of the raw data (Eq.2.61) has to be taken which leads to the following expression,

$$M_{\perp}(\vec{r}) = \frac{1}{S_0 \cdot (2\pi)^2} \cdot \int_x \int_y S(t, \vec{k}) \cdot e^{-i(k_x x + k_y y)} dk_x dk_y. \quad (2.62)$$

Equation 2.62 is the fundamental equation of MRI. Since M_{\perp} is a complex quantity, it is possible to reconstruct magnitude images as well as phase images.

2.3.3 Discrete Sampling of k-Space

In practice, it is impossible to sample the whole k-space continuously and infinitely, but only a discrete number of points. To describe this phenomenon, it is helpful to interpret the sampled signal as a multiplication of the continuous signal with a sampling function $u(k)$ in k-space. Considering the convolution theorem, a multiplication in k-space equals the convolution of the Fourier transforms of both products in image space. This means that the reconstructed image, M_{sample} , is the convolution of the original object, $M_{\perp}(\vec{r})$, and the inverse Fourier transform of the sampling function, $U(\vec{r})$,

$$M_{\text{sample}}(\vec{r}) = M_{\perp}(\vec{r}) \otimes U(\vec{r}). \quad (2.63)$$

In Cartesian k-space sampling, the signal is digitized while a constant frequency encoding gradient (here in x -direction) is switched on. During the duration of this constant gradient G_x , N_x data points with a distance Δk_x are sampled in time intervals of Δt . In phase encoding direction (here y -direction), discrete sampling is realized by incremental changing of the gradient amplitude ΔG_y . This results in the following k-space sampling density,

$$\Delta k_x = \gamma G_x \Delta t_x, \quad (2.64)$$

$$\Delta k_y = \gamma \Delta G_y t_y. \quad (2.65)$$

The resulting digitalized signal S_{sample} can be described as a multiplication of the continuous signal $S(t)$ (Eq. 2.61) with the sampling function $u(k)$ which can be written as a

train of equally spaced delta functions, called *Dirac comb* or *Shah function* III [Bracewell, 1999]. The one-dimensional Shah function can be written as

$$u(k_i) = {}^1\text{III} \left(\frac{k_i}{\Delta k_i} \right) = \Delta k_i \sum_{n=-\infty}^{+\infty} \delta(k_i - n\Delta k_i), \quad (2.66)$$

and for the two-dimensional case as

$$u(k_x, k_y) = {}^2\text{III}(k_x, k_y) = {}^1\text{III}(k_x) {}^1\text{III}(k_y). \quad (2.67)$$

Therefore the sampled signal can be written as

$$S_{\text{sample, dis}}(t, \vec{k}) = S(t, \vec{k}) \cdot {}^2\text{III} \left(\frac{k_x}{\Delta k_x}, \frac{k_y}{\Delta k_y} \right) \frac{1}{\Delta k_x \Delta k_y}. \quad (2.68)$$

$S_{\text{sample, dis}}(t, \vec{k})$ describes the infinite, discrete sampled signal. The two-dimensional Fourier transform into spatial domain yields, by considering the convolution theorem, to a convolution of the Fourier transform of the sampling function and the continuous signal. Therefore Eq. 2.63 turns into

$$M_{\text{sample}}(\vec{r}) = M(\vec{r}) \otimes \mathcal{F}^{-1} \left[{}^2\text{III} \left(\frac{k_x}{\Delta k_x}, \frac{k_y}{\Delta k_y} \right) \right] \frac{1}{\Delta k_x \Delta k_y}. \quad (2.69)$$

The Fourier transform of the Shah function is also a Shah function, but with a reciprocal distance between the peaks (Fig. 2.12):

$$\mathcal{F}^{-1} \left[{}^2\text{III} \left(\frac{k_x}{\Delta k_x}, \frac{k_y}{\Delta k_y} \right) \right] = {}^2\text{III} \left(\frac{\Delta k_x}{2\pi} x, \frac{\Delta k_y}{2\pi} y \right) \frac{\Delta k_x \Delta k_y}{4\pi^2} \quad (2.70)$$

Using Eqs. 2.69 and 2.70, the resulting sampled magnetization for the one-dimensional case can be written as

$$M_{\text{sample}}(\vec{r}) = M_{\perp}(\vec{r}) \otimes \sum_{m=-\infty}^{+\infty} \delta \left(x - \frac{m \cdot 2\pi}{\Delta k_x} \right). \quad (2.71)$$

Here, it is preconditioned that the sampling function is not limited spatially which is an unrealistic precondition in practice that will be discussed in the section 2.3.4. The convolution of the continuous signal with the Shah function leads to a periodical replication of the image with a periodicity of $\frac{2\pi}{\Delta k_x}$ and $\frac{2\pi}{\Delta k_y}$ in x - and y -direction, respectively (Fig. 2.12). This is the reason why the spatial dimension is limited by the so-called *Field of View* (FOV),

$$\text{FOV}_x = \frac{2\pi}{\Delta k_x}. \quad (2.72)$$

$$\text{FOV}_y = \frac{2\pi}{\Delta k_y} \quad (2.73)$$

If a fraction of the investigated object exceeds the limitation by the FOV, artifacts in the image occur. In this case, the part of the object that is cut off at one side of the FOV is illustrated at the opposite side of the FOV, due to the periodicity of the Shah

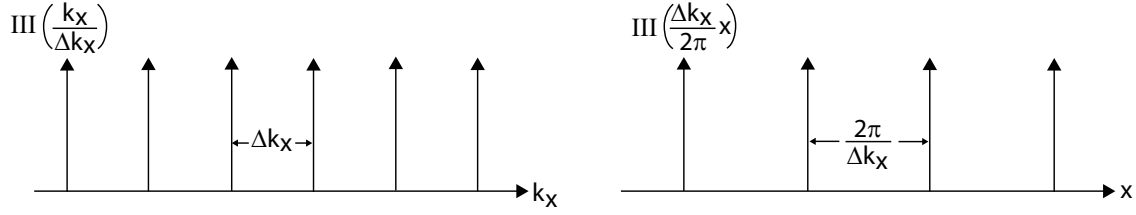


Figure 2.12 Shah function. Dirac comb in the frequency domain (left) and in the spatial domain.

function. This overlapping is also called *aliasing* artifact. Commonly, Eqs. 2.72 and 2.73 can be combined to the following condition:

$$\Delta k \leq \frac{2\pi}{FOV} \quad (2.74)$$

Because the FOV in x - and y -direction can be described as N_x steps of Δx and N_y steps of Δy , respectively, the combination of Eqs. 2.64, 2.65 and 2.74 yields the following sampling criteria,

$$\Delta t_x \leq \frac{2\pi}{\gamma G_x N_x \Delta x}, \quad (2.75)$$

$$\Delta G_y \leq \frac{2\pi}{\gamma t_y N_y \Delta y}. \quad (2.76)$$

Equations 2.75 and 2.76 are equivalent to the Nyquist sampling theorem [Nyquist, 1928] which states that a signal is only exactly reconstructible if the sampling frequency is at least twice as large as the maximum signal frequency [Shannon, 1949].

2.3.4 Image Resolution

In the previous section, it was assumed that the sampling function is of infinite length in k -space. In a real MRI experiment, this is not realizable. In the following, a Cartesian grid is assumed with a fix number of grid points, N_x and N_y , in frequency and phase encoding direction, respectively. That is the reason why the k -space is limited from $-k_i^{\max}$ to k_i^{\max} , with

$$k_i^{\max} = \frac{1}{2} N_i \Delta k_i \quad \text{for } i = x, y. \quad (2.77)$$

To realize the idea of a discrete, finite signal $S_{\text{sample, dis, fin}}$, the discrete, infinite signal (Eq. 2.68) is multiplied by two rectangular functions in x - and y direction¹:

$$S_{\text{sample, dis, fin}}(t, \vec{k}) = S(t, \vec{k}) \cdot \text{III} \left(\frac{k_x}{\Delta k_x}, \frac{k_y}{\Delta k_y} \right) \frac{1}{\Delta k_x \Delta k_y} \cdot \Pi \left(\frac{k_x + \Delta k_x/2}{2k_x^{\max}} \right) \cdot \Pi \left(\frac{k_y + \Delta k_y/2}{2k_y^{\max}} \right). \quad (2.78)$$

The resulting image can be calculated by the Fourier transform of this signal which results in a convolution of the Fourier transform of the discrete, infinite signal (Eq. 2.71) with the

¹The rectangular function is shifted by $\Delta k_i/2$, because the sampling function is chosen to have a sampling point in the origin of the k -space, and an even number of sampling points is assumed.

point spread function (PSF). In this case, it is the Fourier transform of the rectangular functions which is a two-dimensional sinc function.

$$M_{\text{sample, dis, fn}}(x, y) = \left\{ M(x, y) \otimes \left[\sum_{m=-\infty}^{+\infty} \delta\left(x - \frac{m \cdot 2\pi}{\Delta k_x}\right) \sum_{m=-\infty}^{+\infty} \delta\left(y - \frac{m \cdot 2\pi}{\Delta k_y}\right) \right] \right\} \cdot 2k_x^{\text{max}} 2k_y^{\text{max}} \otimes \text{sinc}(k_x^{\text{max}} x) \text{sinc}(k_y^{\text{max}} y) \quad (2.79)$$

Considering a point in the image space, the PSF causes a broadening of this point in the image. The full width at half maximum (FWHM) of a sinc-shaped PSF is here π/k_i^{max} , which is, considering Eqs. 2.72, 2.73 and 2.77, equal to FOV_i/N_i , which coincides with the distance between two adjacent pixels in image space. Since the FWHM of the main maximum is well below this value, the resolution of a MR image is defined as the distance between two pixels,

$$\Delta x = \frac{FOV_x}{N_x} = \frac{2\pi}{\gamma G_x \Delta t_x N_x} \quad (2.80)$$

$$\Delta y = \frac{FOV_y}{N_y} = \frac{2\pi}{\gamma \Delta G_y t_y N_y}. \quad (2.81)$$

Equations 2.80 and 2.81 show that an increased sampling time t_x and a stronger readout gradient G_x lead to a higher image resolution in x -direction. Assuming the number of samples as constant, this will reduce the FOV_x . In analogy to this, an increment of t_y or G_y leads to a reduction of FOV_y if N_y is kept constant. The relation between k-space and image space is presented in Fig. 2.13. The convolution of the image with a sinc function leads to ring-shaped artifacts in the region of sharp edges in the image. This artifact is called *Gibbs-Ringing* [Folland, 1992]. To avoid this, a smoothing filter could be used that suppresses high frequency components. The disadvantage of this technique is a broadening of the PSF resulting in a worse image resolution.

2.3.5 Imaging Methods

In heterogeneous biological tissues like the human body, there are several possibilities to create tissue contrast. The reason for this is not only the different spin density in different areas of the tissue (Tab. 2.3) but also the different relaxation times (Tab. 2.2).

In MRI, there is a large variety of image contrasts due to different k-space trajectories caused by variation of the strength and duration of the gradients and RF-pulses. The

Table 2.3 Water content of various human tissues. Table adapted from Mansfield [1988].

Tissue	Water (%)	Tissue	Water (%)
Skeletal muscle	79.2	Bone	12.2
Heart	80.0	Blood	93.0
Liver	71.1	Cerebrospinal fluid	97.5
Kidney	81.0	Pancreatic juice	98.7
Brain, white matter	84.3	Urine	98.7
Brain, gray matter	70.6	Sweat	99.5

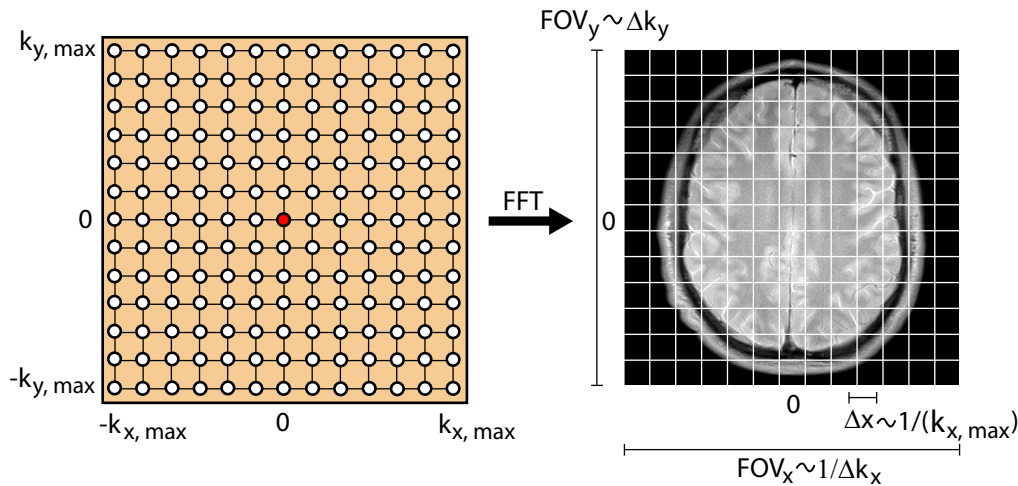


Figure 2.13 Schematic view of the relationship between k -space and image space. The signal, measured at specific values of k_x and k_y are arranged in a matrix, called k -space. The complex data is transformed from the k -space into the image space by Fourier analysis.

timetable of the variation in time of the gradients and RF-pulses is called (*pulse*) *sequence*. To enable fast image reconstruction, most of the pulse sequences sample the data on a Cartesian grid with 2^n grid points in each encoding direction. In the following, the two fundamental types of MR pulse sequences are presented, the spin echo sequence and the gradient echo sequence. There exist much more pulse sequences, but all other sequences are variations of these two sequences.

2.3.5.1 Spin Echo Sequence

Figure 2.14 shows a spin echo (SE) sequence imaging scheme. First, a combination of a 90° RF-pulse and a slice selection gradient flips the magnetization inside the desired slice into the transverse plane. Subsequently, the slice selection gradient G_y is switched on. At the same time the so-called *dephasing gradient* G_x is switched on. At the time $TE/2$, the 180° refocusing RF-pulse is applied, creating a spin echo at the echo time TE that is acquired while switching on a rephasing read-out gradient G_x . This has to be repeated for each k_y -step in k -space, i.e. N_y times. For every repetition, a different phase encoding gradient strength has to be used. The time between two excitations is called *repetition time* (TR). Since each line in k -space has to be acquired with the same initial conditions, the system has to be in equilibrium. Therefore the longitudinal magnetization has to recover to its equilibrium state before the next excitation can be applied. This results in a long TR and, therefore, in a long acquisition time (TA) which is a big disadvantage in clinical MRI.

2.3.5.2 Gradient Echo Sequence

At the beginning of MRI, the spin echo sequence was used to suppress the magnetic field inhomogeneities. Although good results were obtained, the disadvantages of a long TR has led to limitations for further research. Within the years, the MRI hardware improved

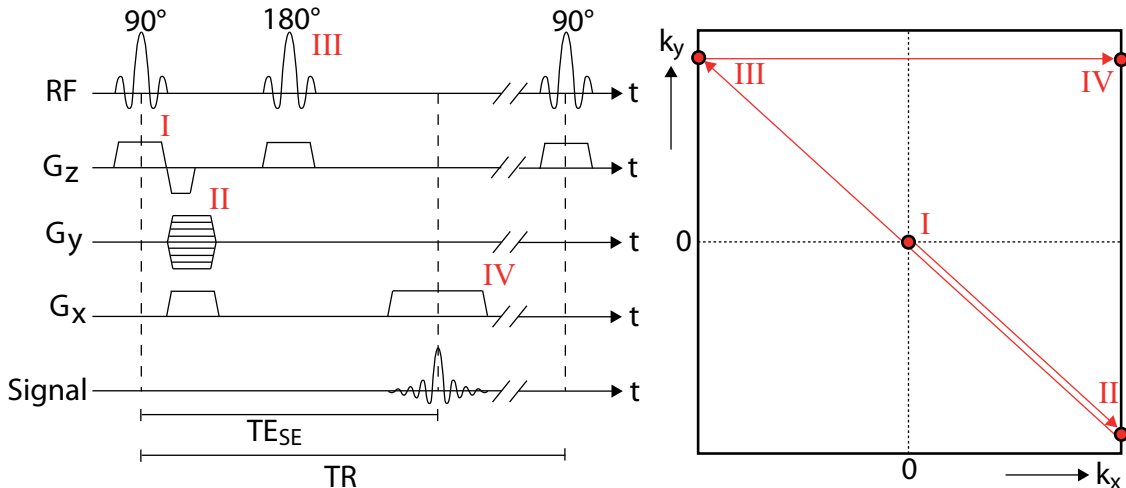


Figure 2.14 Spin Echo sequence and corresponding k-space trajectory. On the left picture, a schematic spin echo pulse sequence is presented, highlighting the four time points I, II, III and IV. The right picture shows the progress of the trajectory for the different times. At first, a 90° pulse leads to the k-space center (I). The phase encoding gradient G_y and the dephasing gradient G_x leads to the right end of the k-space. The particular k_y -line depends on the chosen gradient strength G_y (II). The following 180° pulse reverses the effect of the gradients (III). Finally, the read-out gradient initiates the sampling of the particular k-space line (IV). This procedure is repeated for different amplitudes of the phase encoding gradient, until the k-space is completely sampled.

and, therewith, the homogeneity of the main magnetic field over a large FOV. This has enabled image acquisitions without a refocusing pulse, enabling many possibilities for different kinds of pulse sequences. The most important pulse sequence is the so-called *gradient echo sequence* (GRE, Fig. 2.15). Here, the signal is dephased by means of gradients, before the signal read-out. Subsequently, the rephasing gradient G_x causes an echo at the echo time TE . The most important advantage of this technique is that small flip angles could be used resulting in a shorter recovering time for the longitudinal magnetization. The result is a much faster sequence with a lower SNR because a small flip angle means that less of the magnetization is flipped into the transverse plane and, therefore, less signal can be detected. The corresponding imaging sequence is called *FLASH* (Fast Low Angle SHot) [Frahm et al., 1986].

2.3.5.3 Echo Planar Imaging (EPI)

The two previous sequences enable data acquisition of one line in k-space with each RF excitation, for each phase encoding step. In 1977, Mansfield [1977] developed a technique which allows data acquisition of the whole k-space with only one excitation pulse (Fig. 2.16). After the 2D excitation, two dephasing gradients in phase and readout direction cause a movement of the trajectory into the corner of the k-space ($k_x = -k_{x,max}$, $k_y = k_{y,max}$). Now, the readout gradient is switched on. If the end of one line is reached, a small gradient in phase encoding direction (called *blip*) is applied, and the readout gradient is switched on with the same strength as in the line before but with opposite polarity. This procedure continues until the whole k-space is sampled. Because of the

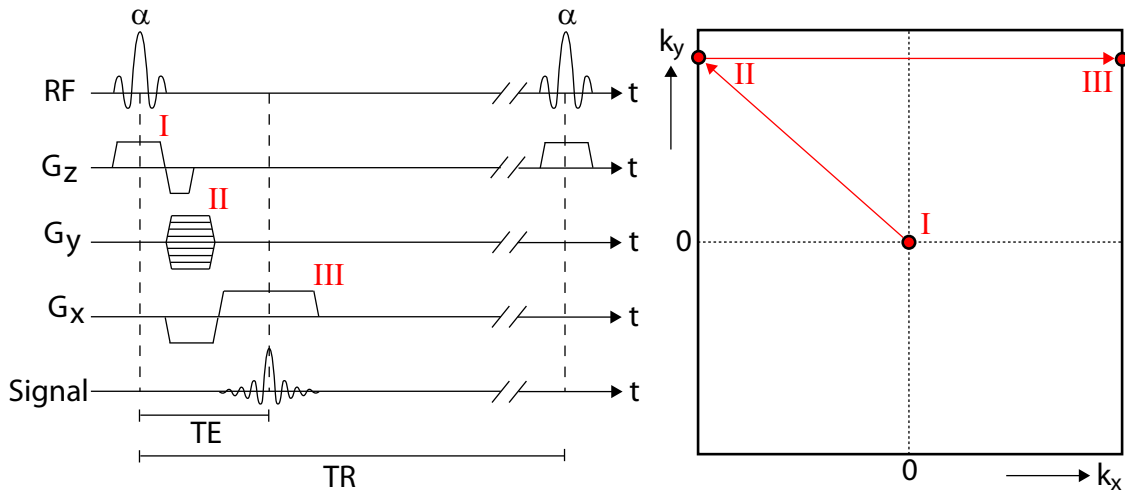


Figure 2.15 Gradient echo sequence and corresponding k-space trajectory. On the left picture, a schematic gradient echo pulse sequence is presented, highlighting the three time points I, II and III. The right picture shows the progress of the trajectory for the different times. At first, during the slice selection gradient a HF-pulse with a flip angle of α is applied. α is usually between 10° and 90° (I). Subsequently, a phase encoding gradient G_y and a dephasing gradient G_x in frequency encoding direction are applied (II). The dephased signal is rephased in readout direction by the subsequent rephasing gradient that has an inverted polarity with respect to the dephasing gradient (III). A gradient echo occurs at TE , where the signal is maximum. While the rephasing gradient is switched on, the data is sampled. The TR is much shorter than in a spin echo experiment resulting in a shorter TA.

high technical requirements this technique could only be realized many years later in the last decade of the 20th century. With this technique, the data acquisition is finished after 50 – 100 ms, which is of the same order as T_2^* of brain tissue (Tab. 2.2). This is the reason why T_2^* constrains the trajectory in k-space because the number of samples that could be acquired is limited by this time. This technique has three main disadvantages: Firstly, the limited number of sampled points leads to a (compared to other techniques) bad image resolution, typically of $3 \times 3 \times 3 \text{ mm}^3$. Secondly, this technique is very sensitive to magnetic field inhomogeneities, which leads to signal loss. Thirdly, the required high bandwidth (compared to the FLASH-technique) leads to a loss in SNR. The main advantage of the EPI is the possibility of acquiring images in a very short period of time, which enables the possibility to detect signal changes of the oxygenation state of the venous blood.

2.3.6 Image Contrast

In MRI, a contrast between different structures is produced. This contrast can have different origins. The choice of the sequence parameter TE and TR play an important role for the resulting image contrast. By varying these parameters, certain tissue structure change their contribution to the signal intensity due to different T_1 and T_2 times. Here, three examples for different contrasts, i.e. weightings, are presented:

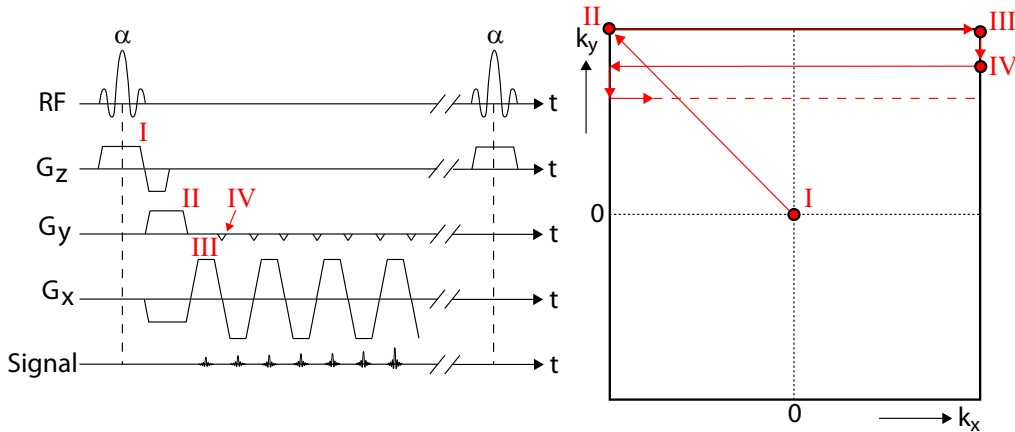


Figure 2.16 EPI sequence. After the slice selective excitation pulse (I), the k-space trajectory moves to the corner of the k-space by two large gradients in frequency and phase encoding direction (II). Afterwards, the readout gradient is switched on and k-space data is acquired. At the end of the k-space line (III) a small gradient in phase encoding direction (*blip*) is switched on resulting in a movement of the trajectory into the next line (IV). Now, the readout gradient is switched on again, but with the opposite polarity compared to the previous line. With this method, the whole k-space can be sampled with only one excitation pulse resulting in a very short acquisition time.

2.3.6.1 T_1 -Weighted Contrast

To get a T_1 -weighted image, it is important to adjust a short repetition time. This can be explained with the fact that different tissues have different T_1 times, and a short repetition time results in a different relaxation of the tissue. The shorter the T_1 time is, the more of the longitudinal magnetization is relaxed during TR . The following RF pulse causes a higher signal for a tissue with a short T_1 . Moreover, it is important to keep TE short because otherwise a T_2 -weighted contrast would be generated.

2.3.6.2 T_2 -Weighted Contrast

In this case, the different T_1 times should not have an impact on the image contrast. Therefore, TR has to be very long, to enable a complete relaxation of the longitudinal magnetization of the different tissues. Typically, TR is in the order of some seconds. To get the best T_2 contrast between two different tissues, the echo time TE has to be between the transverse relaxation times of these investigated tissues (Tab. 2.2).

2.3.6.3 Spin Density Contrast

For long TR and short TE , the longitudinal magnetization of the different tissues is able to relax completely, and, directly after the excitation pulse, the different T_2 times of the different tissues do not have an impact on the contrast because the echo time is much shorter than the T_2 time of the tissues. If there is still a contrast between tissues, it results from the different spin density in the tissues. In this case, the contrast is given by the spatial distribution of the hydrogen nuclei.

Figure 2.17 shows an overview of the mentioned contrasts in MRI.

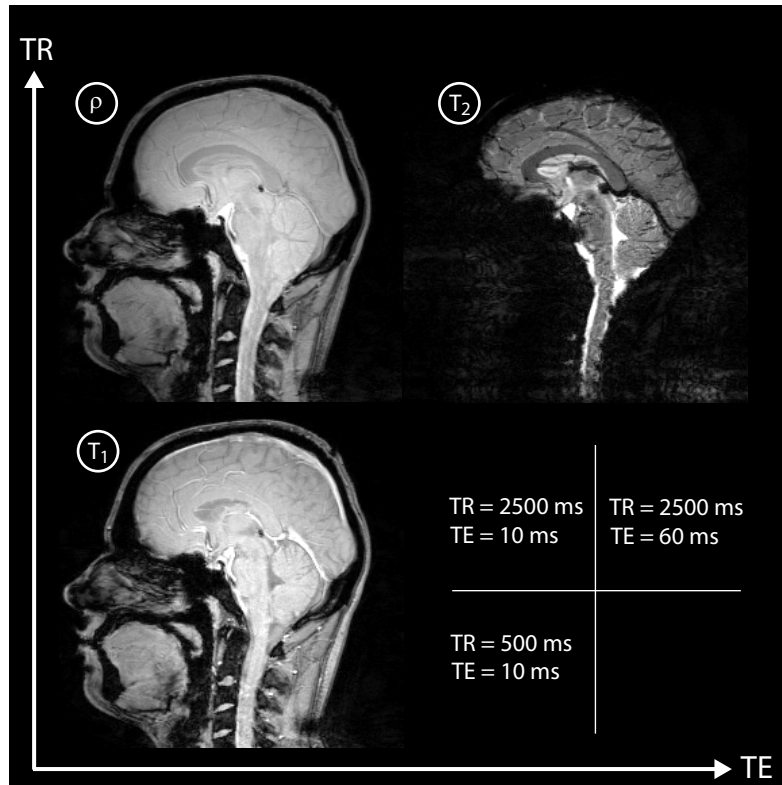


Figure 2.17 Three contrasts in MRI. A short TR and a short TE cause a T_1 -weighted image. Keeping TE short while increasing TR causes a spin density-weighted contrast. A T_2 -weighted image can be recorded by adjusting a long TR and a long TE .

2.4 Physiological Properties of Blood

The cells inside the different tissues of the human body need energy to maintain their vital functions. They get the energy by degradation of nutrients. This degradation requires the presence of glucose, proteins and molecular oxygen. The blood in the vessels is responsible for the glucose and oxygen supply.

2.4.1 Oxygen Transport in the Blood

Human blood consists of blood plasma and blood cells. The blood plasma consists of about 90% water and 10 % dissolved proteins, glucose, mineral ions, hormones and carbon dioxide. The blood cells consist of white blood cells (leucocytes), platelets (trombocytes) and red blood cells (erythrocytes). The white blood cells are responsible for defending the body against both infectious diseases and foreign materials. The platelets play an important role in hemostasis and are a natural source of growth factors. During hemostasis, they lead to the formation of blood clots. White blood cells and platelets are about 4% of the blood cells. The remaining fraction of the blood cells (about 96 %) consist of red blood cells. Their main task is the oxygen transport in the body. The volume fraction of blood cells in the body is called hematocrit (Hct). This value varies from person to person and is usually in the range of 0.40 - 0.43 for healthy grown

up females and about 0.44 - 0.46 for healthy grown up males [Schmidt and Thews, 1995]. The erythrocytes do not only transport molecular oxygen, but also carbon dioxide (CO_2). The transport can be realized by the oxygen affine protein hemoglobin inside the erythrocytes. One single erythrocyte consists of about $3 \cdot 10^8$ hemoglobin molecules. The oxygen molecule is bound to the Fe^{2+} ion in the hemoglobin. Since the Fe^{2+} ion is not changing its oxidation status during this process, the bounding process is called *oxygenation*, not oxidation. Hemoglobin consists of four polypeptid subunits. Each of these subunits consists of an organic molecule with a Fe^{2+} ion in its center, called *heme molecule*. The most common heme molecule is called heme A and is presented in Fig. 2.18. It consists of a porphyrin molecule with the iron molecule in its center. Hemoglobin occurs with and without a bound oxygen molecule and is called oxyhemoglobin (HbO_2) and deoxyhemoglobin (Hb), respectively. A common expression for the oxygen saturation is the blood oxygenation level Y . This is the ratio between oxygenated hemoglobin concentration and total hemoglobin concentration,

$$Y = \frac{[\text{HbO}_2]}{[\text{HbO}_2] + [\text{Hb}]} \quad (2.82)$$

The probability of a reversible binding of the oxygen at the iron ion depends on the oxygen partial pressure pO_2 of the blood. The relationship between Y and pO_2 shows an empirically found sigmoidal behavior [Stryer, 1998],

$$Y = \frac{(pO_2)^{2.8}}{(pO_2)^{2.8} + (p_{0.5})^{2.8}}, \quad (2.83)$$

where $p_{0.5}$ is the oxygen partial pressure of the blood at half oxygen saturation ($Y = 0.5$). Under normal physiological conditions this value is equal to 3.6 kPa. Figure 2.19 shows a typical oxygen saturation curve of a healthy adult.

2.4.2 Tissue Oxygen Consumption

The oxygen consumption of the tissue can be quantified by the metabolic rate for oxygen (MRO_2). The definition of this rate is the ratio between the absolute oxygen consumption per tissue mass and time,

$$\text{MRO}_2 = \frac{\text{O}_2\text{-consumption}}{\text{tissue mass} \cdot \text{time}} \quad \left[\frac{\text{mol}}{\text{g} \cdot \text{s}} \right]. \quad (2.84)$$

In addition to the absolute oxygen consumption, described by MRO_2 , the oxygen extraction fraction (OEF) is of great interest. It describes the ratio of consumed oxygen in the tissue and delivered oxygen by the blood [Golay et al., 2001],

$$\text{OEF} = \frac{\text{O}_2\text{-consumption}}{\text{O}_2\text{-delivery}}. \quad (2.85)$$

Inserting the difference of the hemoglobin concentration of the arterial and the venous blood for the O_2 -consumption, Eq. 2.85 can be transformed to

$$\text{OEF} = \frac{[\text{HbO}_2, \text{arterial}] - [\text{HbO}_2, \text{venous}]}{[\text{HbO}_2, \text{arterial}]} = 1 - \frac{Y_{\text{venous}}}{Y_{\text{arterial}}}. \quad (2.86)$$

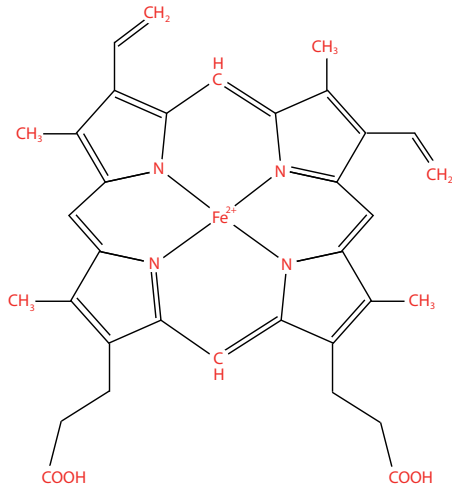


Figure 2.18 Heme molecule. It consists of four pyrrole rings, building a porphyrin ring. The iron ion in its center is able to bind the four nitrogen atoms of the pyrrole rings. Moreover, the iron ion is bound to another polypeptid chain. The remaining binding is used for reversible oxygen adsorption. Hemoglobin consists of four polypeptid subunits, each hosting a heme molecule.

Since arterial blood is approximately 100% O_2 saturated, Eq. 2.86 can be simplified to:

$$OEF = 1 - Y_{\text{venous}}. \quad (2.87)$$

In the human body, different organs have different OEF values. Moreover, the OEF depends on the actual state of stress. For example, skeletal and myocardial muscles have an OEF of about 40 – 60 % in the resting state. This value rises up to 90 % at physical stress [Schmidt and Thews, 1995]. In a resting human brain, the OEF is approximately 0.4-0.5. There can be an increment of the OEF caused by pathophysiological conditions. For example, a tumor can have a different oxygen demand than healthy tissue. The

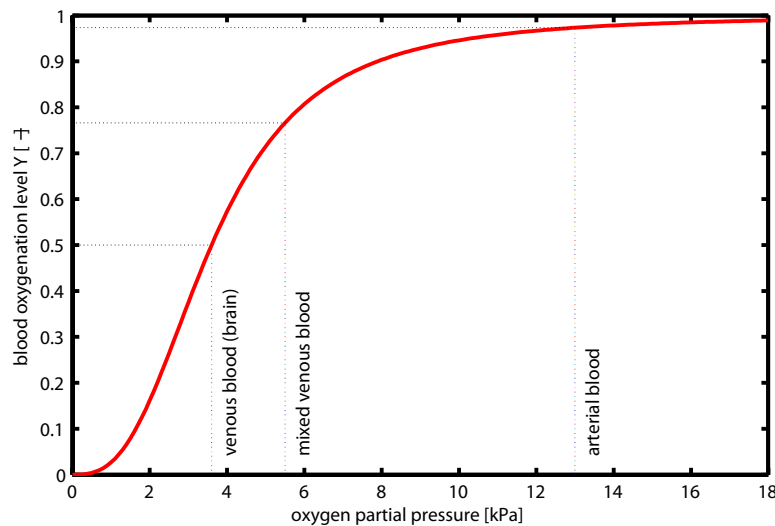


Figure 2.19 Oxygen saturation curve of hemoglobin. The highlighted values represent normal values for arterial blood ($Y \approx 97.5\%$), mixed venous blood ($Y \approx 76.7\%$) and venous blood ($Y \approx 50\%$) in the brain. This curve represents the values for a healthy adult under normal conditions ($pH = 7.4, T = 37^\circ C$).

metabolic rate for oxygen depends on the OEF, the oxyhemoglobin concentration in the arterial blood and the blood flow (BF),

$$\text{MRO}_2 = \text{OEF} \cdot \text{BF} \cdot \text{HbO}_{2, \text{arterial}}. \quad (2.88)$$

Equation 2.88 shows that the body has different possibilities to increase the metabolic rate for oxygen: Either the blood flow or the OEF has to be increased, or both. For example, an oxygen demand in the myocardium which was increased up to four times the resting state value, can be satisfied by increasing the blood flow by four times [Schmidt and Thews, 1995].

2.4.3 Oxygenation Dependent Magnetic Properties of Blood

The twofold oxidized iron ion in the center of the heme molecule has six electrons in the 3d orbitals resulting in four unpaired electrons and two paired electrons. The existing ligand field in the heme molecule causes a splitting of the energy level of the 3d z^2 and $x^2 - y^2$ orbitals from the energy level of the xy , yz and xz orbitals. The energy levels are not degenerated anymore, but the presence of the spins in all orbitals is still the state with the lowest energy. During oxygenation the ligand field increases and the gap between the two orbital groups rises. Since the previous distribution of the spins is not energetically favorable anymore, the two electrons of the high energy state fall into the state of the low energy resulting in 6 paired electrons (Fig. 2.20). A quantum mechanical analysis reveals that the total spin of the system has changed from $S = 2$ (deoxyhemoglobin) into $S = 0$ (oxyhemoglobin). This is the reason why deoxyhemoglobin is paramagnetic and hemoglobin is diamagnetic. The magnetic moment of deoxyhemoglobin has already been found by Pauling and Coryell [1936].

Macroscopically, this procedure appears as a continuous change of the magnetic susceptibility χ_{blood} , which consists of the susceptibility of the erythrocytes χ_{ery} and the susceptibility of the blood plasma χ_{plasma} ,

$$\chi_{\text{blood}} = \text{Hct} \cdot \chi_{\text{ery}} + (1 - \text{Hct}) \cdot \chi_{\text{plasma}}. \quad (2.89)$$

The susceptibility of the erythrocytes is composed of the susceptibility of the oxygenated erythrocytes and the deoxygenated erythrocytes,

$$\chi_{\text{ery}} = Y \cdot \chi_{\text{ery, ox}} + (1 - Y) \cdot \chi_{\text{ery, deox}}, \quad (2.90)$$

where $\chi_{\text{ery, ox}}$ and $\chi_{\text{ery, deox}}$ denote the magnetic susceptibility of red blood cells that are completely oxygenated and completely deoxygenated, respectively. The susceptibility of blood plasma is similar to that of water at 37°C [Schenck, 1996]:

$$\chi_{\text{plasma}} \approx \chi_{\text{H}_2\text{O}(37^\circ\text{C})} = -9.05 \text{ ppm}. \quad (2.91)$$

Because the volume susceptibility of fully oxygenated blood is about -9.25 ppm [Weisskoff and Kiihne, 1992], it is justified to equalize these two values. With the introduction of a value for the difference between the magnetic susceptibility of completely deoxygenated erythrocytes and completely oxygenated erythrocytes,

$$\Delta\chi_{\text{do}} = \chi_{\text{ery, deox}} - \chi_{\text{ery, ox}}, \quad (2.92)$$

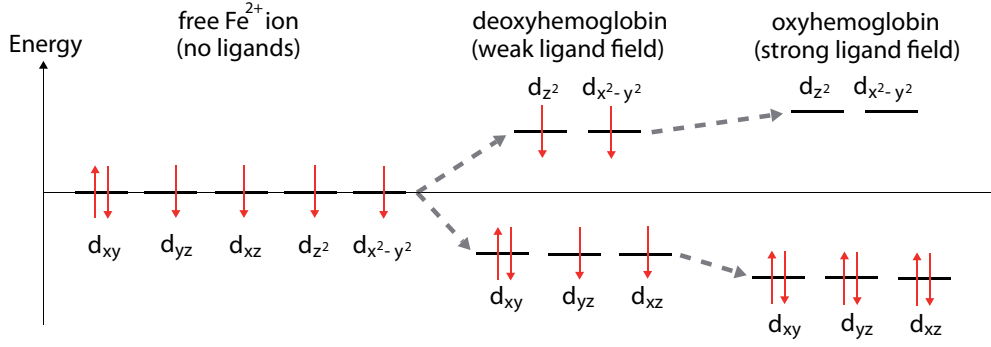


Figure 2.20 Energy states of the 3d orbitals of the iron ion. When no ligand field is present (free iron ion, left), the energy levels are degenerated. In the deoxyhemoglobin a weak ligand field is present. This results in a splitting of the different energy levels. Although two orbitals have now a higher energy level, the favorable electron configuration is still the same. The unpaired electrons give rise to a permanent magnetic dipole moment. This results in paramagnetic properties. In the case of oxyhemoglobin, the energy gap is so high that the electron configuration is not energetically favorable anymore and spin coupling becomes energetically favorable. In this case, heme becomes diamagnetic.

Eq. 2.89 can be simplified to

$$\chi_{\text{blood}} = \chi_{\text{ery, ox}} + \text{Hct} \cdot (1 - Y) \cdot \Delta\chi_{\text{do}}. \quad (2.93)$$

Blood vessels are usually embedded in soft tissue. Therefore the susceptibility difference of tissue and vessels are of interest. With the justified assumption that the susceptibility of soft tissue and fully oxygenated blood cells is nearly equal [Schenck, 1996], the susceptibility difference between blood and tissue $\Delta\chi$ can be written as

$$\Delta\chi = \text{Hct} \cdot (1 - Y) \cdot \Delta\chi_{\text{do}} \approx \text{Hct} \cdot \text{OEF} \cdot \Delta\chi_{\text{do}}. \quad (2.94)$$

The literature value of $\Delta\chi_{\text{do}}$ varies a little. While Weisskoff and Kiihne [1992] measured a value of 2.26 ppm, some years later, Spees et al. [2001] obtained a slightly higher value of 3.39 ppm. Moreover it is assumed that Hct in small vessels is about 15% smaller than in larger vessels [An and Lin, 2000]. Since Hct and $\Delta\chi_{\text{do}}$ are constants, Eq. 2.94 shows the linear dependence of the OEF on the susceptibility difference between tissue and blood.

2.4.4 Microscopic Vascular Anatomy of the Brain

Most of the *in vivo* experiments presented in this work were performed in the brain. One reason for this is the high physiological interest of the oxygen metabolism in the brain. Another reason is that this organ is very well suited for MRI. This is the case because there are hardly any susceptibility effects caused by interfaces or movement artifacts. The largest vessels in the blood vessel network in the brain are the intracortical supplying arteries (120 – 240 μm) and the draining veins (80 – 120 μm). The arterioles and venules that are connected with the arteries and veins, respectively, are even smaller (30 – 40 μm). The capillary network where the oxygen supply of the tissue happens has a radius distribution of 4 – 20 μm . Figure 2.21 shows two images of the vessel network recorded by an electron microscope. A dense vessel network is responsible for a good

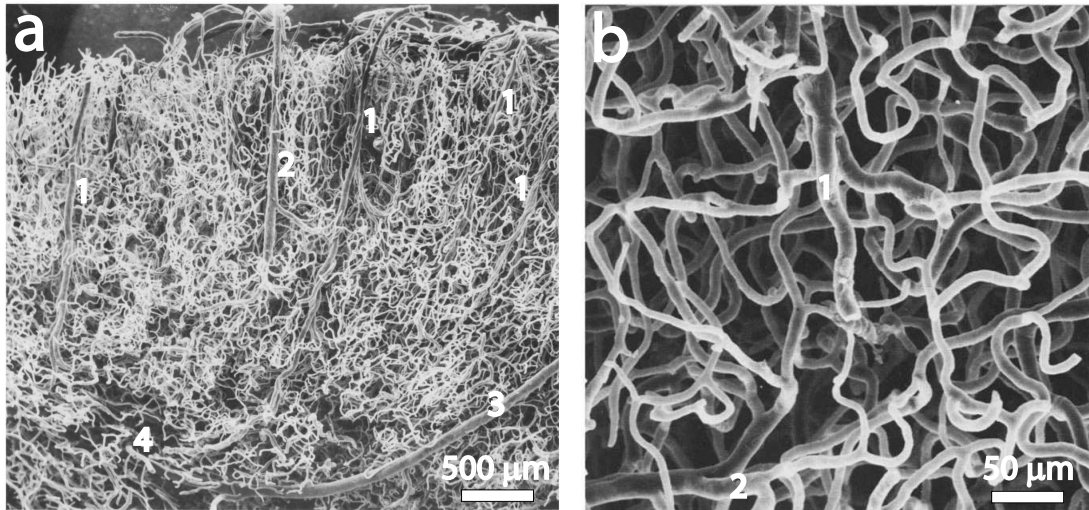


Figure 2.21 Cortical blood vessel network recorded by an electron microscope. The images show the different vessel sizes of an artery of gray matter (1), a vein of gray matter (2), an artery of white matter (3) and smaller vessels of the white matter (4). Figure adopted from Duvernoy et al. [1981].

oxygen supply to the gray matter in the brain, and the gray matter has a higher vessel density than the white matter. This difference between cerebral blood volume (CBV) in gray and white matter was first determined by Yamaguchi et al. [1986] using positron emission tomography (PET). They found a blood fraction of 4.3 ml in 100 g cortical gray matter and 2.1 ml in 100 g white matter. There exist many studies concerning the measurement of the CBV. While, for example, Newman et al. [2003] reproduced the aforesaid results using a T_2^* -weighted method with paramagnetic contrast agent, the absolute results of other studies are varying. Nevertheless, the blood volume ratio between gray and white matter of 2:1 can be found in most of the studies. Moskalenko [1980] measured the venous part of the blood volume in dogs and found a volume fraction of 0.7 of the whole cerebral blood volume. This fact is worth being mentioned because this venous (deoxygenated) blood volume fraction is used in later MR signal calculations.

2.5 Susceptibility Weighted Imaging (SWI) of the Kidney

In this section, a method is described which enables visualization of the oxygenation by using the SWI contrast. Most of the work in this field was done for brain imaging. One part of this work was to implement this technique on kidney imaging which is a big challenge.

2.5.1 Physiological Background and Clinical Applications

Susceptibility differences can be visualized with susceptibility weighted imaging (SWI) by also using phase information in addition to magnitude images [Haacke et al., 2004, Rauscher et al., 2006]. Till now, SWI is applied to the cerebrum, primarily to enhance image contrast of veins [Reichenbach et al., 1997, 2000]. Venous vessels show a higher

susceptibility difference in comparison to the surrounding tissue due to the high concentration of deoxygenated hemoglobin. Besides mere visualization of venous vessels in the cerebrum [Reichenbach et al., 1998], SWI was furthermore applied to the imaging of strokes [Hermier and Nighoghossian, 2004, Deistung et al., 2006], hemorrhages [Tong et al., 2004], and cerebral tumors [Barth et al., 2003]. As SWI contrast depends on the fraction of deoxygenated hemoglobin in blood, an indirect assessment of tissue oxygenation would be a further possible application. Hence, after having implemented SWI on normal kidneys in a first step, SWI of renal tumors and assessment of the response to chemotherapy is planned next. To our knowledge, implementation of SWI on the kidney has not been attempted yet. In comparison to cerebral imaging, in renal imaging different problems have to be solved: On the one hand, one has to cope with respiratory and bulk motion due to peristaltics leading to pronounced artifacts. Therefore the acquisition time should be as short as possible. On the other hand, the kidney shows different oxygen consumption with a higher oxygen fraction in the venous vessel system than in the cerebral veins. Thus, the susceptibility difference between the venous vessels and the surrounding tissue is not as pronounced as in the brain. The aim of this work was to implement SWI on the kidney assuming that through variation of the phase mask even small susceptibility differences become visualizable.

The kidneys play an important role in the control of blood pressure as well as in homeostasis by selectively excreting or retaining various substances [Schoenberg et al., 1997]. There are many diseases leading to an impaired function of the kidney, particularly longstanding diabetes mellitus and renal artery stenosis, but also acute and chronic rejection after renal transplantation [Michaely et al., 2008]. T_2^* weighted MRI is a tool in the diagnostic work-up of kidney diseases allowing for the assessment of organ function [Mendichovszky et al., 2008, Nissen et al., 2010].

2.5.2 SWI-Theory

Depending on the oxygenation level of the blood, the oxy-to-deoxy-hemoglobin ratio changes. Whereas oxyhemoglobin and the surrounding tissue are diamagnetic, deoxyhemoglobin is paramagnetic. Thus, the lower the blood oxygenation level in a vascular network becomes, i.e. the more deoxyhemoglobin is present, the higher the susceptibility differences between vessels and surrounding tissue are [Bauer et al., 1999]. In MRI, this effect is used for imaging as the susceptibility of venous blood in a vascular network creates a susceptibility contrast: In the following, it is assumed that the arterial blood is fully oxygenated. According to Eq. 2.94, the absolute change of the magnetic susceptibility $\Delta\chi$ consists of three factors: The hematocrit value of the subject Hct , the susceptibility difference between fully deoxygenated and fully oxygenated blood $\Delta\chi_{do}$, and the OEF. Depending on the vessel orientation to the main magnetic field, there are extravascular magnetic field inhomogeneities around the vessel (c.f. section 3.1.1). These inhomogeneities in the magnetic field ΔB cause a local phase shift $\Delta\varphi$ which is proportional to the echo time TE ,

$$\Delta\varphi = -\gamma \cdot TE \cdot \Delta B. \quad (2.95)$$

This local phase shift is the basis of SWI [Haacke et al., 2004]. From the recorded complex-valued MR signals, usually a magnitude image is reconstructed, neglecting any available phase information. In contrast, in SWI, this extra information is used to enhance the

corresponding magnitude image by creating a so-called *phase mask*. This phase mask usually shows a linear relationship between the phase value and the mask value. For a typical positive phase mask the mask value for all phase values $\Delta\varphi$ smaller than zero are set to one. The mask values for phase values larger than zero are linearly scaled from one to zero (for phase values from 0 to π). By n times multiplication of the magnitude image with the phase mask the image gets a weighting, where the parts of the brain where $\Delta\varphi$ differs from zero (in inhomogeneous regions, e.g. regions of deoxygenated blood) create a new image contrast in the susceptibility weighted image. The choice of the phase mask and the number of multiplications n are the determining parameters of the resulting image.

2.5.3 Data Processing

2.5.3.1 Standard SWI Reconstruction / Phase Masks

Magnitude and phase images were reconstructed from the 3D raw data set using commercial post-processing software provided by the scanner manufacturer (SWI package, Siemens, Germany). Susceptibility weighted images are a combination of magnitude and phase images. A challenge in creating susceptibility weighted images is the choice of a suitable phase mask, i.e. the weighting function, by which the magnitude images are multiplied. There are three typical phase masks, M: negative, positive and triangular [Reichenbach and Haacke, 2001]. In the case of a positive phase mask, all negative phase values are set to 1, whereas all other values are linearly scaled,

$$M = \begin{cases} 1 & \text{for } \varphi < 0, \\ 1 - \varphi/\pi & \text{for } 0 \leq \varphi \leq \pi, \end{cases} \quad (2.96)$$

The other masks can be created accordingly. A suitable phase mask should be chosen and multiplied pixel-wise with the original magnitude picture. In this study, similar to brain imaging, a positive phase mask is used. The susceptibility weighted image I_{sw} can be written as

$$I_{\text{sw}} = I_{\text{mag}} \cdot M^n, \quad (2.97)$$

where I_{mag} is the magnitude image and n is typically between 3 and 5 [Reichenbach et al., 1998]. Here, $n = 4$ was used. There are two ways to improve image quality: Zero-filling in k-space or interpolation in image space. In this work, latter is used and triple bilinear interpolation was applied. The standard SWI reconstruction does not generate a good contrast in kidney imaging, which is caused by much smaller phase values in the kidney than in the brain (Fig. 4.20c). This is the reason why the reconstruction for kidney imaging was enhanced by changing the shape of the phase mask.

2.5.3.2 Enhanced SWI Reconstruction for Kidney Imaging

Due to very small phase variations in the kidney compared to the brain, it is either useful to change the phase mask or to increase the number of multiplications n with the phase mask M (Eq. 2.97). In this work, both possibilities were investigated. At first, different mask multiplications ($n = 4$, $n = 8$) were compared. As a next step, a new phase mask

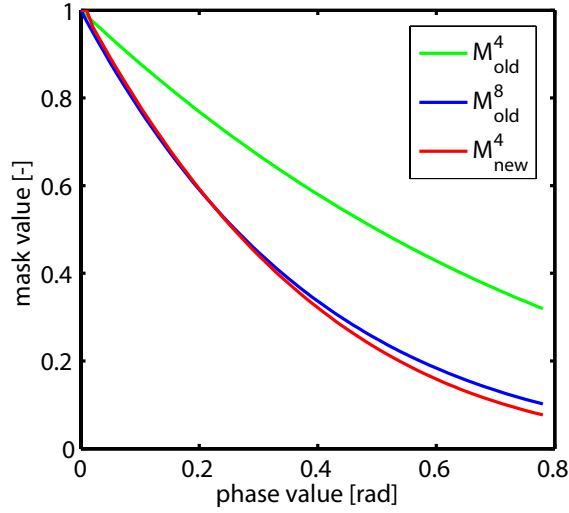


Figure 2.22 Phase dependence of different phase masks. For small phase values, the standard phase mask M_{old} with 8 multiplications looks very similar to the new phase mask M_{new} with 4 multiplications.

was created by altering the slope of the commonly used mask (Eq. 2.96). The slope was doubled resulting in the following phase mask (Fig. 2.22),

$$M^* = \begin{cases} 1 & \text{for } \varphi < \varphi_t, \\ 1 - 2 \cdot (\varphi - \varphi_t)/\pi & \text{for } \varphi_t \leq \varphi \leq \pi/2, \\ 1 & \text{for } \pi/2 < \varphi, \end{cases} \quad (2.98)$$

where φ_t is the phase threshold value. A threshold value $\varphi_t = 0.02$ for very small phase values is introduced to ensure that the susceptibility weighted image is not falsified by small phase fluctuations around zero, i.e. noise. Furthermore, all phase values larger than $\pi/2$ were set to one. This is reasonable because absolute phase values due to susceptibility effects of veins in the kidney are well below $\pi/2$.

3 Materials and Methods

3.1 Modeling Blood Vessels in the Brain

In this section, the modeling of a blood vessel network in the brain is described. Since the magnetic field distribution, caused by the vessel network, is of great interest, it is useful to understand the exact origin of this distribution. The easiest way to understand this is to start with a magnetic field distribution around a single paramagnetic vessel in a homogeneous medium and to transfer this knowledge to a vessel network.

3.1.1 Single Vessel in Homogeneous Tissue

To describe a straight single vessel, a model of an infinitely long homogeneous paramagnetic cylinder seems to be appropriate. Assuming a susceptibility difference $\Delta\chi$ between this vessel and the surrounding tissue, the vessel causes a magnetic field change ΔB outside and inside the vessel. Ogawa et al. [1993] showed that the magnetic field distribution depends on the vessel radius R and the vessel orientation angle θ to the magnetic field,

$$\Delta B = \begin{cases} \frac{\Delta\chi}{2} \cdot \sin^2 \theta \cdot R^2 \cdot \frac{\cos 2\varphi}{r^2} \cdot B_0 & \text{for } r > R, \\ \frac{\Delta\chi}{6} \cdot (3 \cos^2 \theta - 1) \cdot B_0 & \text{for } r < R, \end{cases} \quad (3.1)$$

where r and φ are the distance and the azimuthal angle in a plane orthogonal to the cylinder (Fig. 3.1). It is useful to introduce the characteristic frequency shift $\delta\omega$, which is the maximum frequency offset at the cylinder surface,

$$\delta\omega = \frac{\Delta\chi\gamma B_0}{2}. \quad (3.2)$$

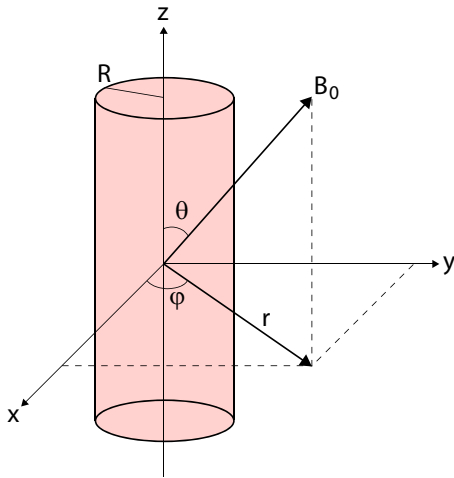


Figure 3.1 Cylinder in an external magnetic field. The position of the cylinder can be described by the parameters r , φ and θ , which is the angle between the cylinder axis and the external magnetic field.

With Eqs. 3.1 and 3.2 it is possible to express the frequency shift $\Delta\omega$ inside and outside the cylinder as

$$\Delta\omega = \begin{cases} \delta\omega \cdot \frac{R^2}{r^2} \cdot \sin^2 \theta \cdot \cos 2\varphi & \text{for } r > R, \\ \delta\omega \cdot \frac{1}{3} \cdot (3 \cos^2 \theta - 1) & \text{for } r < R. \end{cases} \quad (3.3)$$

It can be seen that the maximum field offset at the surface of the cylinder is only dependent on B_0 and the susceptibility difference between the cylinder and the surrounding medium. The radius of the vessel determines the spatial extend of the field distortions, whereas the orientation of the vessel to the magnetic field is responsible for the shape of the frequency distribution outside and inside the vessel. Figure 3.2 shows three interesting cases for vessel orientations. The first case shows a vessel parallel to the magnetic field ($\theta = 0^\circ$) resulting in a vanishing frequency shift outside the cylinder and the maximum frequency shift inside the cylinder. The second case is a vessel perpendicular to the magnetic field ($\theta = 90^\circ$), where $\Delta\omega$ inside the cylinder reaches its minimum and the absolute values of the $\Delta\omega$ outside its maximum. The third interesting case is, when $\Delta\omega$ inside the cylinder becomes zero (i.e. $3 \cos^2 \theta = 1$). The corresponding angle ($\theta = 54.74^\circ$) is called *magic angle*.

3.1.2 Partial Volume Effect

Heterogeneous biological probes consist of different tissue types, e.g. water and fat or blood vessels and surrounding tissue. Considering a blood vessel network embedded in a homogeneous medium, the total signal from this voxel can be separated into an intravascular part \vec{S}_{int} and an extravascular part \vec{S}_{ext} . The total signal \vec{S} is the sum of these two compartments,

$$\vec{S} = \lambda \cdot \vec{S}_{\text{int}} + (1 - \lambda) \cdot \vec{S}_{\text{ext}}, \quad (3.4)$$

where λ is the volume fraction occupied by the vessel network.

3.1.3 Analytical Solution for MR Signal Decay in the Presence of a Paramagnetic Cylinder

The analytical expression for a signal from a voxel with a single cylinder in the surrounding medium has been derived by Yablonskiy and Haacke [1994]. It is given by

$$S(t) = S(0) \cdot \left(1 - \frac{\lambda}{1 - \lambda} \cdot f_c(\delta\omega_\theta) + \frac{1}{1 - \lambda} \cdot f_c(\lambda \cdot \delta\omega_\theta \cdot t) \right), \quad (3.5)$$

where $\delta\omega_\theta$ denotes the characteristic frequency shift for the cylinder,

$$\delta\omega_\theta = \frac{\Delta\chi\gamma B_0}{2} \cdot \sin^2 \theta, \quad (3.6)$$

and the characteristic function f_c is given by

$$f_c(\varphi) = \int_0^1 \frac{1 - J_0(\varphi \cdot u)}{u^2} du, \quad (3.7)$$

where J_0 is the zeroth order Bessel function.

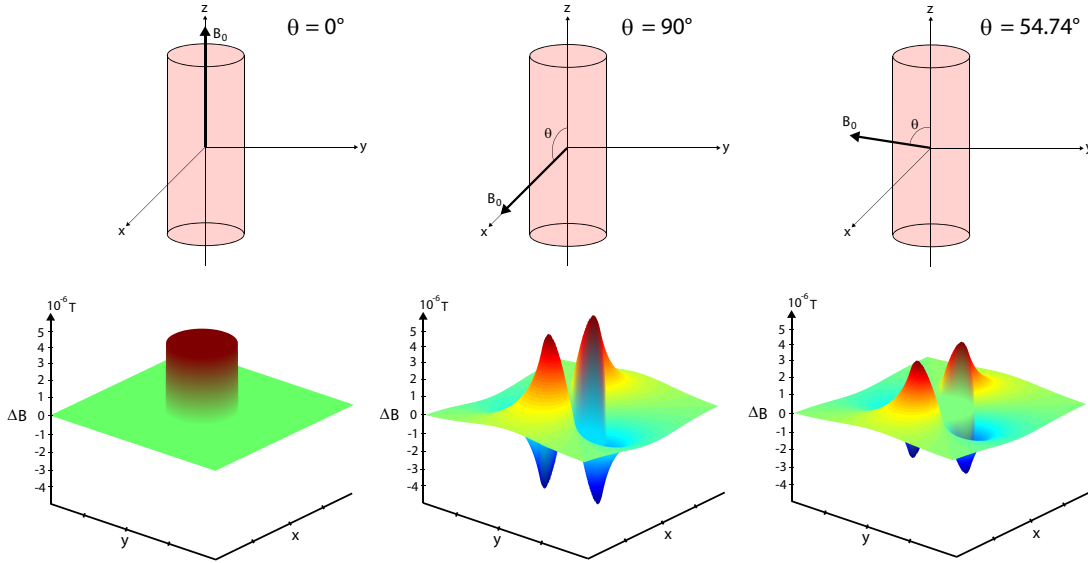


Figure 3.2 Magnetic field distribution around a paramagnetic vessel with different orientations. **Left:** If the vessel is located parallel to the external magnetic field, the extravascular field changes vanish. **Middle:** If the vessel is placed perpendicular to the magnetic field (in this case B_0 is aligned with the x -axis) the extravascular magnetic field distortions become maximal. **Right:** The magic angle: The magnetic field inside the vessel is equal to the homogeneous part outside the vessel. ΔB denotes the magnetic field change relative to the external field. In this simulation, a magnetic field strength of 3 T and a susceptibility difference of 4.5 ppm are assumed.

3.1.4 Blood Vessel Network in Homogeneous Tissue

The simulation of a blood vessel network requires some assumptions. First, randomly spatial distributed cylinders are assumed, which is justified by having a look at typical vessel diameter (c.f. section 2.4.4) and typical voxel sizes of 1 mm^3 . This Lorentzian distribution results in an exponential signal decay (c.f. section 2.2.7). Secondly, this model does not allow too high blood volume fractions ($\lambda < 5\%$), because statistical distribution of the cylinders allows overlapping, which can not be found in a real vessel network. The radii of the blood vessels do not have an influence on the signal decay inside a voxel. Therefore the signal decay depends only on the blood volume λ and the susceptibility difference $\Delta\chi$ between blood and surrounding tissue. Moreover, the following calculations accomplished by Yablonskiy and Haacke [1994] neglect the signal contribution originating from the vessels, which is a justified assumption for a low blood volume ($\lambda < 5\%$). The regime, where signal decay due to inner voxel spin dephasing occurs before molecular diffusion averages out the phases, is called *static dephasing regime*. High magnetic fields, big susceptibility differences and large vessels favor the static dephasing regime.

For the simulation of a cylinder network, the average over the randomly distributed cylinders is necessary. The following calculations can be found more detailed in the works of Yablonskiy and Haacke [1994], Kiselev and Posse [1999] and Sedlacik [2007]. The signal

from a voxel can be written as

$$S(t) = e^{-t/T_2} \cdot \int_{\vec{r}} S_0(\vec{r}) e^{-i\Delta\omega(\vec{r}) \cdot t} d\vec{r}, \quad (3.8)$$

where $\Delta\omega$ is the local deviation from the readout frequency and $S_0(\vec{r})$ the spin-density dependent basic signal fraction. Equation 3.3 shows the frequency shift for a cylinder. Since only spins outside the cylinders are considered and a homogeneous spin distribution is assumed ($S_0(\vec{r}) = S_{0,\text{ext}}$), Eq. 3.8 can be simplified to

$$S_{\text{ext}}(t) = (1 - \lambda) \cdot S_{0,\text{ext}} \cdot e^{-t/T_2} \prod_{n=1}^N \langle \Psi_n \rangle, \quad (3.9)$$

where N is the number of cylinders and Ψ_n is the extravascular signal of the n^{th} cylinder. Averaging over all orientations of the isotropically distributed cylinders leads to an integration over the cylinder orientation θ with a distribution function $(\sin\theta)/2$, as well as an integration over φ and r with the uniform distribution function $1/(A - \pi R^2)$ [Kiselev and Posse, 1999]. A is the cross-sectional area of the voxel and πR^2 is the cross section of the cylinder. With the magnetization density function

$$\Psi = e^{-i\Delta\omega(\vec{r}) \cdot t} \quad (3.10)$$

that can be calculated from the Bloch equations, the averaged effect of the cylinders can be written as

$$\langle \Psi_n \rangle = \int_0^\pi d\theta \frac{\sin\theta}{2} \int_0^{2\pi} d\varphi \int_R^\infty dr \frac{r}{A} \cdot e^{-i\Delta\omega(\vec{r}) \cdot t}. \quad (3.11)$$

Eq. 3.11 can then be transformed into

$$\langle \Psi_n \rangle = 1 - \frac{\pi R^2}{A} \int_0^\pi d\theta \frac{\sin\theta}{2} \int_0^{2\pi} d\varphi \int_R^\infty dr \frac{r}{\pi R^2} \cdot \left(1 - e^{-i\Delta\omega(\vec{r}) \cdot t}\right). \quad (3.12)$$

The assumption of a small volume fraction occupied by a single cylinder compared to the whole volume, $(\pi R^2)/A$, turns Eq. 3.12 into the following approximation,

$$\langle \Psi_n \rangle = 1 - \frac{\pi R^2}{A} \int_0^\pi d\theta \frac{\sin\theta}{2} \int_0^{2\pi} d\varphi \int_R^\infty dr \frac{r}{\pi R^2} \cdot \left(1 - e^{-i\Delta\omega(\vec{r}) \cdot t}\right) \approx 1. \quad (3.13)$$

Therefore Eq. 3.13 can be written as an exponential function,

$$\langle \Psi_n \rangle = \exp \left[-\frac{\pi R^2}{A} \int_0^\pi d\theta \frac{\sin\theta}{2} \int_0^{2\pi} d\varphi \int_R^\infty dr \frac{r}{\pi R^2} \cdot \left(1 - e^{-i\Delta\omega(\vec{r}) \cdot t}\right) \right] \approx 1. \quad (3.14)$$

The substitution of Eq. 3.14 in Eq. 3.9 yields the following signal equation

$$\ln \left[\frac{S_{\text{ext}}}{(1 - \lambda) \cdot S_{0,\text{ext}} \cdot e^{-t/T_2}} \right] = \lambda \int_0^\pi d\theta \frac{\sin\theta}{2} \int_0^{2\pi} d\varphi \int_R^\infty dr \frac{r}{\pi R^2} \cdot \left(1 - e^{-i\Delta\omega(\vec{r}) \cdot t}\right), \quad (3.15)$$

where

$$\lambda = \frac{\pi R^2 N}{A} \quad (3.16)$$

is the volume fraction occupied by all cylinders. For a numerical integration the substitution

$$u = \frac{R^2}{r^2} \quad (3.17)$$

and the according differential

$$dr = -\frac{r^3}{2R^2} du \quad (3.18)$$

is used. Equation 3.15 can now be expressed as ($r = R \rightarrow u = 1, r = \infty \rightarrow u = 0$)

$$\ln \left[\frac{S_{\text{ext}}}{(1 - \lambda) \cdot S_{0,\text{ext}} \cdot e^{-t/T_2}} \right] = \lambda \int_0^\pi d\theta \frac{\sin \theta}{2} \int_0^{2\pi} d\varphi \int_1^0 \frac{r^3}{-2R^2} du \frac{r}{\pi R^2} \cdot \left(1 - e^{-i\Delta\omega(\vec{r}) \cdot t} \right). \quad (3.19)$$

The back substitution $r^4 = R^4/u^2$ turns the signal equation into

$$\ln \left[\frac{S_{\text{ext}}}{(1 - \lambda) \cdot S_{0,\text{ext}} \cdot e^{-t/T_2}} \right] = \lambda \int_0^\pi d\theta \frac{\sin \theta}{2} \int_0^{2\pi} d\varphi \int_0^1 du \frac{1}{2\pi u^2} \cdot \left(1 - e^{-i\Delta\omega(\vec{r}) \cdot t} \right). \quad (3.20)$$

Now the external signal equation can be written as

$$S_{\text{ext}} = (1 - \lambda) \cdot S_{0,\text{ext}} \cdot e^{-t/T_2} \cdot e^{-\lambda \cdot f_c(\delta\bar{\omega} \cdot t)}, \quad (3.21)$$

where f_c is the characteristic function for the network of randomly distributed cylinders. Yablonskiy and Haacke [1994] simplified this complicated expression, which allows faster numerical integration:

$$f_c(\delta\bar{\omega} \cdot t) = \frac{1}{3} \cdot \int_0^1 du \cdot (2 + u) \cdot \sqrt{1 - u} \cdot \frac{1 - J_0(1.5 \cdot \delta\bar{\omega} \cdot t \cdot u)}{u^2}, \quad (3.22)$$

where J_0 is the Bessel function of order zero. The argument of f_c consists the mean characteristic frequency shift for the cylinder network

$$\delta\bar{\omega} = \frac{4\pi}{3} \cdot \gamma \cdot \Delta\chi \cdot B_0. \quad (3.23)$$

Although Eq. 3.21 has no analytical solution, it is possible to distinguish two different time regimes, the short-term regime and the long-term regime. The short-term regime predicts a Gaussian field distribution (section 2.2.7) resulting in a biexponential signal amplitude. The long-term regime predicts a Lorentzian magnetic field distribution in the voxel, which leads to a monoexponential signal amplitude,

$$S(t) = (1 - \lambda) \cdot S(0) \cdot e^{-0.3\lambda(\delta\bar{\omega} \cdot t)^2} \cdot e^{-t/T_2} \quad \text{for} \quad |\delta\bar{\omega} \cdot t| < 1.5, \quad (3.24)$$

$$S(t) = (1 - \lambda) \cdot S(0) \cdot e^{-\lambda(\delta\bar{\omega} \cdot t - 1)} \cdot e^{-t/T_2} \quad \text{for} \quad |\delta\bar{\omega} \cdot t| \geq 1.5. \quad (3.25)$$

Therefore the transition time t_c between these two regimes can be expressed as

$$t_c = \frac{1.5}{\delta\bar{\omega}}. \quad (3.26)$$

It can be seen that the short-term regime becomes shorter for an increasing field strength B_0 .

3.2 MR Techniques

In this section, the MR hardware and the corresponding software are described. Different MR imaging sequences used in this work are explained. At the end of this section the MR phantoms that were used for different experiments are presented.

3.2.1 MR Scanners

All measurements were carried out on a Siemens MR scanner with a field strength of 3T (Magnetom Trio, Siemens Medical Healthcare, Erlangen, Germany, Fig. 3.3a) at the university hospital in Mannheim, Germany. This system uses a sequence developing environment called *IDEA* (Integrated Development Environment for Applications). For brain imaging, the signal was acquired using a standard birdcage 12-channel head coil (Fig. 3.3b). Abdominal images were acquired using a 6-element phased-array surface coil in combination with a 24-element phased-array spine coil (Fig. 3.3c).

3.2.2 MR Sequences

The MR sequences used in this work are either provided by Siemens or developed with a C++ based sequence development environment (*IDEA*, Siemens, Erlangen, Germany).

3.2.2.1 Gradient Echo Sampled Spin Echo (GESSE)

In section 3.1.4, the influence of a vessel network on the signal intensity was described. The signal is a function of the frequency shift $\delta\omega$ originating from the deoxygenated blood in the vessels. The frequency shift has to be calculated in order to get an idea of the tissue oxygenation. Therefore, the knowledge of the signal behavior around a spin echo is required. Yablonskiy and Haacke [1997] presented a so-called *gradient echo sampled spin echo* (GESSE) sequence that samples the signal around a spin echo. This sequence is similar to the GESFIDE (Gradient Echo Sampling of FID and Echo) method, which allows a simultaneous determination of R_2 and R_2^* [Ma and Wehrli, 1996]. The GESSE sequence is a combination of a spin echo sequence and a gradient echo sequence. Figure 3.4 shows the sequence scheme of the GESSE sequence. After a 90° excitation pulse and the following 180° pulse the signal is sampled by a large number of gradient echoes before and after the spin echo. This results in several images with different echo times acquired during the rephasing and dephasing part of the spin echo. The crusher gradients, that are switched on in slice selection direction before and after the 180° pulse, can compensate refocusing imperfections [Ma and Wehrli, 1996], that could lead to a mixing of R_2 and R_2^* . Possible phase shifts in k-space were avoided by the usage of a mono directional readout [Haacke et al., 1999]. A shortening of the time interval between two adjacent echoes is realizable with an increase of the bandwidth resulting in a lower SNR.

3.2.2.2 Multi-Slice Multi-Echo Gradient Echo (MMGE)

A 3D multi-slice multi-echo gradient echo (MMGE) sequence was used to acquire high resolution phase images. Multi-echo acquisition was performed by sampling the same line in k-space n times after excitation resulting in n echoes. The desired echo time

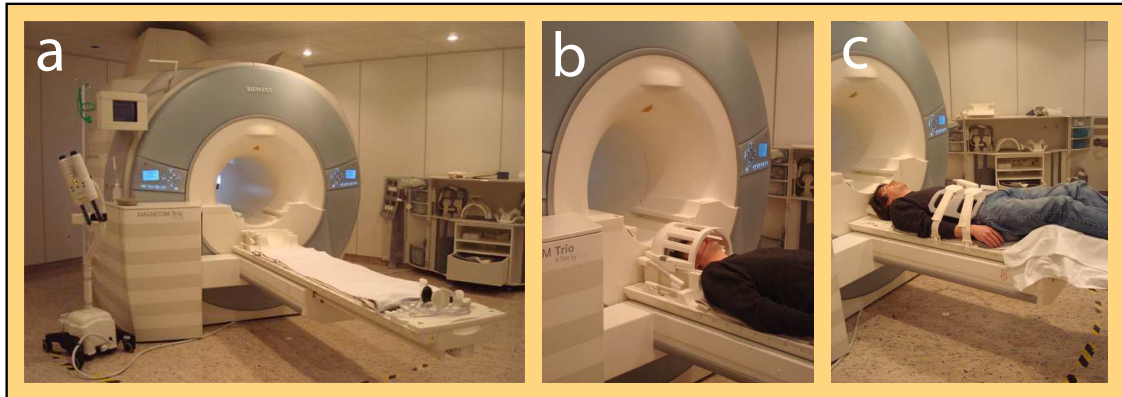


Figure 3.3 MR hardware: Scanner and coils. a) The measurements were performed on a 3 T MRT. The used receiving coils were b) a standard birdcage 12-channel head coil for brain measurements and c) a 6 element phased-array surface coil combined with a 24-element phased-array spine coil.

could be varied. These images have a resolution twice as large as the GESSE sequence in all three dimensions. The phase images reveal information about the macroscopic field inhomogeneities resulting in unwanted signal decay. With a correction algorithm these inhomogeneities could be corrected, further described in section 3.3. Another MMGE sequence with the same image resolution as the GESSE sequence was used for the calculation of R_2^* maps used as an input parameter for the GESSE sequence, further described in section 3.4.3.

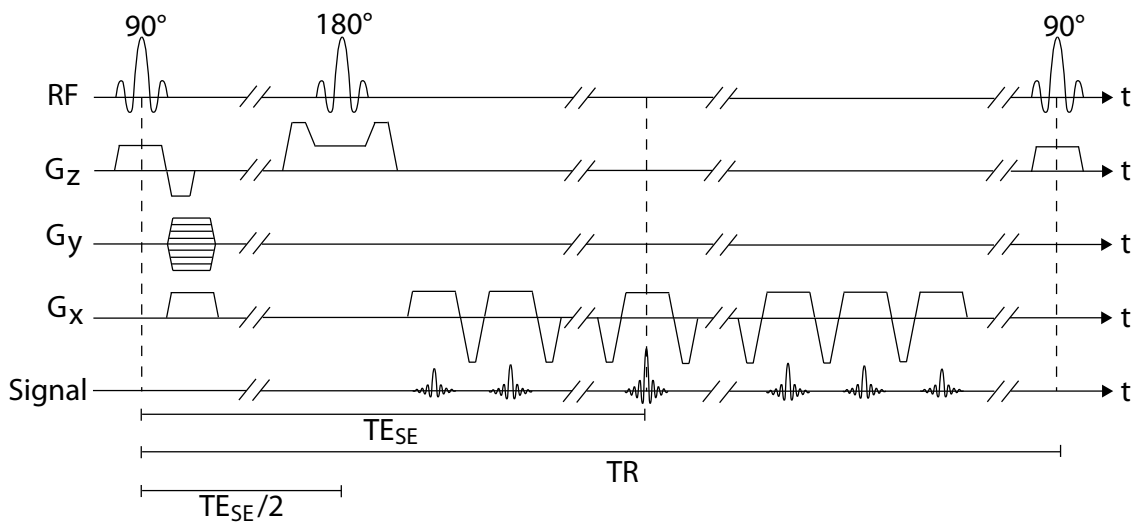


Figure 3.4 Scheme of the gradient echo sampled spin echo (GESSE) sequence. A spin echo occurs at the time TE_{SE} , coinciding with one of the gradient echoes. The signal before and after the spin echo is sampled by gradient echoes.

3.2.2.3 Carr-Purcell-Meiboom-Gill (CPMG)

In section 3.4.3, a method is described, where R_2 and R_2^* values are used as input parameters for the postprocessing of the GESSE data. Therefore the calculation of a R_2 map is necessary. This could be realized by the application of a Carr-Purcell-Meiboom-Gill (CPMG) sequence [Carr and Purcell, 1954, Meiboom and Gill, 1958]. The sequence is a spin echo sequence with several 180° pulses after the 90° excitation pulse, creating several spin echoes at different echo times. These T_2 -weighted images enable the calculation of R_2 maps.

3.2.3 Measurement Phantoms

In this work, different phantoms were used to validate the presented methods. First, a relaxation phantom is presented that was used for sequence comparison and correction, further described in section 4.3.1. As a next step, a tissue phantom was used to validate this sequence correction (section 4.3.2). The third phantom presented here is a flow phantom, which enables linear water flow inside the phantom. This phantom was used for velocity-selective spin labeling measurements, further described in section 3.5.1.6.

3.2.3.1 Relaxation Phantom

For the adjustment and comparison of different imaging sequences, a phantom was used that consisted of different compartments, each filled with distilled water and a different concentration of contrast agent. The contrast agent gadopentetate dimeglumine (or Gd-DTPA) was used, which was the first paramagnetic contrast agent in MRI and is today still the most commonly used contrast agent in clinical routine. The concentrations in the tubes range from pure water to 5 mM. The exact concentration of Gd-DTPA in each tube is illustrated in Fig. 3.5. The tubes are also filled with 1% agar, which makes the content more viscous and shortens the T_1 relaxation time. This enables the usage of a shorter TR resulting in a shorter total measurement time.

3.2.3.2 Tissue Phantom

The second phantom, that was used in this study, is a tissue phantom (Fig. 3.6). This phantom was used to simulate brain tissue with a two-compartment model. It consists of two plastic bottles, filled with distilled water and a 1mM concentration of Gd-DTPA. Two of the bottles are additionally filled with randomly coiled polyamide strings (Polyamide 6-6.6 black, Fa. Krahmer GmbH, Buchholz). The string has a diameter of $93\ \mu\text{m}$. The volume fraction of the strings in the bottles were calculated to 1% and 3%, respectively. With a bottle volume of 293 ml, this results in a string length of 431.3 m and 1294.0 m, respectively. After filling the compounds into the plastic bottle, the phantoms were placed in a vacuum chamber with an air pressure of about 0.3 bar to remove air bubbles inside the phantom. Afterwards, they were placed in an ultrasonic bath until all bubbles were removed.

3.2.3.3 Flow Phantom

A flow phantom was used to simulate different flow velocities in the brain. This consists of a glass box with a tube system inside (Fig. 3.7a). The tube inside the box enables

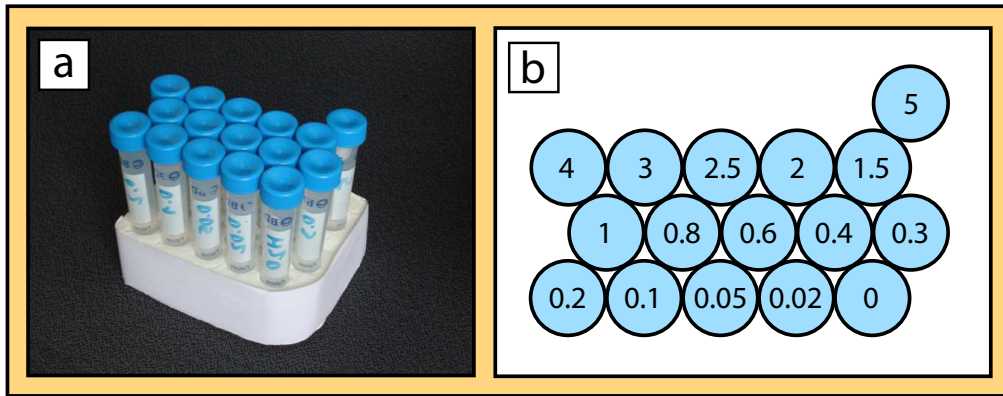


Figure 3.5 Relaxation phantom. a) 16 Tubes with a volume of 17 ml are filled with distilled water, agar and the contrast agent Gd-DTPA. b) The contrast agent concentration (in mM) of the respective tubes.

water flow in three perpendicular directions. The box is connected with long tubes to the adjacent room, where a pump and a water reservoir control the flow inside the box, causing a constant flow. The pump enables the variation of the flow velocity. In this work, a flexible-tube pump (323S/D with pump head 323D, Watson-Marlow Bredel Pumps, Falmouth, Cornwall TR11 4RU, UK) was used, illustrated in Fig. 3.7b.

3.3 Macroscopic Inhomogeneity Correction

In section 3.1, the modeling of a blood vessel network in homogeneous tissue was described. It is assumed that next to the microscopic field inhomogeneities, that cause transverse relaxation, deoxygenated blood vessels are the only source of magnetic field inhomogeneities. This statement is not true since other sources of field inhomogeneities are air/tissue or air/bone interfaces. This results in an unwanted signal decay and a fal-

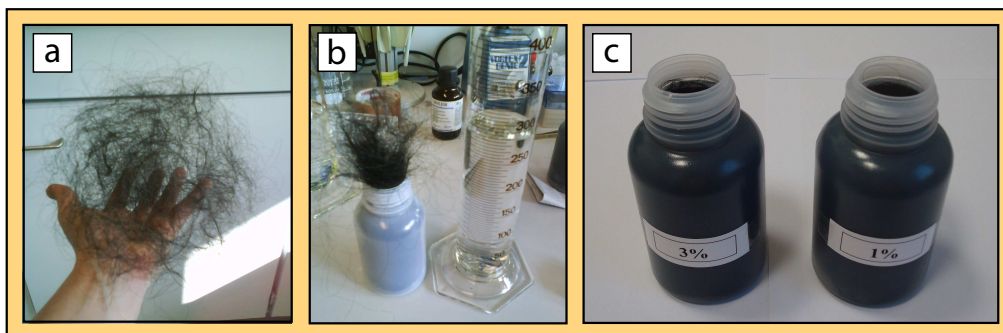


Figure 3.6 Tissue phantom. The image shows the manufacture of the tissue phantom: a) For the phantom with a string volume fraction of 3%, a polyamide string with a length of 1294 m and a diameter of $93 \mu\text{m}$, was randomly coiled. b) The string and the water contrast agent compound were filled into a plastic bottle. c) The two phantoms consist of a string volume fraction of 3% and 1%, respectively.

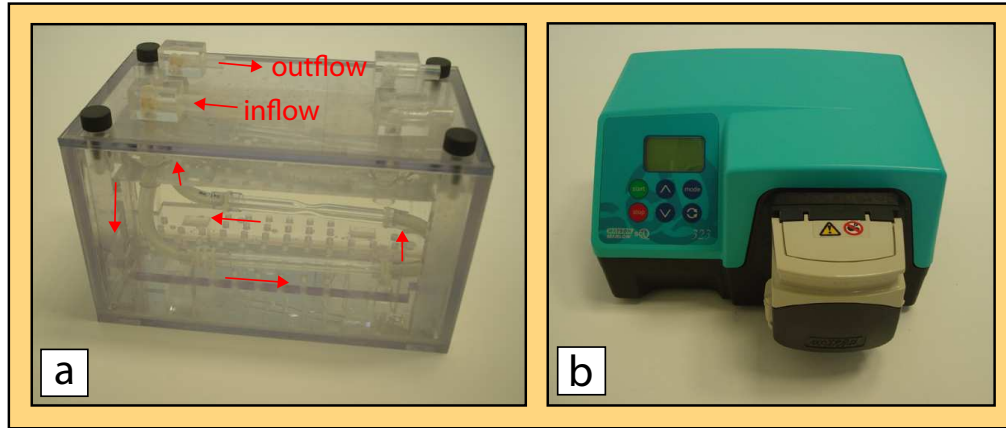


Figure 3.7 Flow phantom and pump. a) The flow phantom is a glass box with two connections for the inflow and the outflow tube. Inside this box a glass tube enables linear flow. This phantom was used for velocity-selective spin labeling measurements (section 3.5.1.6). b) The pump and the water reservoir are placed in another room and are connected with the phantom by long tubes.

sification of the calculation of R'_2 , if the acquired data is not corrected. In this section, a method is presented that enables the separation of the microscopic and the macroscopic field inhomogeneities [Jezzard and Balaban, 1995, Irrarrazabal et al., 1996]. The total magnetic field B_s can be assumed as a superposition of the capillary fields B_{cap} and the macroscopic fields B_{macro} ,

$$B_s = B_{\text{cap}} + B_{\text{macro}}. \quad (3.27)$$

Therefore the signal equation can be written as

$$S(t) \propto \int_V M_{\perp}(0) \cdot e^{i\gamma \cdot (B_{\text{cap}}(\vec{r}) + B_{\text{macro}}(\vec{r})) \cdot t} \cdot e^{-t/T_2} d\vec{r}. \quad (3.28)$$

The signal decay can be split into three contributions, the capillary contribution S_{cap} , the macroscopic contribution S_{macro} and the contribution due to T_2 decay,

$$S(t) = S_{\text{cap}}(t) \cdot S_{\text{macro}}(t) \cdot e^{-t/T_2}. \quad (3.29)$$

With Eqs. 3.28 and 3.29 the macroscopic field contribution can be written as

$$S_{\text{macro}}(t) = \int_{\text{voxel}} d\vec{r} e^{-i\gamma \cdot B_{\text{macro}}(\vec{r}) \cdot t}. \quad (3.30)$$

A known magnetic field distribution $B_{\text{macro}}(\vec{r})$ would make the integral in Eq. 3.30 solvable and S_{macro} could be separated from the rest of the signal equation. In section 2.2.4.2, it was shown that the transverse magnetization can be expressed as a complex quantity,

$$M_{\perp}(\vec{r}, t) = |M_{\perp}(\vec{r}, t)| \cdot e^{i\phi(\vec{r}, t)}, \quad (3.31)$$

where t is the time from the center of the excitation pulse. Equation 3.30 and Eq. 3.31 show the linear relationship between the phase ϕ and the intra-voxel mean magnetic field [Bonny et al., 2000],

$$\phi(\vec{r}, t) = -\gamma \Delta B(\vec{r}) \cdot t + \phi_0(\vec{r}) = -\gamma (B_{\text{macro}} - B_{\text{read}}) \cdot t + \phi_0(\vec{r}), \quad (3.32)$$

where γB_{read} is the readout frequency and $\phi_0(\vec{r})$ the phase at $t = 0$. Equation 3.32 shows that the acquisition of the time course of the complex MR signal provides information about the macroscopic field inhomogeneities $B_{\text{macro}}(\vec{r})$ (Fig. 3.8). Assuming much smaller inhomogeneities than the main magnetic field strength allows the description of the macroscopic field inhomogeneities as a Taylor series,

$$B_{\text{macro}}(r) = B_{\text{macro}}^0 + \frac{\partial B_{\text{macro}}(r_0)}{\partial r}(r - r_0) + \frac{1}{2} \frac{\partial^2 B_{\text{macro}}(r_0)}{\partial r^2}(r - r_0)^2 + \dots \quad (3.33)$$

The first term of Eq. 3.33 leads to a constant phase in the signal, which does not result in any phase dispersion. In contrast to that the second and third term cause a dephasing of the signal. Since the main contribution of this dephasing originates from the linear term, the macroscopic field inhomogeneities can be interpreted as a linear field across the voxel. This linear gradient results in a rectangular distribution function, which leads to a sinc-shaped signal decay S_{macro} (here in x -direction) [Haacke et al., 1999],

$$F_x(t) = \text{sinc} \left(\frac{\gamma \cdot G_{x,\text{macro}} \cdot \Delta x \cdot TE}{2} \right). \quad (3.34)$$

It can be seen that the correction function does not only depend on the echo time TE , but also on the macroscopic gradient $G_{x,\text{macro}}$ in x -direction and the resolution Δx . B_{macro} can be calculated from the experimental data by linear regression to the phase values over the time (Fig. 3.8),

$$B_{\text{macro}} = \frac{1}{\gamma} \frac{d\phi}{dt}. \quad (3.35)$$

Images with different echo times are acquired in the measurement. Now, the gradient maps in all three dimension G_x , G_y and G_z and the respective correction functions F_x , F_y and F_z can be calculated. The resulting total correction function $F_{\text{tot}}(t)$ is the product of the three one-dimensional correction functions,

$$F_{\text{tot}}(t) = F_x(t) \cdot F_y(t) \cdot F_z(t). \quad (3.36)$$

Finally, the original data $\text{Data}_{\text{original}}$ has to be divided by the correction function F_{tot} resulting in macroscopic inhomogeneity corrected data,

$$\text{Data}_{\text{corr}}(t) = \frac{\text{Data}_{\text{original}}(t)}{F_{\text{tot}}(t)}, \quad (3.37)$$

where t can either be the time from the excitation pulse or from the spin echo. A high resolution 3D MMGE sequence (cf. section 3.2.2.2) was used to estimate the distribution $B_{\text{macro}}(\vec{r})$ inside a voxel of a GESSE measurement. In these high resolution images the signal loss due to macroscopic inhomogeneities can be neglected. After B_{macro} had been calculated by using linear regression to the phase values over time for each voxel of the MMGE images, the gradients in all three directions were calculated. For the gradient maps in each direction, the two adjacent voxels in the respective direction were considered. Equation 3.36 was used to calculate the resulting total correction function. It can be seen that the largest inhomogeneity effect can be seen in slice selection direction. One reason for this is that this dimension is typically larger than the in-plane resolution and, therefore, the argument in the correction function (Eq. 3.34) is a higher value. Acquired phase images often consist of several phase jumps (called *wraps*) caused by the fact, that there are only phase values between $-\pi$ and π . These phase jumps can be removed by an algorithm developed by Herráez et al. [2002]. The unwrapped data can then be used to calculate the time-dependent correction function and to correct the GESSE data.

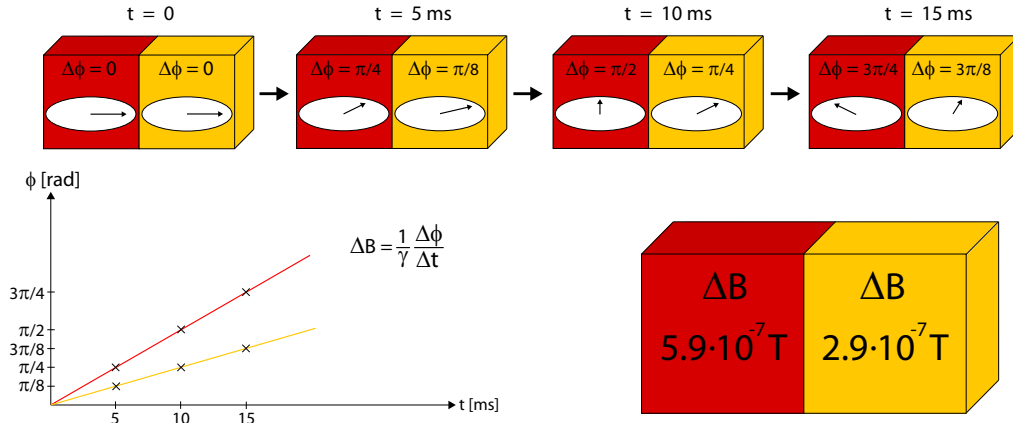


Figure 3.8 Calculation of ΔB . **Top:** Acquisition of high resolution phase maps at different echo times. Here, two adjacent voxels under the influence of different B_{macro} values are sketched. **Bottom:** The slope of the phase-time-curve yields $\Delta\omega$, the deviation from the Larmor frequency. Dividing by γ yields the ΔB value of the respective voxel.

3.4 Measurement of Tissue Oxygenation: Analytical Methods

This section consists of three different analytical methods of oxygenation calculation. All methods are based on the same tissue model: The susceptibility difference between deoxygenated blood and surrounding tissue cause a certain magnetic field distribution in the voxel resulting in oxygenation-dependent signal relaxation. Knowledge about this distribution and the magnetic properties of blood enables the calculation of the oxygenation saturation of the venous blood. Moreover, another technique for tissue oxygenation calculation is presented here. This technique allows the separation of the signal originating from the venous part of the blood circuit from the rest of the signal. The T_2 calculation and the usage of a calibration curve enables OEF determination of the tissue. At the end of this section, susceptibility weighted imaging (SWI) measurements of the kidney are presented. The contrast in these images are also a marker for oxygenation of the blood.

3.4.1 Three-Parameter Fit (TPF) Approach

The method of tissue oxygen quantification is based on the signal equation (Eq. 3.21). The important information is implied in the frequency shift $\delta\bar{\omega}$, that can be found in the argument of the characteristic function $f_c(\delta\bar{\omega} \cdot t)$ in the signal equation. Therefore the analytical expressions for the asymptotic forms of this characteristic function has to be used. The combination of Eq. 3.23 and Eq. 3.25 yields the important expression for the reversible relaxation rate,

$$R'_2 = \lambda \cdot \delta\bar{\omega} = \lambda \cdot \frac{4\pi}{3} \cdot \gamma \cdot \Delta\chi \cdot B_0. \quad (3.38)$$

Equation 3.38 shows the linear relationship between the deoxyhemoglobin-induced frequency shift and the reversible relaxation rate. Since the frequency shift is a function of the mean susceptibility difference in the voxel, the relaxation rate R'_2 can be written as

a function of λ and $\Delta\chi$. It can be concluded from Eq. 3.38 that $\Delta\chi$ can be calculated, if λ and the R'_2 are known. With this information the oxygenation Y can be calculated (Eq. 2.94). While the GESSE sequence (section 3.2.2.1) samples data around a spin echo, R'_2 and λ can be calculated from this data by measuring the long-term asymptotic forms. In this case the argument of Eq. 3.25 changes from t to $t - TE$ and the signal equation for the long-term asymptotic form turns into

$$S(t - TE) = (1 - \lambda) \cdot S_t(0) \cdot e^\lambda \cdot e^{-R'_2 \cdot |t - TE|} \cdot e^{-R_2 \cdot (t - TE)}. \quad (3.39)$$

Equation 3.39 is the fundamental signal equation, which is used for parameter determination by fitting of the acquired MR data. Furthermore, this equation shows that the signal amplitude at the time of a spin echo TE_{SE} is absolutely unaffected by magnetic inhomogeneities, while those inhomogeneities are characteristic for the signal decay in the vicinity of a spin echo (Fig. 3.9). It can be seen that the irreversible relaxation rate R_2 and the reversible relaxation rate R'_2 counteract each other before the spin echo. After the spin echo both relaxation rates are adding up. This results in the following relaxation rates before and after the spin echo, respectively,

$$R_{2,b} = R_2 - R'_2, \quad (3.40)$$

$$R_{2,a} = R_2 + R'_2. \quad (3.41)$$

Since both, $R_{2,b}$ and $R_{2,a}$, are measured, the relaxation rates R_2 and R'_2 can be calculated. The investigation of the signal at $t = TE$ yields information about the volume fraction λ of the deoxygenated blood,

$$\lambda = \ln \left(\frac{S_{\text{extra}}(TE_{SE})}{S(TE_{SE})} \right). \quad (3.42)$$

According to Eq. 3.39, where λ , R'_2 and R_2 are the parameters that can be determined by fitting the acquired MR data, this method is called *TPF-method* (three-parameter fit method). When the three parameters R_2 , R'_2 and λ are determined by the TPF-method, the two latter can be used to calculate the oxygenation (Eq. 2.94 and Eq. 3.38),

$$Y = 1 - \frac{3}{4\pi\gamma B_0} \cdot \frac{R'_2}{\lambda} \cdot \frac{1}{\Delta\chi_{\text{do}} \cdot \text{Hct}}. \quad (3.43)$$

Bongers [2004] compared two different methods for oxygenation determination. One method was based on independently fitting of the asymptotes before and after the spin echo, the other method used the combined function (Eq. 3.39). It was shown that the independent method yields unstable parameter estimation. With the combined method, that is used in this work, the true extrapolation is avoided and the parameter error is reduced by 30-50% compared to the independent method, assuming the same SNR.

3.4.2 Semi-Quantitative (SQ) Approach

Although the TPF-method yields promising results, the parameter error is still non-negligible. The main problem is the uncertainty when fitting three parameters at the same time. The idea was to develop a method where the three parameter fit of the TPF-method turns into a two parameter fit. Therefore, a method developed in this work is based on an independent λ determination. It has to be mentioned that in the equations

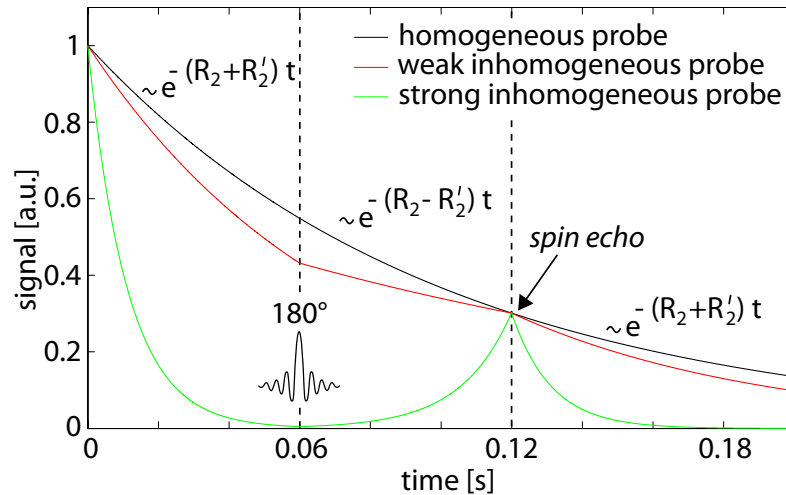


Figure 3.9 Signal around a spin echo. This simulation shows probes of different inhomogeneity. While the signal decay of a homogeneous probe (black line, $R_2' = 0$) is not affected by a spin echo, the reversible relaxation rate changes the signal decay of a weak inhomogeneous probe (red line, $R_2' = 4$ Hz) and a strong inhomogeneous probe (green line, $R_2' = 80$ Hz). In this simulation, the irreversible relaxation rate $R_2 = 10$ Hz was assumed.

and calculations, λ is not the whole blood volume, but that part of the blood volume that is responsible for susceptibility differences between blood and tissue. λ is the blood volume of the venous (deoxygenated) part, because the susceptibility difference between arterial (oxygenated) blood and surrounding tissue is negligible.

In this method, the value for the whole blood volume determined in a dynamic susceptibility contrast (DSC) perfusion measurement is used, because there does not exist a reliable method that can be used to determine the venous blood volume. Therefore this method is called *semi-quantitative method* (SQ-method).

3.4.2.1 Determination of the CBV Using a DSC-Perfusion Measurement

In general, contrast in MRI arises mainly from the heterogeneous distribution of proton density and/or relaxation times. Therefore, the lack of need for contrast materials in most applications is one of the main advantages of MRI over x-ray techniques. Nevertheless, there exist areas, where the usage of external contrast agents is essential. This is the case for areas with different tissue vascularity and perfusion. These areas do not show a difference in contrast on MRI images without contrast agents. In most DSC-MRI studies paramagnetic gadolinium-based contrast agents are used. The magnetic susceptibility of the tracer is proportional to its concentration. The high concentrated contrast agent is injected rapidly, creating a so-called *bolus*. The paramagnetic tracer alter the susceptibility of the tissue bulk in a measurable way by changing the contrast in MR images [Rosen et al., 1990]. The local susceptibility difference causes a local magnetic field disturbance, that causes a frequency shift of the present water molecules (Fig. 3.10). This results in a shorter T_2^* relaxation time, measurable with a T_2^* -weighted sequence. The assumption of monoexponential relaxation leads to the following signal intensity of a T_2^* -weighted

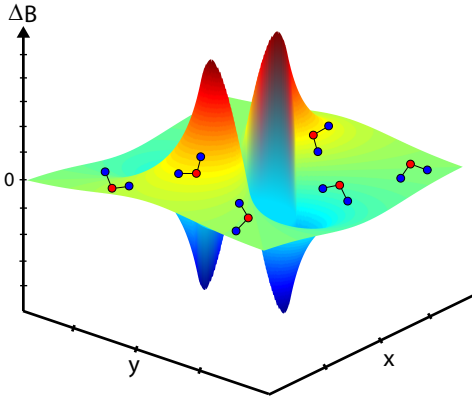


Figure 3.10 The effect of paramagnetic contrast agent on MR signal. The sketch shows the magnetic field offset around a paramagnetic vessel with an angle $\theta \neq 0$ to the magnetic field. The protons in the water molecules that give a contribute to the MR signal underlie different magnetic field offsets resulting in different precession frequencies of the magnetic moments. This leads to intra-voxel spin dephasing resulting in signal loss in T_2^* -weighted images.

sequence,

$$S = S_0(\rho, T_1, TR) \cdot e^{-R_2^* \cdot TE}, \quad (3.44)$$

where $S_0(\rho, T_1, TR)$ is a term that depends only on the proton density ρ , the longitudinal relaxation time T_1 and the repetition time TR . The contrast agent causes an increase of the relaxation rate R_2^* , proportional to the concentration of the contrast agent in the blood C_a ,

$$R_2^* = R_{2,0}^* + r_2^* \cdot C_a, \quad (3.45)$$

where $R_{2,0}^*$ is the intrinsic gradient echo relaxation rate without contrast agent and r_2^* is the transverse relaxivity, dependent on the blood volume and the vascular morphology [Boxerman et al., 1995, Kiselev, 2001]. If $S(0)$ and $S(t)$ are the signal intensities in the baseline state and at a time t after the bolus injection, respectively, and $R_2^*(0)$ and $R_2^*(t)$ are the corresponding relaxation rates, the tissue concentration $C_t(t)$ can be calculated with Eq. 3.44 and Eq. 3.45,

$$\begin{aligned} C_t(t) &= \frac{R_2^*(t) - R_2^*(0)}{r_2^*} = \frac{\Delta R_2^*(t)}{r_2^*} \\ &= \frac{1}{r_2^* \cdot TE} \cdot \ln \left(\frac{S(t)}{S(0)} \right). \end{aligned} \quad (3.46)$$

This tracer method can be used for the determination of the vascular distribution of the signal. The regional cerebral blood volume (CBV) can be quantized by determination of an arterial input function (AIF), that denotes the concentration of contrast agent within the arterial supply to the tissue. Figure 3.11 schematically shows the variation of time of the AIF $C_a(t)$, the tissue concentration $C_t(t)$ and the MR signal $S(t)$. Integration over the concentration-time-curve and normalizing the data to the AIF enables CBV quantification,

$$\text{CBV} = \frac{H_f \int_0^\infty C_t(t) dt}{\rho \int_0^\infty C_a(t) dt}, \quad (3.47)$$

where

$$H_f = \frac{1 - \text{Hct}_{\text{art}}}{1 - \text{Hct}_{\text{cap}}} \quad (3.48)$$

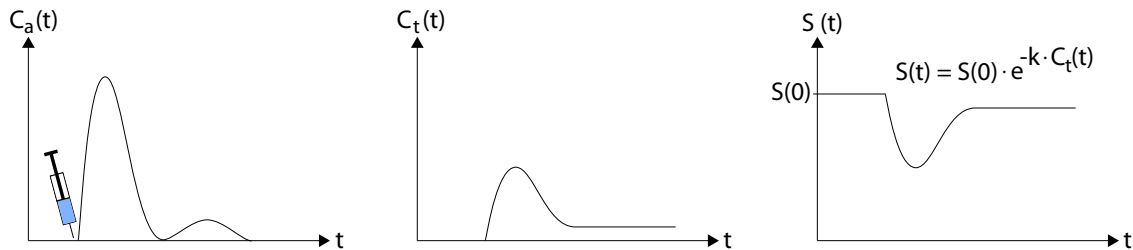


Figure 3.11 Dynamic susceptibility contrast. After the paramagnetic tracer is injected into the blood supply, it enters the brain microcirculation and disperses. **Left:** The AIF shows a rapid increase of tracer concentration due to bolus injection. After the concentration in the blood has decreased to zero, it regrows a little and then falls back to zero. This regrowing happens due to recirculation of the contrast agent. **Middle:** The contrast agent concentration in the microcirculation starts to increase after bolus injection. After the maximum concentration in the blood is reached, it falls back to a nearly constant value, because the contrast agent stays in the microvasculature until it is washed out by the kidneys. This procedure can last several hours. **Right:** The MR signal decreases during the circulation (*first pass*) and does not return to the baseline level for a long time due to the mentioned recirculation of the tracer.

is a factor that accounts for the difference in arterial hematocrit Hct_{art} and capillary hematocrit Hct_{cap} , and ρ is the density of brain tissue [Tofts, 2003]. These CBV values, in this section denoted as λ , were used for further data postprocessing.

3.4.2.2 Combination of DSC with GESSE Measurement

The results of a DSC measurement, i.e. the λ -values, were used as an input parameter for further data postprocessing. This results in a two parameter fit for the signal equation. The fit of the missing parameters, R_2 and R'_2 , is then more stable due to less fitting parameters. The oxygenation calculation is performed using Eq. 3.43. The advantages and disadvantages of the SQ-method compared to the TPF-method are discussed in chapter 5.

3.4.3 Three-Sequence-Combination (TSC) Approach

In this work, another method was developed to determine the OEF. The model is the same as for the TPF- and the SQ-method, but the measurement differs. Here, three measurements were performed to determine the three parameters of the signal equation (Eq. 3.39) independently. This method is called *TSC-method* (three-sequences-combination). For R_2 determination a CPMG sequence was used (c.f. section 3.2.2.3). This T_2 -weighted imaging sequence acquires several echoes at different echo times and can be used for R_2 fitting. For R'_2 determination the MMGE sequence (c.f. section 3.2.2.2) was used, which allows the determination of R_2^* by multi-echo acquisition. By subtracting the calculated R_2 value from the calculated R_2^* value, the R'_2 value could be calculated pixel-wise. These two parameters, R_2 and R'_2 , were used as input parameters for the GESSE sequence. The schematic process of the TSC-method can be seen in Fig. 3.12. As can be seen in the signal equation (Eq. 3.39), the number of free parameters reduces to one resulting in a very stable fit. By separate determination of the relaxation times, the slopes of the curves

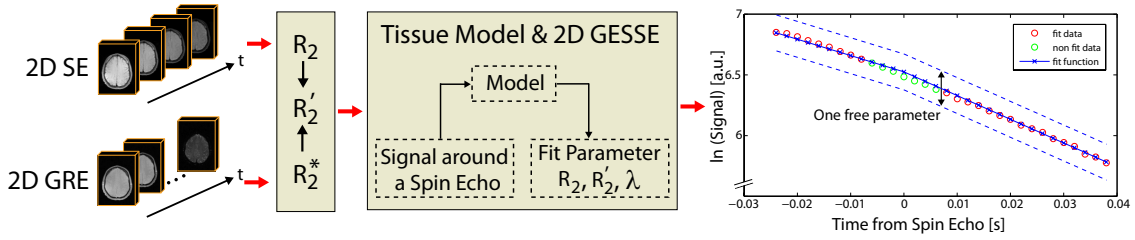


Figure 3.12 Experimental setup of the TSC-method. First, echo trains of a spin echo sequence and a gradient echo sequence were acquired to calculate a R_2 map and a R_2^* map of the investigated slice. After R_2' calculation, R_2 and R_2' were used as an input parameters for the GESSE data postprocessing resulting in only one left fit parameter, λ .

of the GESSE measurement before and after the spin echo are defined. Therefore the parameter fit determines the value of the oxygenated blood volume λ by shifting the fit curve in vertical direction.

3.5 Measurement of Tissue Oxygenation: Venous Blood Isolation Method

This section uses an approach for oxygenation determination that has first been published by Bolar et al. [2009] and is called *QUantitative Imaging of EXtraction of Oxygen and TIssue Consumption* (QUIXOTIC). This OEF determination method consists of three steps: The isolation of the signal originating from venous blood, the measurement of the relaxation time T_2 of the venous blood, and the calibration with a T_2 - Y -calibration curve.

3.5.1 Isolation of Venous Blood Signal

The QUIXOTIC method is based on a velocity-selective spin labeling (VSSL) technique [Wong et al., 2006]. Hereby, so-called *velocity-selective modules* (VSMs) are used to sustain the signal from spins flowing below a critical velocity v_c .

3.5.1.1 Velocity Encoding

In the following, one-dimensional stationary flow of the spins is assumed. Considering a spin flowing in x -direction with the velocity v_x under the influence of a bipolar gradient with amplitude G_x , the spin accumulates a phase,

$$\begin{aligned} \Delta\varphi &= \Delta\omega \cdot t \\ &= \gamma \cdot G_x \cdot \delta \cdot (x_1 - x_2), \end{aligned} \quad (3.49)$$

where x_1 and x_2 are starting and end point, respectively. Assuming a spin with the velocity $v_x = 0$ ($x_1 = x_2$, Fig. 3.13a) the accumulated phase is $\Delta\varphi = 0$ (Eq. 3.49). If the velocity becomes larger than zero (Fig. 3.13b), the spin accumulates a phase. The distance between x_1 and x_2 depends then on the time from the middle of the first gradient to the middle of the second gradient, Δ . For the case without a time delay between the gradients, Δ equals to δ , the duration of one gradient. For a constant velocity $v_x > 0$,

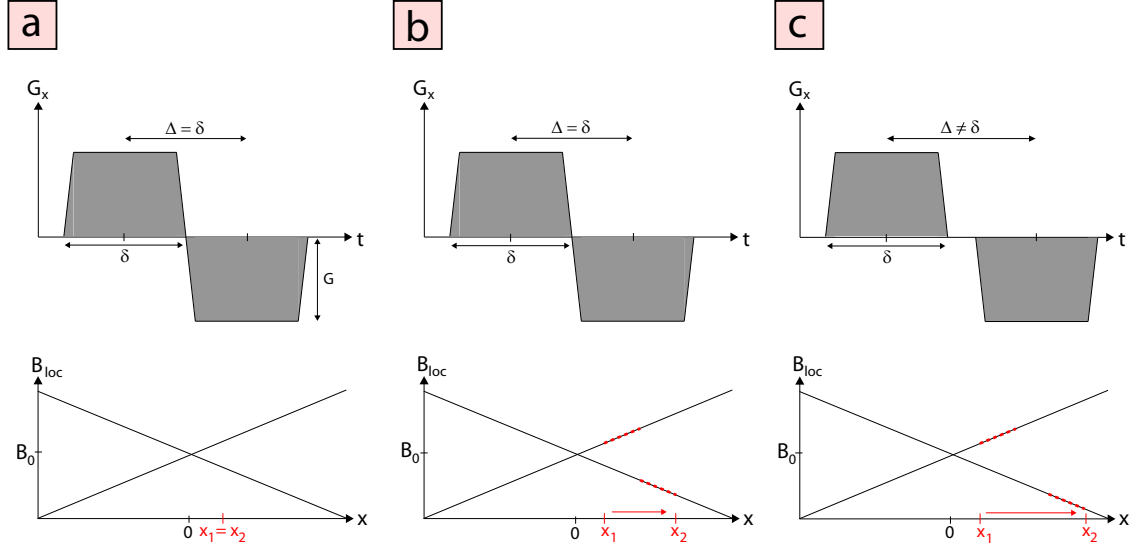


Figure 3.13 Velocity encoding in one dimension. Under the influence of a bipolar gradient, a spin accumulates a phase, that is proportional to its velocity v_x , the gradient strength G_x , the duration from the middle of one gradient to the middle of the other gradient Δ and the duration of one gradient δ . The image shows the cases for **a)** $v_x = 0$, **b)** $v_x > 0$ and adjacent bipolar gradients and **c)** $v_x > 0$ with a time interval between the bipolar gradients.

the accumulated phase becomes

$$\Delta\varphi = \gamma \cdot G_x \cdot v_x \cdot \delta^2. \quad (3.50)$$

If the distance between the gradients becomes larger than zero (Fig. 3.13c), the accumulated phase $\Delta\varphi$ depends additionally on Δ ,

$$\Delta\varphi = \gamma \cdot G_x \cdot v_x \cdot \delta \cdot \Delta. \quad (3.51)$$

3.5.1.2 Capillary Model

For the following calculation, the tissue model of Ahn et al. [1987] was used. For this model, several preconditions were made [Keele et al., 1982, Folkow and Neil, 1971]: Assuming a mean capillary diameter of about 3 mm with an average length of about 750 μm with a flow velocity of about 300 – 500 $\mu\text{m/s}$ inside the capillaries. With a readout time of $t_{\text{read}} = 100 \text{ ms}$, which is a typical duration for the readout in MRI, the distance passed by the flowing spins can be calculated to 30 – 50 μm . The comparison of the capillary length with this distance allows the assumption that the flow inside the segmented capillaries is constant and linear, even if the direction of the flow may differ from capillary to capillary. The assumption of a capillary density of 400 – 500 mm^3 and a typical voxel size of $1 \times 1 \times 7 \text{ mm}^3$ yields about 3000 segmented capillaries in one voxel. This fact justifies a statistical approach resulting in the assumption of statistically distributed and randomly orientated cylinders in all directions. Figure 3.14a shows the transition from the *in vivo* capillary network to the capillary flow model.

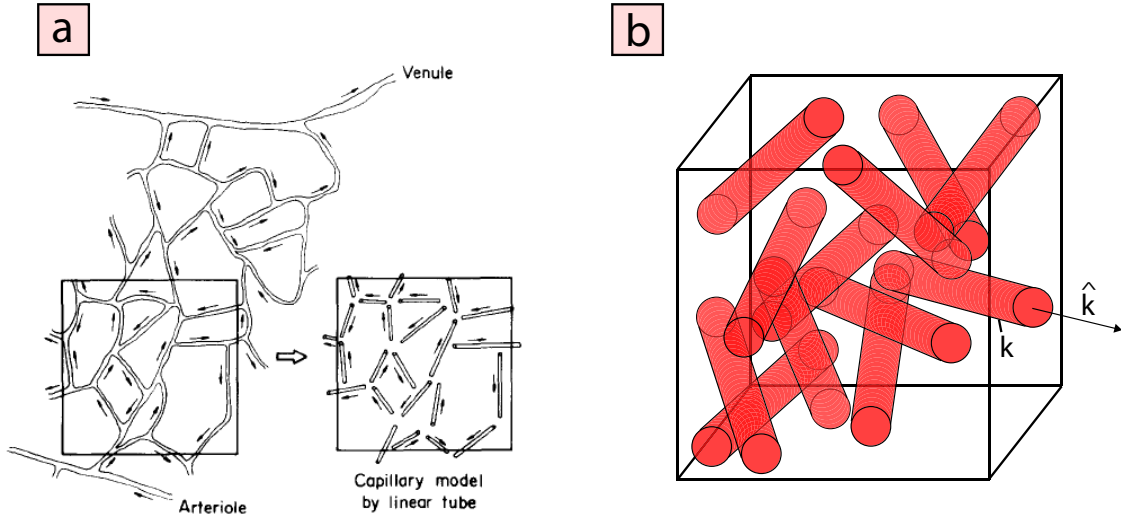


Figure 3.14 Capillary Modeling. a) Statistically distributed and randomly orientated tubes are used to model the capillary flow. Figure adopted from Ahn et al. [1987]. b) Sketch of the tube distribution inside a voxel.

3.5.1.3 Statistical Analysis for the Capillary Model

According to the preconditions described in section 3.5.1.2, the signal originating from a tube network under the influence of velocity encoding gradients is described below [Ahn et al., 1987]. Denoting a tube within a voxel as k (Fig. 3.14b) and the corresponding orientation with the unit vector \hat{k} , the signal originating from the tube with a velocity density function $f_k(v)$ for all velocity components can be expressed as

$$m_k = m_{0k} \int_0^{\infty} f_k(v) \cdot e^{i \cdot \Delta \phi} dv. \quad (3.52)$$

Inserting Eq. 3.51 yields

$$m_k = m_{0k} \int_0^{\infty} f_k(v) \cdot e^{iv_x \cdot \gamma G_x \delta \Delta \hat{k}} dv, \quad (3.53)$$

where m_{0k} is the spin intensity in the tube at $v = 0$. Substituting

$$\vec{\alpha} = \gamma \cdot \vec{G} \cdot \delta \cdot \Delta \quad (3.54)$$

yields the three-dimensional signal equation,

$$m_k = m_{0k} \int_0^{\infty} f_k(v) \cdot e^{iv \cdot \vec{\alpha} \cdot \hat{k}} dv, \quad (3.55)$$

The signal from a whole voxel can be calculated by a summation over all m_k in Eq. 3.53,

$$\begin{aligned} M &= \sum_k m_{0k} \int_0^\infty f_k(v) \cdot e^{iv \cdot \vec{\alpha} \cdot \hat{k}} dv \\ &= \sum_k m_{0k} \int_0^\infty f_k(v) \cdot e^{iv|\alpha| \cos \theta_k} dv, \end{aligned} \quad (3.56)$$

where θ_k is the angle between $\vec{\alpha}$ and \hat{k} . As a next step, it is assumed that the velocity density function is equal for all tubes ($f_k(v) = f(v)$), which turns Eq. 3.56 into

$$M = M_0 \int f(\theta) \left[\int_0^\infty f(v) \cdot e^{iv|\alpha| \cos \theta} dv \right] d\theta. \quad (3.57)$$

M_0 is the sum of equilibrium spin intensity for the stationary ($v = 0$) state, and $f(\theta)$ is the orientational density function, which can be expressed as

$$f(\theta) = \begin{cases} \frac{\sin \theta}{2} & \text{for } 0 \leq \theta \leq \pi, \\ 0 & \text{for otherwise.} \end{cases} \quad (3.58)$$

θ is the polar angle in a spherical coordinate system, where the direction of the vector $\vec{\alpha}$ coincides with the z -direction. With the combination of Eqs. 3.57 and 3.58, the signal equation can be expressed as

$$\begin{aligned} M &= \frac{M_0}{2} \int_0^\infty f(v) \left[\int_0^\pi \sin(\theta) \cdot e^{iv|\alpha| \cos \theta} d\theta \right] dv \\ &= M_0 \int_0^\infty f(v) \text{sinc}(|\vec{\alpha}|v) dv \end{aligned} \quad (3.59)$$

3.5.1.4 Different Flow Types

According to Eq. 3.59, a certain velocity density function $f(\theta)$ has to be assumed for further calculations. Therefore, the model of two most common kind of flow types are presented here: Plug flow and laminar flow (Fig. 3.15). In the case of plug flow, there is only one velocity $v = v_0$ present, which turns the velocity density function into

$$f(v) = \delta(v - v_0), \quad (3.60)$$

and the signal can be calculated according to Eq. 3.59,

$$\begin{aligned} M &= M_0 \int_0^\infty \delta(v - v_0) \text{sinc}(|\vec{\alpha}|v) dv \\ &= M_0 \text{sinc}(|\vec{\alpha}|v_0). \end{aligned} \quad (3.61)$$

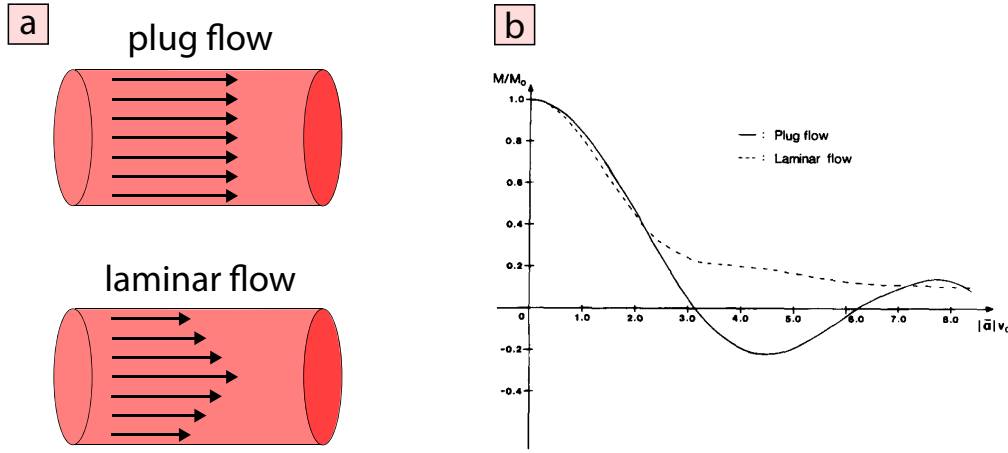


Figure 3.15 Different flow types: Plug flow and laminar flow. **Left:** While in the case of plug flow the flow velocity is independent from the position, for laminar flow the profile shows a higher flow velocity in the middle of the capillary than at the boundary. **Right:** Plot of the signal for random directionally directed flow inside the capillaries with different flow types after application of the VSM. Figure adopted from Ahn et al. [1987].

Laminar flow with a maximum velocity v_{\max} and a mean velocity $v_0 = v_{\max}/2$ can be described with the following velocity density function,

$$f(v) = \begin{cases} 1/(2v_0) & \text{for } 0 \leq v \leq 2v_0, \\ 0 & \text{for otherwise.} \end{cases} \quad (3.62)$$

This results in the signal equation for laminar flow,

$$\begin{aligned} M &= \frac{M_0}{2} \int_0^{2v_0} \text{sinc}(|\vec{\alpha}|v) dv \\ &= M_0 \text{Si}(2|\vec{\alpha}|v_0)/(2|\vec{\alpha}|v_0), \end{aligned} \quad (3.63)$$

where Si is the sine integral,

$$\text{Si}(x) = \int_0^x \text{sinc}(x') dx'. \quad (3.64)$$

Fig. 3.15 shows the plot of random directionally distributed flow as a function of $|\vec{\alpha}|v_0$. The superposition of laminar and plug flow allows the simplification that the signal M/M_0 passes zero at

$$|\vec{\alpha}|v_c = \pi, \quad (3.65)$$

and then remains near zero [Duhamel et al., 2003], where v_c is called *critical velocity*. This model shows that spins with a velocity below the critical velocity give a contribution to the signal, while spins with a velocity larger than the critical velocity do not. This fact is used in the QUIXOTIC approach. It has to be mentioned that Eq. 3.65 shows the possibility to vary v_c by variation of $|\vec{\alpha}|$, for instance by increasing or decreasing the velocity encoding gradient amplitudes (Eq. 3.54).

3.5.1.5 Development of the Velocity-Selective Module (VSM)

This velocity-selective cut off is called *velocity-selective module* (VSM). The simplest module presented by Ahn et al. [1987] consists of two bipolar gradients. He and Guilfoyle et al. [1991] further developed a model consisting of these two gradients with a 180° pulse in between, to remove macroscopic field offset effects. Duhamel et al. [2003] developed a technique where he subtracted an image acquired with prior VSM from an image without VSM and called this technique *velocity-selective arterial spin labeling* (VSASL). A fundamental work on this field was published by Wong et al. [2006] where he modified the VSM by adding an additional pair of bipolar gradients and another 180° pulse to reduce the effects of eddy currents. The 180° refocusing pulses were applied as adiabatic pulses to avoid B_1 inhomogeneities. In practice, at first a 90° hard pulse is applied to flip the magnetization into the transverse plane. Afterwards, the gradient/pulse-combination explained above is applied. Now, there are only spins with a velocity below v_c in the transverse plane. Applying another 90° hard pulse (with a 180° phase shift compared to the first one), causes a back flipping of this magnetization into the longitudinal direction and a flipping of the spins with a velocity larger than v_c into the transverse plane. The pulse scheme of the VSM can be seen in Fig. 3.16. After the application of a VSM, a spoiler gradient is applied to destroy residual transverse magnetization resulting from spins flowing faster than v_c .

3.5.1.6 Velocity-Selective Spin Labeling (VSSL)

The properties of a VSM can now be used to get the MR signal from spins that flow below a certain velocity. The aim of this part of the work is to get a signal from spins of the venous part of the vascular tree to investigate the oxygen content. This can be realized by the following VSSL-based technique [Bolar et al., 2009]. Considering a vascular tree, the flow velocity profile inside the tree can be simplified. The flow velocity is higher in the big arteries and veins than in the capillary bed, due to the higher vessel diameter. A simplification of the velocity profile is presented in Fig. 3.17. Assuming an imaging sequence that starts with a VSM with an adjusted v_c value, this value is chosen to select

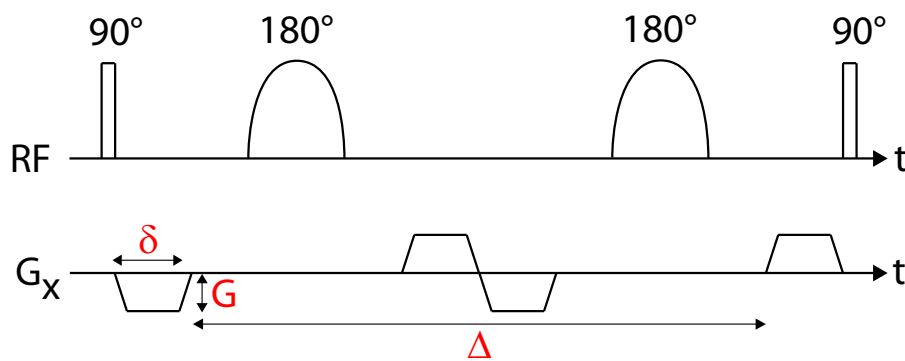


Figure 3.16 Velocity-selective module (VSM). The module consists of a combination of 90° hard pulses and adiabatic 180° pulses. The important property of adiabatic pulses is their B_1 -inhomogeneity resistance. Each of them is placed between a pair of bipolar gradients in the respective encoding direction. This example shows velocity encoding in x -direction.

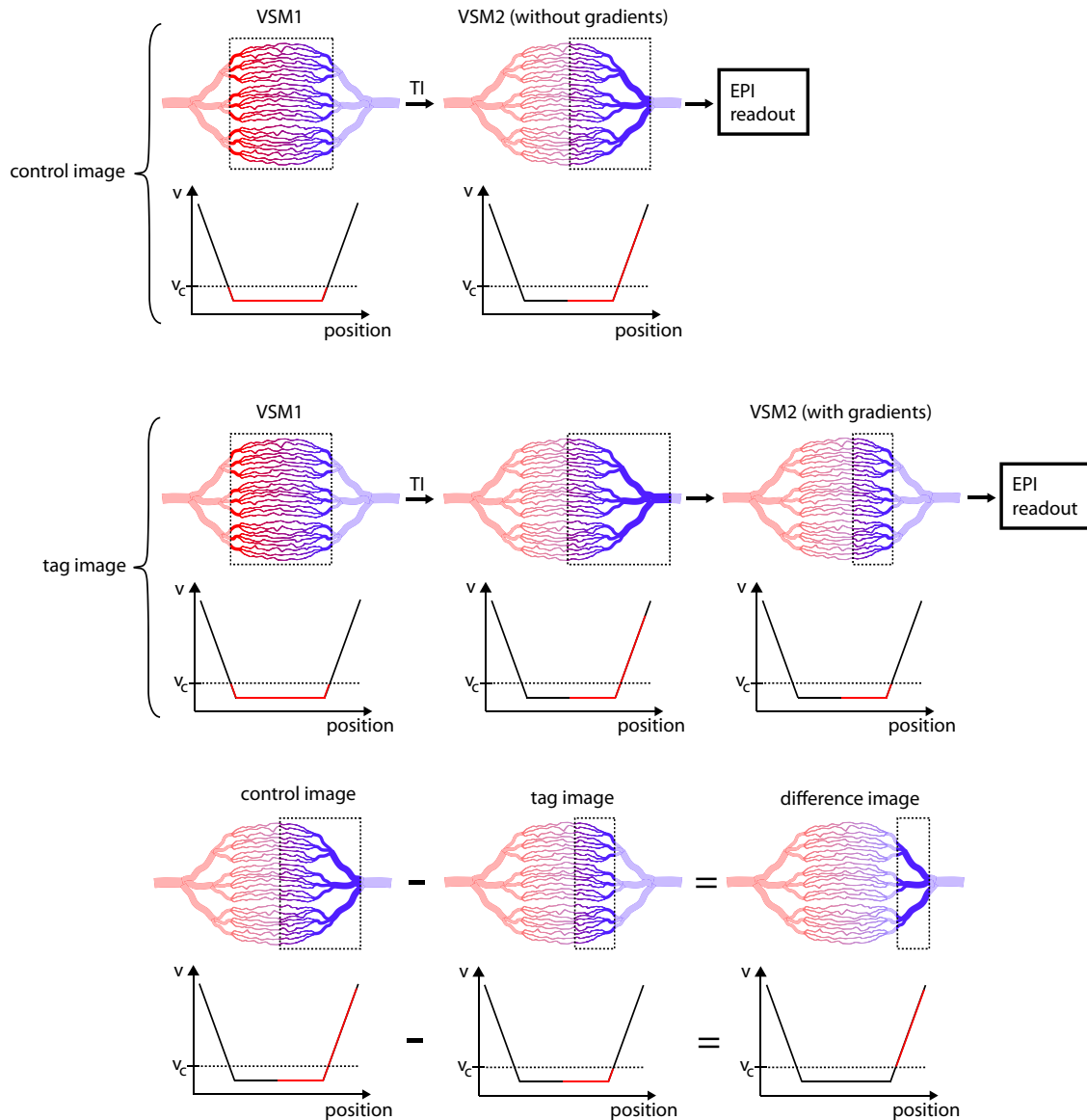


Figure 3.17 Velocity-selective spin labeling (VSSL). **Top:** The imaging sequence for the control image consists of the VSM1, a delay time TI and the VSM2 without gradients. On the acquired image signal from spins that are either stationary or located between the capillary bed and the venous part of the vascular tree. **Middle:** The tag image sequence is the same as the control image sequence except from the now applied gradients in the VSM2. This results in the tagging of spins that are either stationary or still in the capillary bed. **Bottom:** The subtraction of the tag image from the control image leads to a remaining signal originating only from spins out of the venous part of the blood circuit.

only the blood below v_c ¹. If now an EPI would be started, there would only be a signal originating from spins flowing slower than v_c (e.g. spins in the capillary bed and stationary

¹*select* means that after the application of the VSM, only spins with a velocity larger than v_c are in the transverse plane

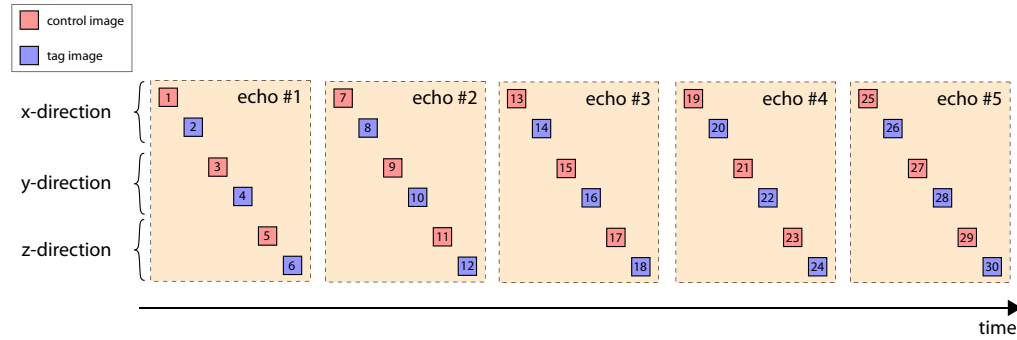


Figure 3.18 Acquisition order of the VSSL measurement. Control images and tag images are acquired alternately in x -, y - and z -direction. After the six images of the first echo are acquired, the recording of the second echo starts. This procedure continues until all echoes are acquired.

spins). After the application of the VSM, an EPI is executed after a duration of time, called *inflow time* TI , while the labeled blood flows into the venous part of the vascular tree. After the time TI a second VSM, called *VSM2*, is applied without the gradients. In contrast to the VSM1, the second module VSM2 does not cut off the signal originating from spins with $v > v_c$, but causes a T_2 -weighting due to the 180° pulses. Subsequently, the EPI starts, acquiring a T_2 -weighted image of the stationary tissue and the blood that is located somewhere between the capillary bed and the large veins, depending on the duration TI . The acquired image is called *control image*. As a next step, after TR , again VSM1 is applied. After waiting the time TI , the VSM2, that is now the same as VSM1, is applied. The second module again cuts off the signal from spins flowing faster than v_c . In our example, only the stationary spins and the spins that are still in the capillary bed after TI are in the transverse plane before readout. The following EPI acquires the so-called *tag image*. As a last step, the tag image is being subtracted from the control image to receive a difference image which contains only signal from spins of the venous part of the vascular tree. A schematic illustration of the capillary network and the velocity profile during the control image and tag image acquisition as well as the subtraction of both can be seen in Fig. 3.17. Figure 3.18 illustrates the order of the acquired images. After a control image, always the corresponding tag image was acquired. First the control and tag images for all three dimension for the first echo was acquired. Afterwards, the same was done with the second echo. This procedure was continued until echo number 5. With a number of 6 images (control image and tag image, three dimensions) this results in a total number of 30 acquisition per measurement.

3.5.1.7 Sequence Design: Consideration of T_1 Relaxation

After the application of VSM1 all spins above the velocity v_c are saturated in the control image as well as in the tag image. During the following inflow time the spins experience a non-negligible T_1 relaxation. While VSM2 again saturates all spins above v_c in the tag image, there is a longitudinal component of spins above this velocity in the control image due to T_1 relaxation. Subtraction of control and tag image leads to signal from the desired venous component that is contaminated by the spins of the unwanted compartments. To

solve this problem, a global inversion pulse is placed between VSM1 and VSM2. This results in a nulling of the recovering blood signal. Hereby, the correct time for the inversion pulse has to be calculated. After the time t_{pre} , the non-selective inversion pulse is applied resulting in an inversion of all spins. During t_{post} the magnetization vector of the initially saturated spins (with $v > v_{\text{cut}}$) will grow to zero. To calculate the times t_{pre} and t_{post} for a desired TI , the signal equations for saturation recovery and inversion recovery have to be used. After application of VSM1 the saturated spins recover resulting in a longitudinal magnetization

$$M_{z,\text{fast}} = M_{0,\text{fast}} \left(1 - e^{-t_{\text{pre}}/T_1}\right), \quad (3.66)$$

where $M_{0,\text{fast}}$ is the equilibrium value of the magnetization of the spins with $v > v_{\text{cut}}$ in z -direction and T_1 is the longitudinal relaxation time of the investigated tissue. Introducing the variable M_{rat} as the ratio of M_z and M_0 , t_{pre} can be expressed as

$$t_{\text{pre}} = -T_1 \cdot \ln(1 - M_{\text{rat}}). \quad (3.67)$$

After the time t_{pre} the inversion pulse is applied and M_{rat} turns into $-M_{\text{rat}}$. To calculate the time t_{post} , a theoretical inversion pulse after the VSM1 module has to be considered. The theoretical development of the longitudinal magnetization can be expressed as

$$M_{z,\text{fast}} = M_{0,\text{fast}} \left(1 - 2e^{-t_{\text{theo}}/T_1}\right), \quad (3.68)$$

or, with the same notation as in Eq. 3.67,

$$t_{\text{theo}} = -T_1 \cdot \ln\left(\frac{1 + M_{\text{rat}}}{2}\right). \quad (3.69)$$

For this theoretical consideration, there is a zero-crossing of the signal for

$$t_{\text{null}} = -T_1 \cdot \ln(0.5). \quad (3.70)$$

Since the time t_{null} is the sum of t_{theo} and t_{post} , the time between the inversion pulse and VSM2 can be calculated as

$$\begin{aligned} t_{\text{post}} &= -T_1 \cdot \ln(0.5) + T_1 \cdot \ln\left(\frac{1 + M_{\text{rat}}}{2}\right) \\ &= T_1 \cdot \ln(1 + M_{\text{rat}}). \end{aligned} \quad (3.71)$$

3.5.1.8 Sequence Design: TI -Variation

By determining a certain TI value and with the knowledge about the T_1 relaxation time of the investigated material, a calculation of M_{rat} is possible. The longitudinal relaxation time depends on different factors, i.e. temperature T , hematocrit Hct and oxygenation Y . Lu et al. [2004] showed a linear T -dependency and a linear Hct-dependency of T_1 in blood. Moreover, T_1 slightly increases with blood oxygenation. For a typical human Hct of 0.42 and a human body temperature of 36.75°C the T_1 relaxation times are 1644 ± 14 ms and 1584 ± 5 ms for arterial and venous blood, respectively. Therefore an assumed T_1 value of 1600 ms for blood is well justified. With this information and the relationship

$$TI = t_{\text{pre}} + t_{\text{post}} = T_1 \cdot \ln\left(\frac{1 + M_{\text{rat}}}{1 - M_{\text{rat}}}\right) \quad (3.72)$$

the times t_{pre} and t_{post} can be calculated (Eqs. 3.67 and 3.71). Figure 3.19 shows the dependency of the parameter t_{pre} , t_{post} and M_{rat} on the inflow time TI .

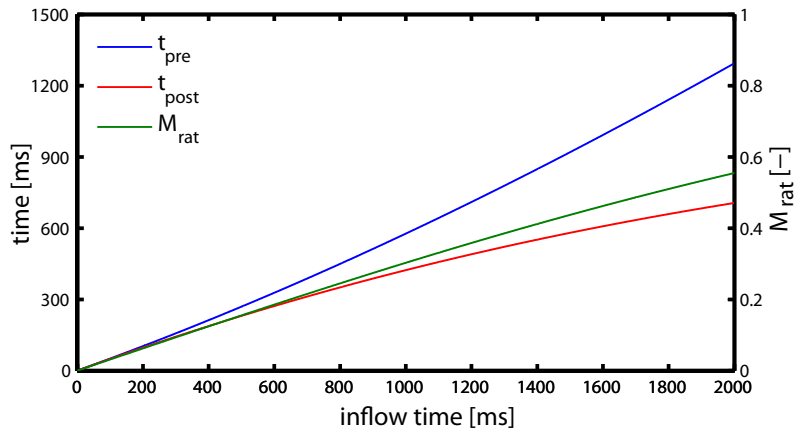


Figure 3.19 Important sequence parameters. Pre-inversion-pulse time t_{pre} and post-inversion-pulse time t_{post} after VSM1 are illustrated on the left axis. The right axis shows the ratio of the longitudinal magnetization of the initially saturated spins and the equilibrium longitudinal magnetization of them. For this simulation, a T_1 of 1600 ms was assumed.

3.5.1.9 Sequence Design: Variation of v_{cut}

The venous bolus is defined on two edges: On the leading edge it is limited by the inflow time, while on the trailing edge v_{cut} is the limiting factor. To have a variable sequence, the inflow time can be changed simply by increasing or decreasing the time delay between VSM1 and VSM2. The corresponding times t_{pre} and t_{post} are changed accordingly (Eq. 3.72). According to Eq. 3.54, a variation of v_c is realizable by the variation of the gradient amplitudes of VSM1 and VSM2.

3.5.2 Echo Time Variation

The aim of this section is to determine the relaxation time T_2 of the signal originating from the blood in the veins. This can be achieved by the modification of the VSM2 from section 3.5.1.6. To acquire a T_2 -weighted signal at different echo times, the VSM2 can be expanded by pairs of adiabatic 180° pulses. The time between the acquired echoes is determined by the length of the VSM2. Figure 3.20 illustrates the modification of the imaging sequence. Each added pair of refocusing pulses enables signal acquisition at a later echo time. In this work, the VSM2 consist of maximum six pairs of adiabatic pulses, that enable echo acquisition at six different times. These data could be used for a pixel-wise calculation of T_2 of the venous blood.

3.5.3 OEF Calibration

As a last step of the QUIXOTIC approach, the calculated T_2 values of the venous blood have to be calibrated to get the OEF values. Such a calibration was done by Zhao et al. [2007]. He used bovine blood, which consists of erythrocytes, that have a similar shape, size and water permeability as human cells [Benga and Borza, 1995]. He did several experiments with blood consisting of different hematocrit values and different oxygenation status. In this work, for oxygenation calibration a hematocrit value of 0.44

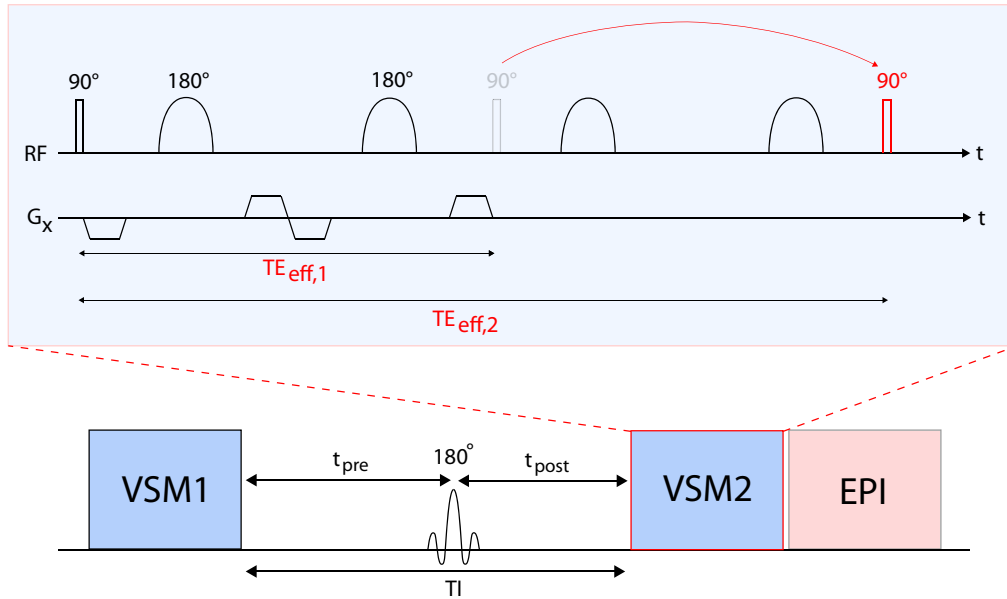


Figure 3.20 Modification of VSM2. An additional pair of adiabatic 180° pulses preserves the T_2 -weighting of the sequence and enables signal acquisition at a longer echo time. By adding more pairs of adiabatic 180° pulses, the acquisition of images at even longer echo times can be realized.

was used. The empirical formula found for this hematocrit value can be written as [Zhao et al., 2007]

$$R_2 = 8.3 + 33.6(1 - Y) + 71.9(1 - Y)^2. \quad (3.73)$$

The calibration curves for three different Hct values are illustrated in Fig. 3.21.

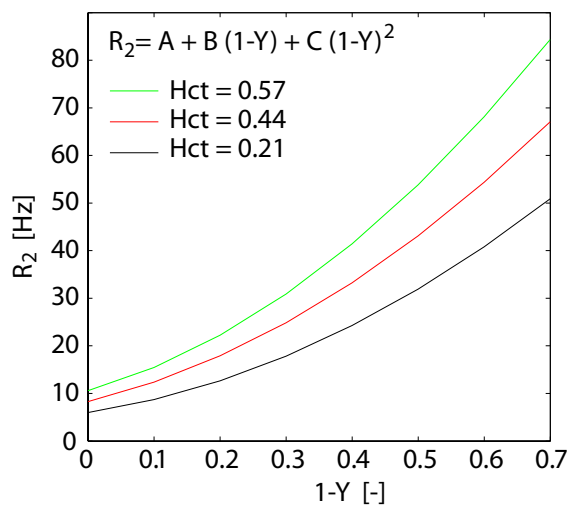


Figure 3.21 R_2 -oxygenation-calibration curve. The plot shows the empirical curves for three different Hct: Hct = 0.57 ($A = 10.6$, $B = 39.3$, $C = 94.3$), Hct = 0.44 ($A = 8.3$, $B = 33.6$, $C = 71.9$), Hct = 0.21 ($A = 6.0$, $B = 21.0$, $C = 61.6$). The empirical found equation and values are adopted from Zhao et al. [2007]. This equation enables the calculation of the OEF value from a known T_2 value of the blood.

4 Results

In the previous section, several methods for quantitative and qualitative oxygenation measurements were described. These methods consist partly of analytical methods based on a tissue model (TPF-, SQ- and TSC-method). Another technique is based on the isolation of the signal of venous blood from the rest of the signal (VSSL) and the last one is an oxygenation based contrast method (SWI). This section presents the results of the measurements. These findings were achieved carrying out phantom measurements and *in vivo* measurements of the different techniques.

4.1 TPF-Method

This section presents the results of the measurements of the TPF-method. The images of the single sequences are presented but also the fit, the macroscopic field correction method and finally the OEF calculation. Figure 4.1 shows the original images acquired with the

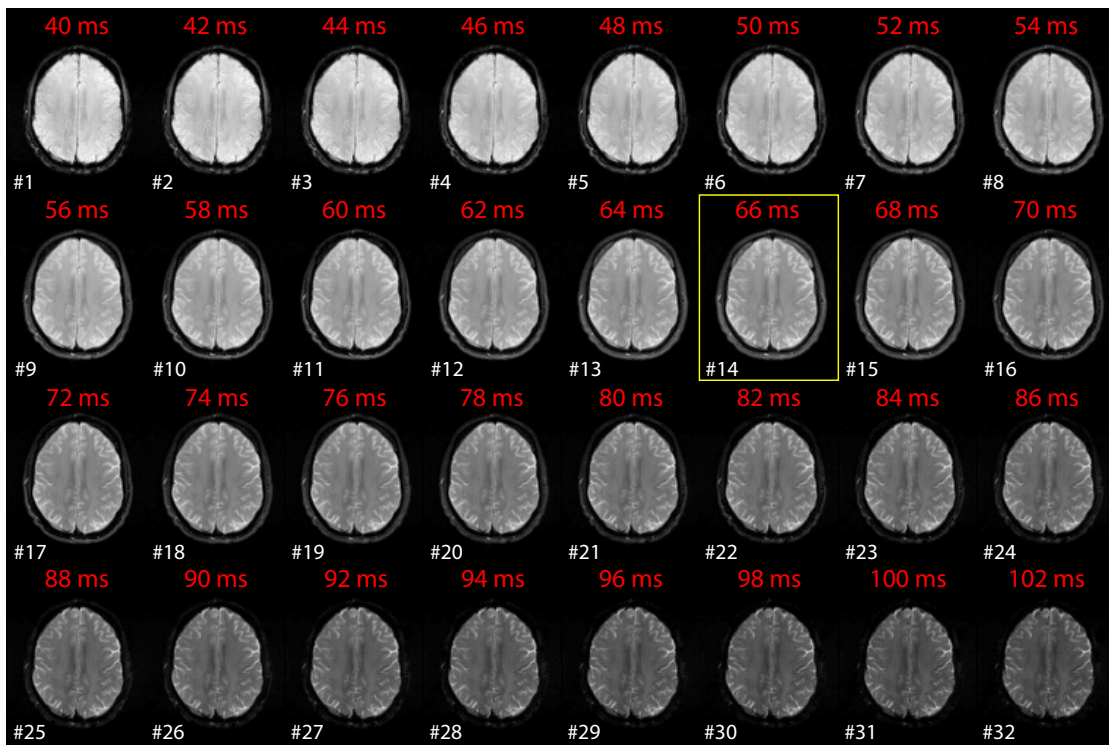


Figure 4.1 Data from the GESSE sequence. The echoes 1-13 show the gradient echoes before the spin echo, echoes 15-32 show the gradient echoes after the spin echo. Echo number 14 (yellow box) shows the spin echo. The red and white numbers show the echo time and the echo number of the respective echo.

Table 4.1 Measurement parameters of the TPF- and the SQ-method. While the GESSE sequences sample the signal around a spin echo to calculate the tissue oxygenation, the MMGE sequences are used for magnetic field mapping. The EPI sequence is performed during contrast agent injection to calculate the CBV.

Sequence	GESSE _{TPF}	MMGE _{TPF}	GESSE _{SQ}	MMGE _{SQ}	EPI _{SQ}
TE [ms]	66 (SE)	5 (1 st)	99.5 (SE)	4.92 (1 st)	45
TR [ms]	2000	100	1500	100	1450
FA [°]	90	20	90	25	90
Matrix size	128×96	256×192	128×104	256×208	128×104
FOV [mm ²]	256×192	256×192	256×208	256×208	256×208
d [mm]	6	3	6	2	6
BW [Hz/Px]	1400	500	440	230	1345
Averages	8	4	6	1	1
Contrasts	32	12	32	5	50
GE for SE	14	-	13	-	-
Δt_{TE} [ms]	2	5	3.5	7.38	1.56
Slices	1	4	1	6	1
TA [min:s]	25:36	3:50	15:38	2:05	1:18

GESSE sequence (section 3.2.2.1). The imaging parameters are presented in Tab. 4.1. In the presented measurement, the 14th image coincides with the spin echo. Therefore the signal of the images 1-13 decays with a relaxation rate R_{2b} (Eq. 3.40). The signal of the images acquired after the spin echo decays with a relaxation rate R_{2a} (Eq. 3.41), which is equal to R_2^* . The acquired data is influenced by macroscopic field inhomogeneities (section 3.3). To correct the data, a MMGE sequence with a high resolution is applied. The parameters are presented in Tab. 4.1. The time interval between two images was 5 ms. Figure 4.2 shows the original phase images for the 12 acquired echoes. Phase inhomogeneities can hardly be seen in the first echo, while at later echoes the phase values especially at the boundary become larger. As phase values can only be presented between $-\pi$ and π , phase wraps appear. These are removed by an algorithm by Herráez et al. [2002]. Moreover, to focus on the interesting parts of the image, a mask was applied to suppress any background noise from outside of the investigated object. The resulting images are presented in Fig. 4.2. These unwrapped phase images can now be used to calculate the deviation of the magnetic field in a certain voxel from the main magnetic field. If there was no deviation, the precession frequency would coincide with the Larmor frequency and no phase offset $\Delta\phi$ would exist. The higher the magnetic field offset, i.e. the magnetic field inhomogeneity, the faster the phase value increases. The magnetic field offset can then be calculated by the time development of the phase,

$$\Delta B = \frac{\Delta\omega}{\gamma} = \frac{1}{\gamma} \cdot \frac{\Delta\phi}{\Delta t}. \quad (4.1)$$

Figure 4.3 shows the linear relationship between phase and time in the magnetic field mapping experiment. The two presented ROIs were placed in a homogeneous part of the white matter (blue) and at the boundary of the brain in the region of gray matter

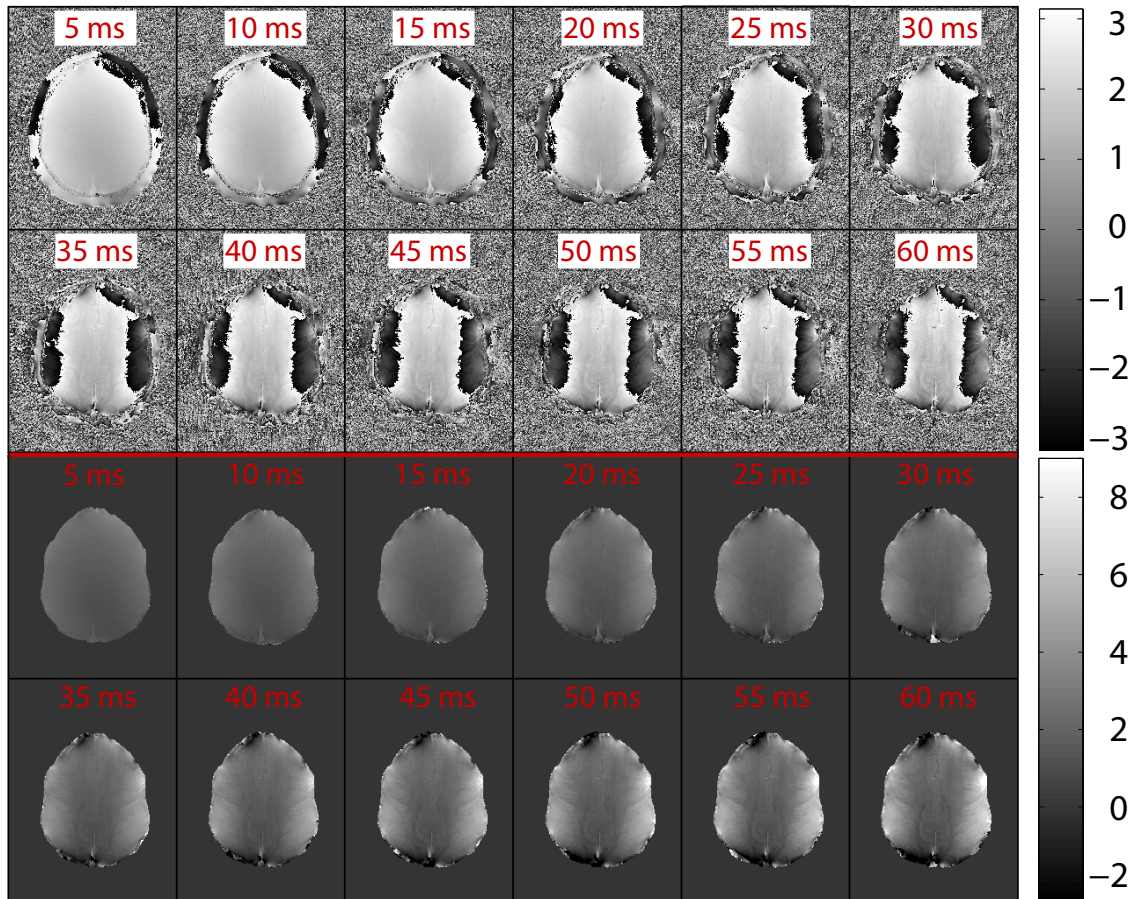


Figure 4.2 Magnetic field inhomogeneities: Wrapped and unwrapped phase images of the second slice. The first two rows show phase images recorded at echo times between 5 ms and 60 ms in time intervals of 5 ms. The scale reaches from $-\pi$ to $+\pi$. The second two rows show the respective unwrapped phase images with a scale from -3 to 9 after the application of an image mask.

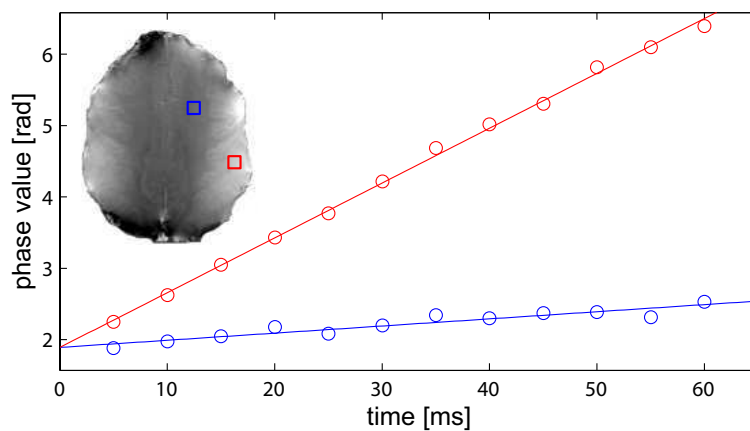


Figure 4.3 Phase development in two different ROIs. The ROIs are placed in gray matter (red) and white matter (blue). By linear regression the frequency offset $\Delta\omega$ for each voxel can be calculated, which enables the determination of ΔB in the respective voxel. This is important for macroscopic field inhomogeneity correction.

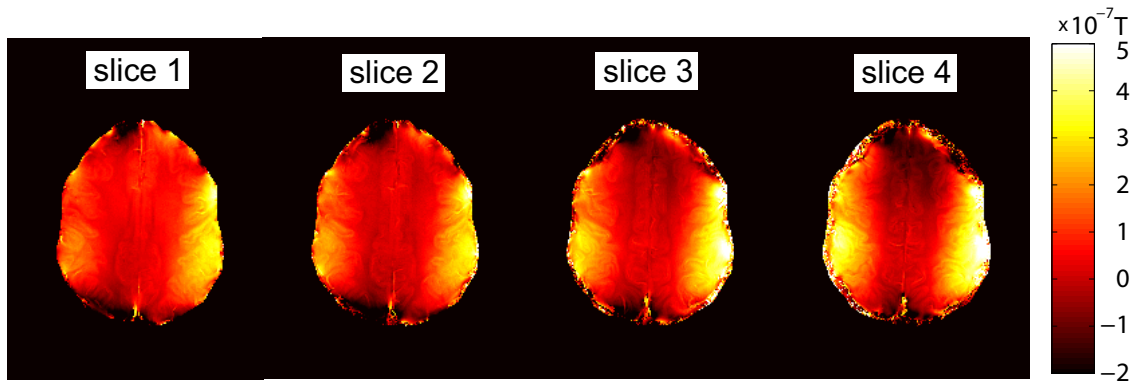


Figure 4.4 Magnetic field inhomogeneity maps for the four acquired GRE-slices. Slice 2 and 3 are located in the GESSE slice and are therefore relevant for the calculation of gradient maps in x - and y -direction. Slice 1 and 4 (together with slice 2 and 3) are used to calculate the gradient map in z -direction.

(red). By linear regression the slope can be calculated. For the example of Fig. 4.3, the slopes for the blue ROI and the red ROI are $0.01 \frac{\text{rad}}{\text{ms}}$ and $0.08 \frac{\text{rad}}{\text{ms}}$, respectively. According to Eq. 4.1, this results in calculated magnetic field inhomogeneities of $3.7 \cdot 10^{-8} \text{ T}$ and $2.87 \cdot 10^{-7} \text{ T}$, respectively. Figure 4.4 shows the calculated ΔB maps for all four slices. To correct the acquired GESSE data for magnetic field inhomogeneities, the magnetic gradient maps have to be calculated (Eq. 3.34). This can be done by investigating the two adjacent voxels in the respective direction. Figure 4.5 shows a sketch of the gradient calculated in y -direction. Assuming four acquired slices, this results in four slices of G_x and G_y maps and two slices of G_z maps. For x - and y -gradient maps only the two inner

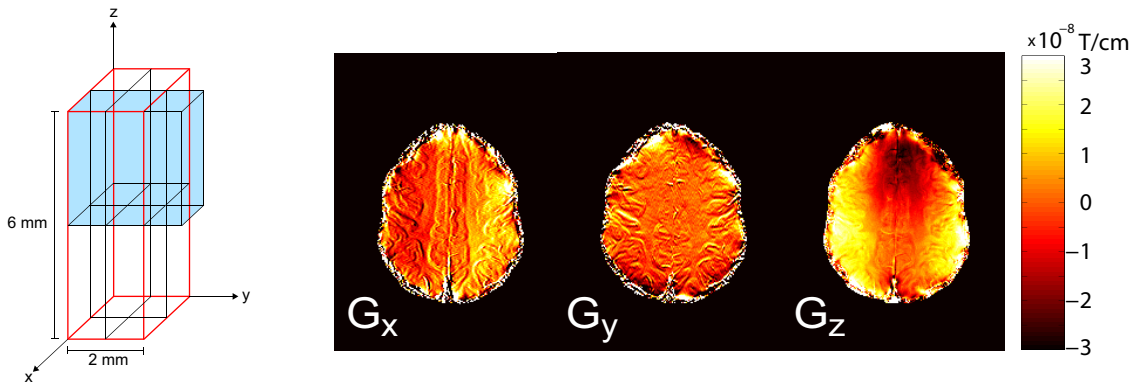


Figure 4.5 Gradient map calculation. **Left:** The voxel size of the high resolution phase maps (black) is chosen to be half the size of the GESSE sequence (red) in each dimension. The exemplary calculation of the gradient in y -direction is illustrated for one voxel. For the gradient calculation in the respective direction, the ΔB values of the two adjacent voxels are used (blue voxels). **Right:** The gradient maps for the three dimensions are presented. The gradient map in z -direction shows large inhomogeneities at the left and right boundary of the brain.

slices are used for averaging, while for the z -gradient map both acquired slices are used. The resulting high resolution G_x , G_y and G_z maps are presented in Fig. 4.5. If the gradients of the macroscopic field inhomogeneities are known, the correction function for the GESSE data set can be calculated. According to Eq. 3.37, the original data has to be divided pixel-wise by this time-dependent correction function. Figure 4.6 shows the resulting correction maps in x -, y - and z -direction for six different times. Moreover, it presents the resulting total correction function for these times. The greater the distance to the spin echo, the higher the impact of the correction function (Eq. 3.34). To enable a pixel-wise correction, these images have to be downscaled to GESSE sequence resolution. The signal development in the two ROIs and the respective signal correction can be seen in Fig. 4.7a.

4.1.1 OEF Calculation

In this section, the quantification of the tissue oxygenation is being performed. As already mentioned, the information about the quantification is contained in the signal behavior around a spin echo (section 3.4). To illustrate the data post processing, the signal intensity of a certain voxel is investigated. Figure 4.7a shows the uncorrected and corrected values

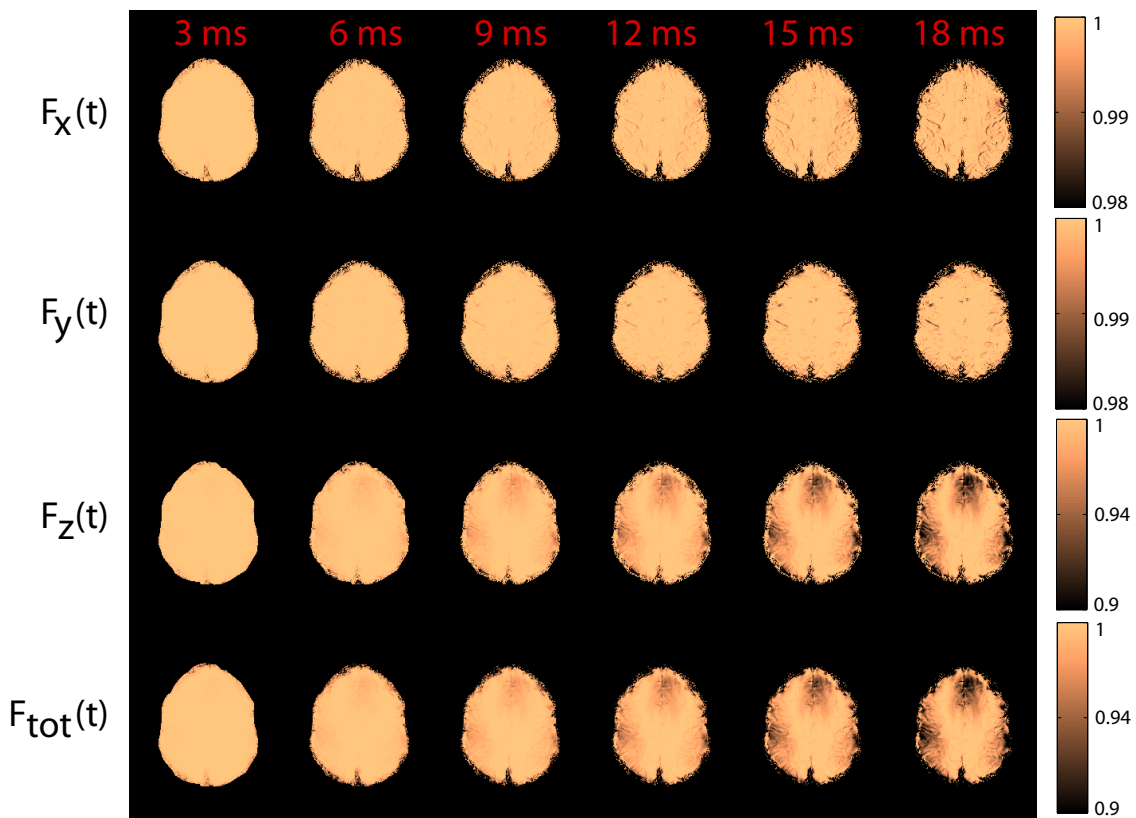


Figure 4.6 Three-dimensional correction function. While the influence of macroscopic field inhomogeneities in x - and y -direction is rather small, the correction factor in z -direction has a big influence on the signal. One reason for this is the larger extension in the respective direction (in-plane resolution: 2 mm, slice thickness: 6 mm).

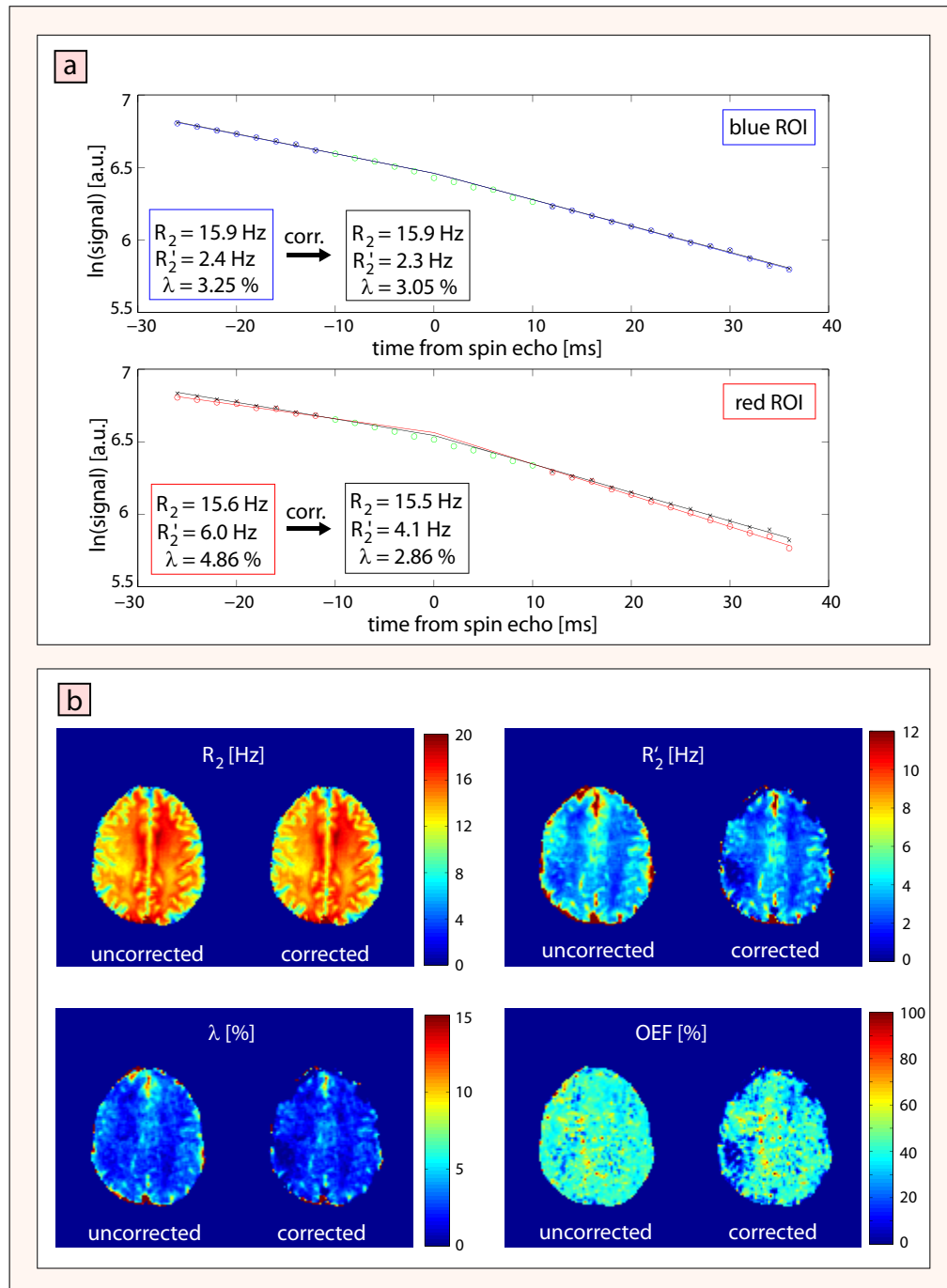


Figure 4.7 Signal behavior around a spin echo in two different regions of the brain and parameter maps calculated with the TPF-method. **a)** The homogeneous region (top) is hardly influenced by the macroscopic field inhomogeneities resulting in very little signal correction. In a more heterogeneous region (bottom), the signal has to be corrected resulting in different R_2' and λ values **b)** The images show the uncorrected and the corrected parameter maps of R_2 , R_2' , λ and OEF. While on the R_2 maps no influence of the inhomogeneities can be found, on the other parameter maps the correction function has a strong influence, e.g. the venous blood volume is overestimated at the boundary without correction.

of the blue and the red ROI of Fig. 4.3. The three-parameter fit yields the following three uncorrected values for the ROI in the inhomogeneous region: $R_2 = 15.6$ Hz, $R'_2 = 6.0$ Hz, $\lambda = 4.86$ %. After correction, the corresponding values become $R_2 = 15.5$ Hz, $R'_2 = 4.1$ Hz and $\lambda = 2.86$ %.

By pixel-wise analysis, R_2 , R'_2 and λ maps can be calculated. The corrected and uncorrected maps are illustrated in Fig. 4.7b. As expected, there is hardly any difference between the R_2 maps, because in any T_2 -weighted imaging experiment, all inhomogeneities are refocused due to the 180° pulse. In contrast to that, there is a significant difference between the two R'_2 maps. The big influence of the inhomogeneities can be seen in particular at the boundary. According to Eq. 3.43, the R'_2 and the λ values can now be used for a pixel-wise determination of the OEF. The resulting uncorrected and corrected OEF maps are illustrated in Fig. 4.7b. The OEF map shows hardly any visible contrast between gray matter and white matter. As a next step, gray and white matter masks are created from a T_2^* -weighted image. Table 4.2 shows the results for R_2 , R'_2 , λ and OEF values with the corresponding standard deviations.

4.2 SQ-Method

This section presents the results of the SQ-method. The sequence parameters of the GESSE sequence are presented in Tab. 4.1. In contrast to the TPF-method, a thinner slice thickness (2 mm) for the field maps was used. Figure 4.8a shows the sketch of the gradient calculation. This invasive method was applied in tumor patients in clinical routine. The moment of contrast agent injection was used for the DSC measurement to enable CBV calculation. In this study, the total measurement time had to be shortened, because of the long investigation time of the patients in the MR scanner due to clinical investigations. Therefore some parameters had to be changed compared to the TPF-method. Figure 4.8b shows a T_2^* -weighted image to illustrate the location of the tumor. In the presented case, the tumor was an acoustic neuroma, which is a benign primary intracranial tumor of the myelin-forming cells of the vestibulocochlear nerve, arising from the Schwann cells. The GESSE sequence has to be applied before the DSC perfusion sequence because the paramagnetic contrast agent (Gd-DTPA) is injected during the perfusion measurement and it takes a long period of time until it is washed out again. The parameters for the perfusion EPI are illustrated in Tab. 4.1. After the AIF had

Table 4.2 Parameters of white matter and gray matter. The reversible relaxation rate R_2 (in Hz), the reversible relaxation rate R'_2 (in Hz), the venous blood volume λ (in %), and the oxygen extraction fraction (OEF) (in %) are presented with and without macroscopic inhomogeneity correction.

	WM	WM _{corr}	GM	GM _{corr}
R_2	14.91 ± 1.37	14.91 ± 1.37	11.57 ± 3.20	11.56 ± 3.20
R'_2	2.66 ± 0.68	2.30 ± 0.73	4.90 ± 3.14	3.50 ± 2.39
λ	2.16 ± 0.97	1.87 ± 0.93	3.96 ± 2.82	2.83 ± 2.12
OEF	44.31 ± 17.35	42.86 ± 16.29	43.31 ± 14.05	43.89 ± 14.44

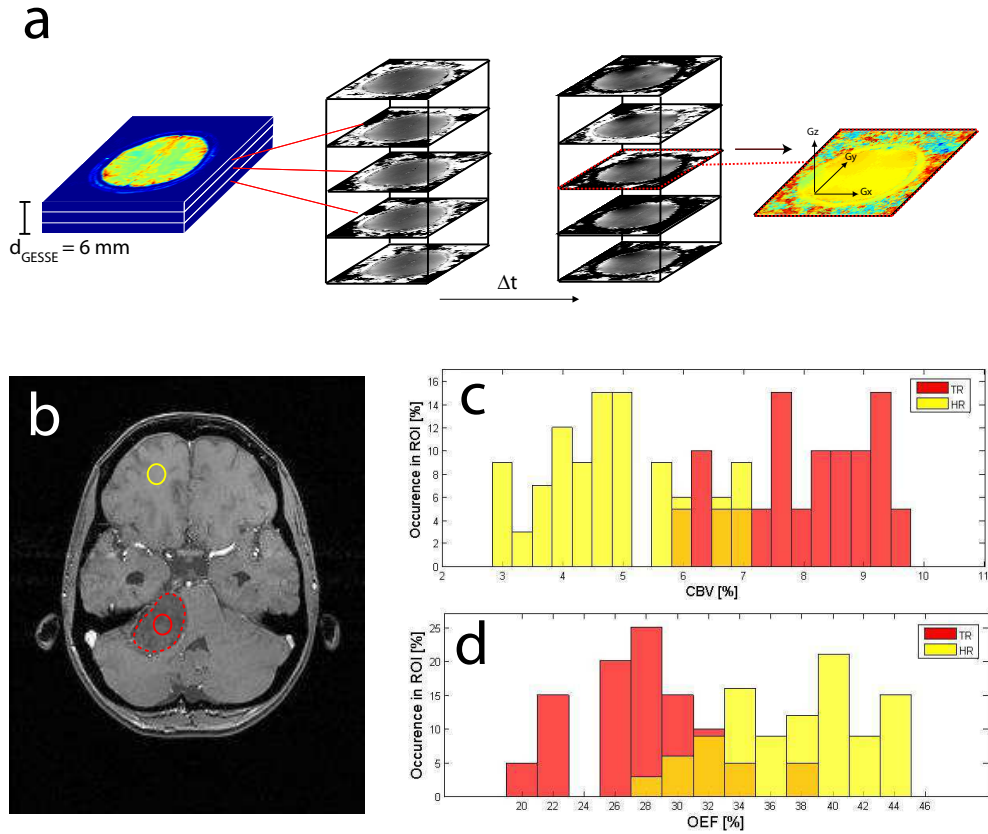


Figure 4.8 Experimental setup, location of the ROIs and corresponding CBV and OEF histograms. **a)** Sketch of the experimental setup. The slice thickness of the GESSE sequence is three times larger than the one of the high resolution phase mapping sequence. These measurements are performed before contrast agent injection. **b)** One ROI is placed in the healthy region (yellow circle), the other in the tumorous region (red circle). The tumorous area is marked with a dashed red line. **c)** CBV and **d)** OEF map of the two regions. While the CBV in the healthy region is lower than in the tumorous region, the OEF in the healthy region is higher.

been chosen, the CBV could be calculated (Eqs. 3.46 and 3.47). Two different ROIs were chosen, one in the white matter of a healthy region and one in the tumorous region (Fig. 4.8b). The calculated histograms of the CBV values in these two regions as well as the OEF values, calculated from the CBV and the R_2' from the GESSE measurement, are presented in Fig. 4.8c and 4.8d. It can be seen that in the tumorous region the blood volume is higher and the OEF value is significantly lower than in the healthy region. The CBV in the healthy and the tumorous region can be calculated as $(4.87 \pm 1.17) \%$ and $(8.02 \pm 1.11) \%$, respectively. The OEF values are $(37.54 \pm 4.55) \%$ and $(27.80 \pm 4.31) \%$ in healthy and tumorous tissue, respectively.

4.3 TSC-Method

This section presents the results of the different measurements evaluated with the TSC-method. For R_2 , R_2^* , ΔB and λ map calculation, a CPMG, a MMGE, a high resolution MMGE and a GESSE sequence have to be applied (Fig. 4.9). Figure 4.10 shows the resulting maps for the relaxation times R_2 and R_2^* as well as the R_2' map, which is calculated by pixel-wise subtraction of the R_2 -value from the R_2^* -value. The R_2 and the

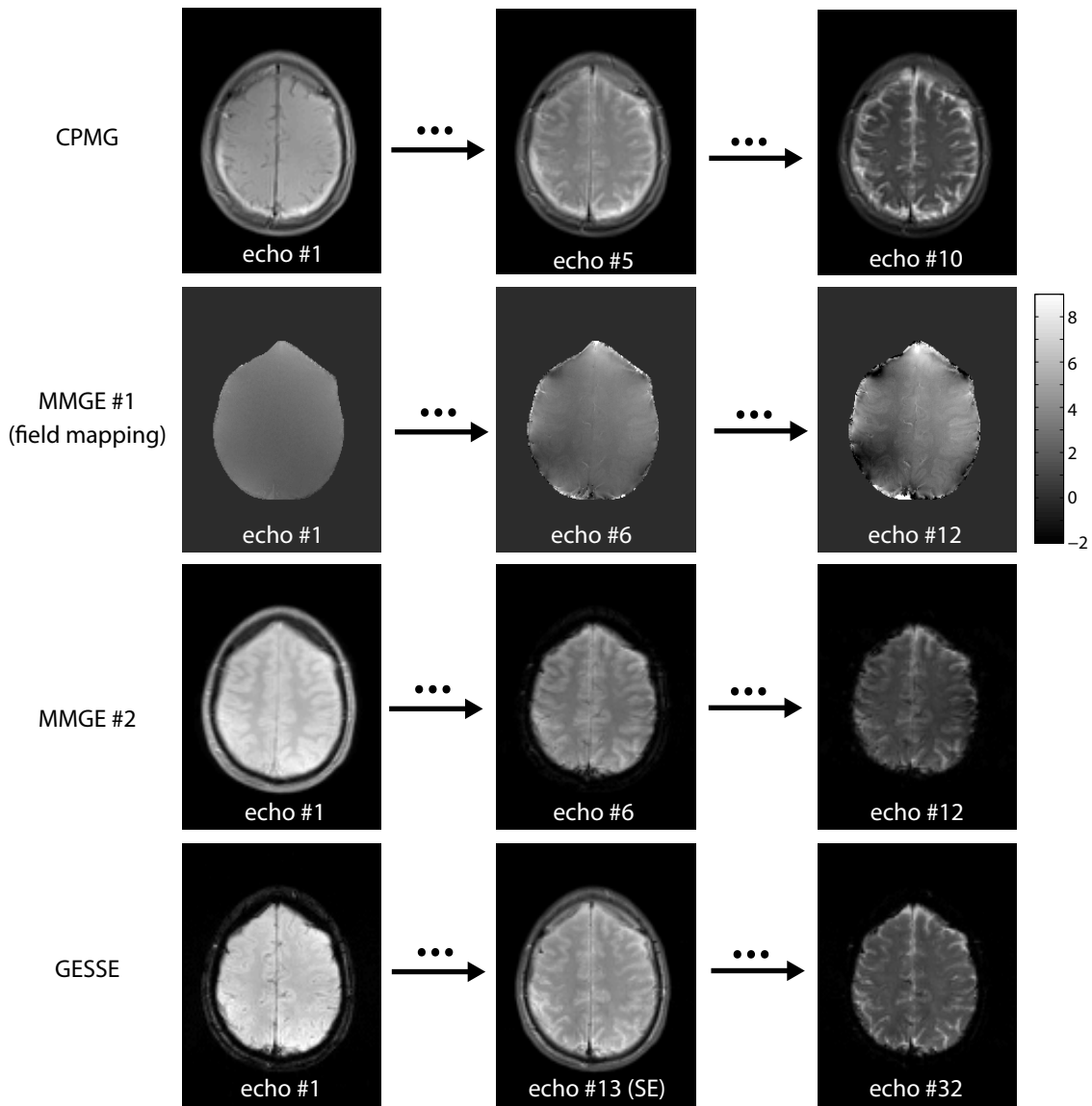


Figure 4.9 TSC-Method. The CPMG sequence is used to calculate R_2 maps, the following high resolution MMGE sequence enables signal correction by gradient map calculation. Subsequently, another MMGE sequence with the same resolution as the CPMG sequence is performed to calculate R_2^* maps. As a last step, a GESSE sequence is applied for signal sampling around a spin echo to enable the determination of λ .

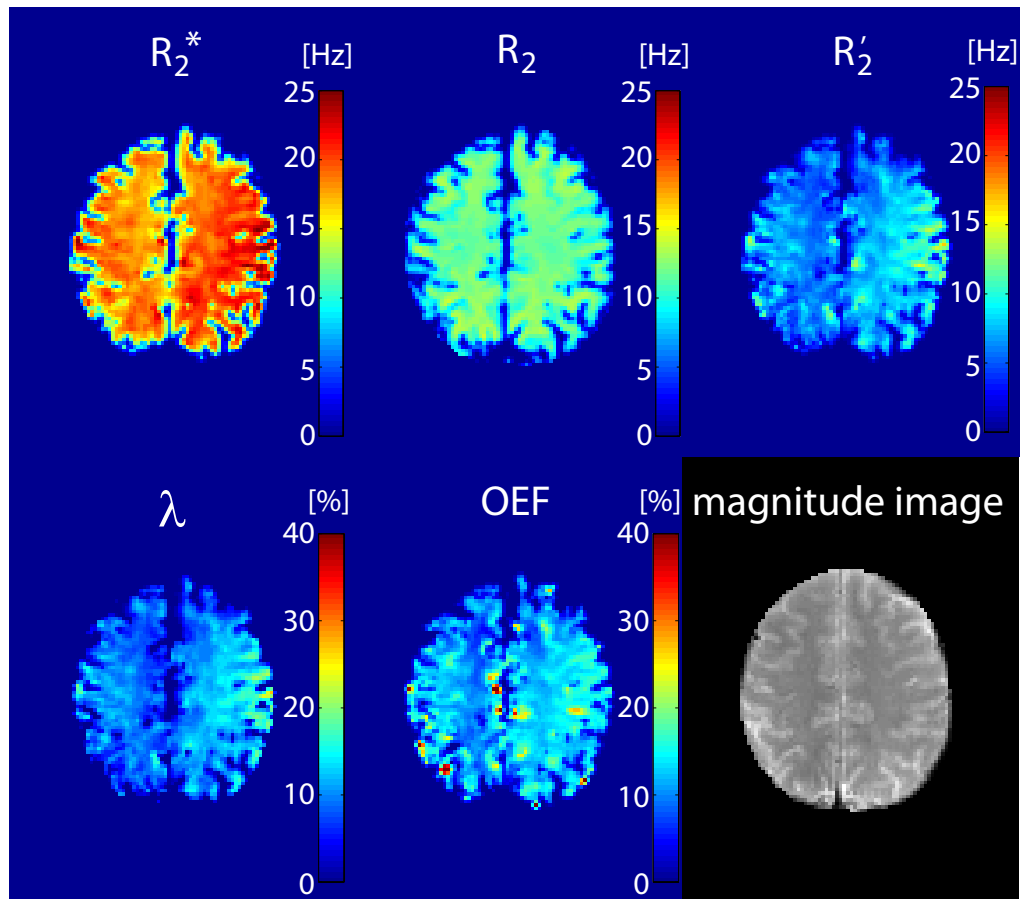


Figure 4.10 Parameter maps of the TSC-method. In this work, a Hct ratio of 0.34 in small vessels was assumed [Eichling et al., 1975], which is typical for healthy humans. For the susceptibility difference between completely deoxygenated and completely oxygenated red blood cells the value 0.27 ppm [Spees et al., 2001] was used.

R'_2 values are used as fit parameters for the signal equation (Eq. 3.39), resulting in a map of the deoxygenated blood volume λ . With R'_2 and λ as input factors, Eq. 3.43 can now be used to calculate the OEF map. Here, a Hct value of 0.34 [Eichling et al., 1975] and a $\Delta\chi_{\text{do}}$ value of 0.18 ppm were used [Spees et al., 2001]. The parameters of the imaging sequences (without sequence correction, cf. section 4.3.1) are presented in Tab. 4.3. The values of R_2 , R'_2 , λ and OEF in white and gray matter are presented in Tab. 4.5. It can be seen that although the λ and the OEF maps look very homogeneous, there is an overestimation of λ and an underestimation of the OEF. To illustrate this, a ROI in the white matter was investigated. Figure 4.11 shows the signal decay in this ROI and the corresponding fit. It can be seen that the slopes before and after the spin echo were not calculated correctly. Therefore the mistake has to be found in R_2 and R'_2 calculation.

Table 4.3 The imaging parameters of the four sequences of the TSC-method. The total acquisition time was approximately 57 minutes.

Sequence	CPMG	MMGE (Phase)	MMGE (Mag.)	GESSE
TE [ms]	13.1 (1 st)	5 (1 st)	5 (1 st)	59 (SE)
TR [ms]	2000	100	3000	2000
FA [°]	90	20	90	90
Matrix size	128×96	256×192	128×96	128×96
FOV [mm ²]	256×192	256×192	256×192	256×192
d [mm]	6	3	6	6
BW [Hz/Px]	200	500	500	1400
Averages	6	2	4	8
Contrasts	20	12	12	25
GE for SE	-	-	-	13
Δt_{TE} [ms]	13.1	5	5	2
TA [min:s]	14:28	2:34	14:24	25:36
Phase part. Four.	6/8	-	6/8	-

4.3.1 Phantom Measurements: Sequence Correction

To determine the origin of the falsification of the calculated relaxation times, the sequences that are responsible for their determination were investigated. For the following investigations the relaxation phantom presented in section 3.2.3.3 was used. First, the

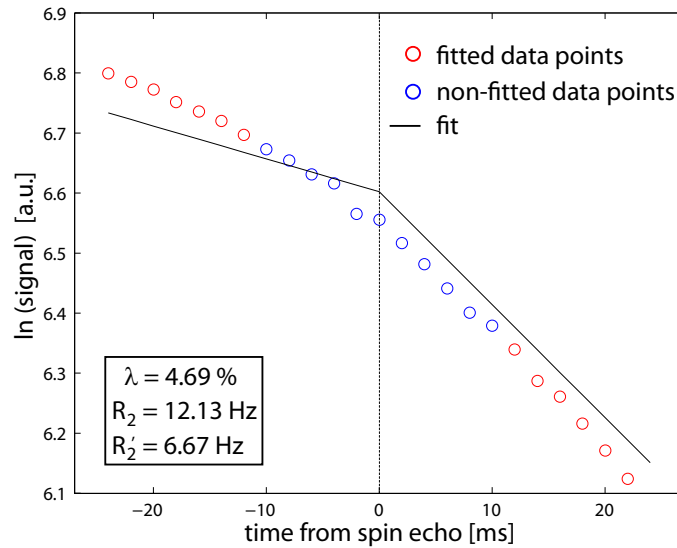


Figure 4.11 Data fit of the TSC-method. It can be seen that the slopes before and after the spin echo are not calculated correctly. While the slope behind the spin echo is slightly underestimated, the slope before the spin echo shows a strong underestimation compared to the GESSE data.

GESSE sequence is applied. Seven data points from 10 ms (long-term regime, Eq. 3.26) after the spin echo are used for R_2^* fitting. Secondly, the MMGE sequence is applied. The resulting R_2^* maps for both measurements are illustrated in Fig. 4.12.

Correspondingly, the first seven data points (long-term regime) of the GESSE measurement were used for $R_{2,b}$ mapping. As can be seen in Eq. 3.40, the slope after the 180°

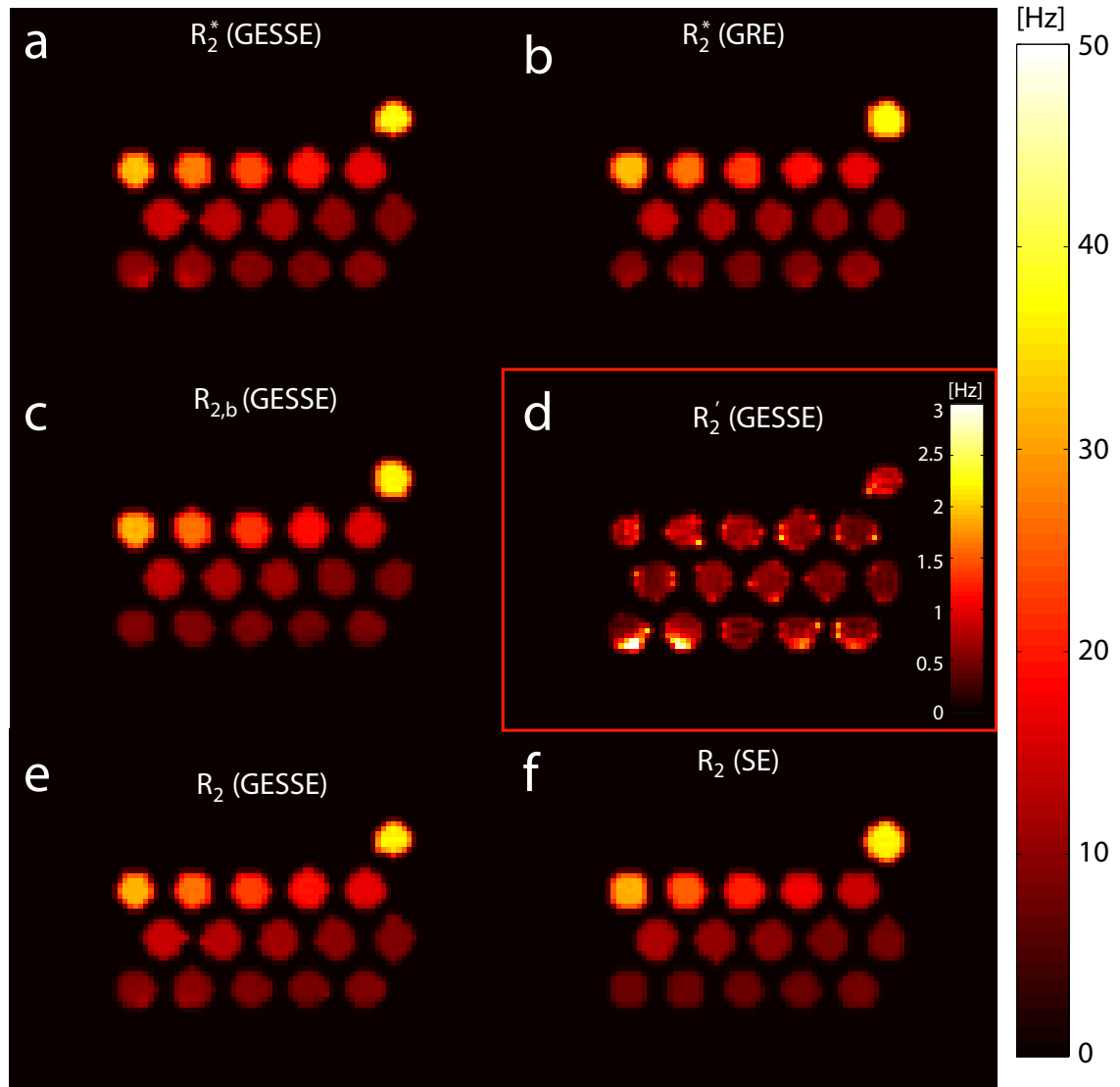


Figure 4.12 Comparison of the different sequences using the relaxation phantom. R_2^* maps calculated from a) the GESSE data and b) the MMGE data, c) $R_{2,b}$ map calculated from the data points before the spin echo, d) R_2' map that can be calculated from the GESSE data, e) Resulting R_2 map calculated from the GESSE data, f) R_2 map calculated from the data of the CPMG-sequence.

pulse and before the spin echo can be written as

$$\begin{aligned} R_{2,b} &= R_2 - R'_2 \\ &= R_2^* - 2 R'_2. \end{aligned} \quad (4.2)$$

The fit of the data before the spin echo yields $R_{2,b}$, which can be used in combination with the original R_2^* fit of the data behind the spin echo to determine R'_2 . Using this information, R_2 can be calculated. This measurement can be compared to a CPMG measurement and the resulting R_2 map. In analogy to the mentioned R_2^* comparison, Fig. 4.12 shows the R_2 maps calculated from the data acquired with the different sequences. The different R_2^* and R_2 values for ROIs in the different tubes are presented in Figs. 4.13a and 4.13b. The resulting average values and standard deviations are presented in Tab. 4.4. Keeping in mind that the OEF determination will be performed in the brain, the interesting range for relaxation rates is between 10.10 Hz (gray matter) and 14.49 Hz (white matter) [Stanisz et al., 2005]. This area is marked with a yellow box in Fig. 4.13. Therefore further investigations concerning the values in this range of magnitude resulting in the probes with a contrast agent concentration between 0.6 mM and 1.5 mM, were performed. The calculated R_2^* values are well inside or just below the error range. Figure 4.13c shows the percentage underestimation of R_2^* by the MMGE sequence compared to the GESSE sequence. It can be seen that in the investigated range the average value of the four data points is 4.65 %. The comparison of Fig. 4.13a and Fig. 4.13b shows that the falsification in the calculation of λ and OEF does not have its

Table 4.4 Relaxation rates in dependency of the contrast agent concentration calculated with different sequences. The R_2^* values are compared by a GESSE and a MMGE sequence. The R_2 -value are compared by a GESSE and a CPMG sequence.

Concentration [mM]	R_2^* (GESSE) [Hz]	R_2^* (GRE) [Hz]	R_{2b} (GESSE) [Hz]	R_2 (GESSE) [Hz]	R_2 (SE) [Hz]
5	$37,71 \pm 2.70$	37.40 ± 0.98	36.79 ± 1.55	36.80 ± 2.03	36.69 ± 1.44
4	32.57 ± 1.29	32.07 ± 0.47	31.55 ± 1.87	31.67 ± 0.79	31.17 ± 0.33
3	27.59 ± 1.33	26.83 ± 0.49	26.36 ± 1.43	26.72 ± 1.01	25.16 ± 0.23
2.5	23.48 ± 0.77	22.77 ± 0.59	22.26 ± 0.83	22.86 ± 0.72	20.72 ± 0.22
2	20.06 ± 0.38	19.53 ± 0.58	18.86 ± 0.80	19.45 ± 0.52	17.20 ± 0.26
1.5	16.88 ± 0.17	16.70 ± 0.92	16.15 ± 0.30	16.51 ± 0.12	14.26 ± 0.33
1	14.86 ± 0.21	14.31 ± 0.93	14.04 ± 0.58	14.43 ± 0.19	11.93 ± 0.19
0.8	13.46 ± 0.26	12.45 ± 0.58	12.20 ± 0.25	12.83 ± 0.16	10.35 ± 0.09
0.6	12.19 ± 0.24	11.55 ± 0.45	11.12 ± 0.30	11.65 ± 0.17	9.5 ± 0.06
0.4	10.16 ± 0.14	9.90 ± 0.34	9.18 ± 0.39	9.66 ± 0.16	8.22 ± 0.04
0.3	9.35 ± 0.25	9.59 ± 0.47	8.58 ± 0.32	8.95 ± 0.09	7.84 ± 0.04
0.2	9.96 ± 0.55	9.28 ± 0.54	9.03 ± 0.42	9.49 ± 0.34	7.45 ± 0.02
0.1	10.62 ± 0.70	9.59 ± 0.66	9.19 ± 0.77	9.88 ± 0.54	7.35 ± 0.06
0.05	9.32 ± 0.89	8.88 ± 0.87	8.56 ± 0.43	8.84 ± 0.54	7.08 ± 0.04
0.02	8.65 ± 0.56	9.43 ± 1.04	7.34 ± 1.12	7.91 ± 0.50	7.11 ± 0.05
0	9.44 ± 0.51	10.43 ± 0.99	8.23 ± 1.03	8.81 ± 0.59	7.83 ± 0.03

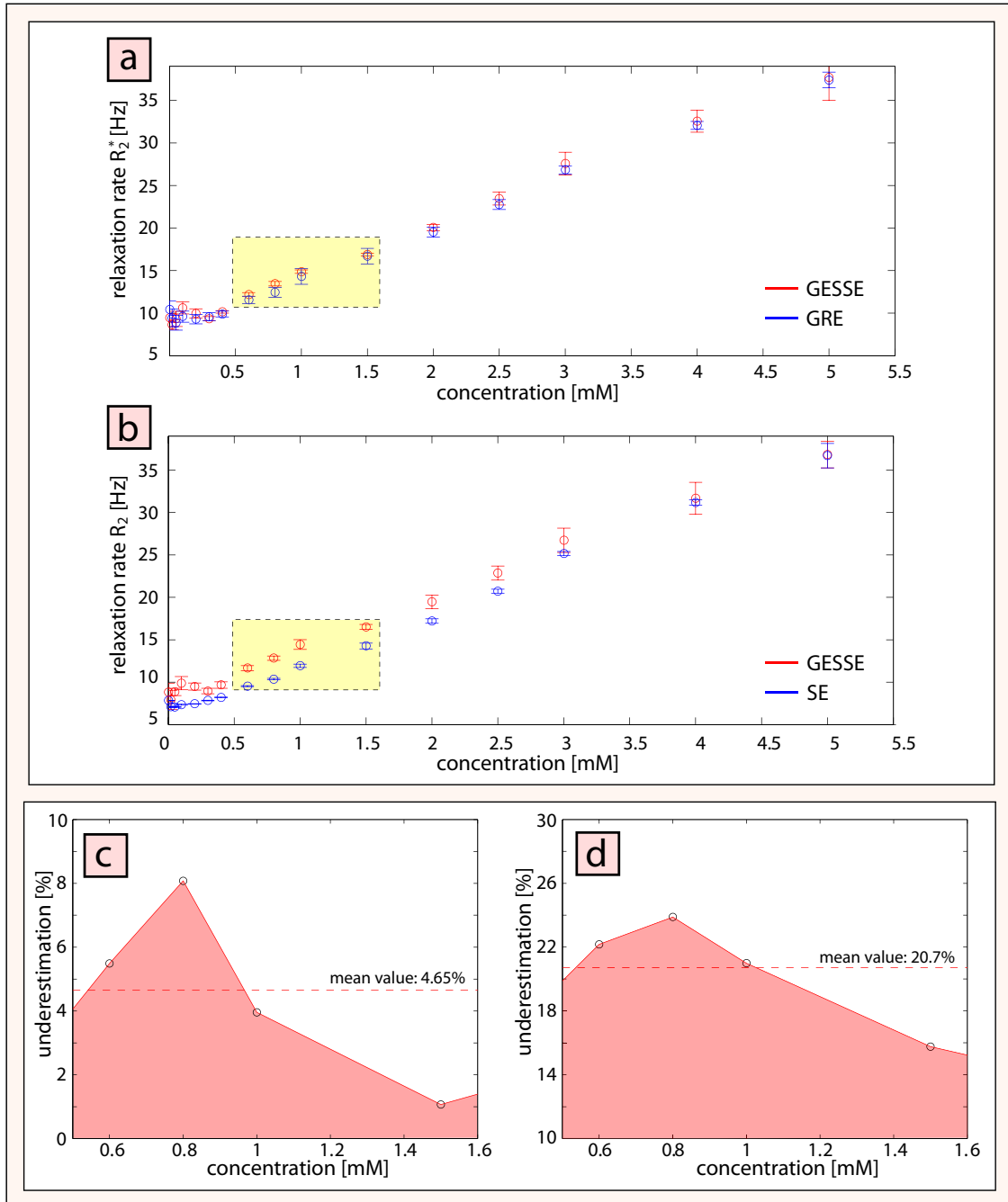


Figure 4.13 Underestimation of the MMGE and CPMG sequence compared to the GESSE sequence. a) Average R_2^* values and standard deviations of the 16 ROIs placed in the 16 tubes of the relaxation phantom. The values are determined by the MMGE and the GESSE sequence. b) Average R_2 values from the CPMG and the GESSE sequence. The yellow box marks the range of R_2 values of gray and white matter in the brain. c) Relative percentage underestimation of R_2^* d) and R_2 . The presented mean value is not the mean value of the whole curve but the mean value of the four relevant data points.

main origin in the R_2^* calculation. This was already presumed because in Fig. 4.11 the slope of the fit curve behind the spin echo (which is R_2^*) corresponds well to the acquired data points. Therefore the main reason for the error in the fit must be found in the determination method of R_2 . The different R_2 values for ROIs in the different tubes are presented in Fig. 4.13b. It can be seen that there is a global underestimation of R_2 with the CPMG sequence compared to the GESSE sequence, which is illustrated in Fig. 4.13d. The percentage average value of this range was calculated as 20.7%. This results in the following "adjusted" values of the MMGE and CPMG data,

$$R_{2,\text{corr}}^* = 1.0465 \cdot R_{2,\text{MMGE}}^*, \quad (4.3)$$

$$R_{2,\text{corr}} = 1.2070 \cdot R_{2,\text{CPMG}}. \quad (4.4)$$

4.3.2 Phantom Measurements: Correction Validation

The results of the sequence comparison, i. e. the correction factor for R_2 calculation is now validated with another phantom. Here, the tissue phantom described in section 3.2.3.2, is used. The imaging sequences and the used parameters are the same as for the relaxation phantom measurement. Figure 4.14a shows a T_2^* -weighted image of the two phantoms acquired at an echo time of 40 ms. Moreover, the R_2 map resulting from the CPMG sequence, the R_2^* map and the R_2' map after sequence correction are illustrated. While the R_2 values in both phantoms are of the same order of magnitude, the R_2^* map shows a big difference in both phantoms. The higher R_2 values in the phantom with a string volume fraction of 3% occur due to a higher susceptibility difference inside the voxel compared to the 1%-phantom. This can be verified by a look at the R_2' maps. As a first step, the different ways of R_2^* calculation were investigated. Figure 4.14b shows the averaged R_2^* values of the ROIs of Fig. 4.14a calculated from the GESSE data (blue circles) and from the GRE data (red circles). In addition to that, the uncorrected values from the GRE data are presented (black crosses). The sequence correction causes a good accordance of the GRE data and the GESSE data, while the uncorrected GRE data is globally underestimated compared to the GESSE data. As a next step, the signal behavior before the spin echo is investigated. Figure 4.14c shows the corrected R_2^{before} map calculated with a GESSE data fit. Here, six voxels were chosen to show the sequence correction before the spin echo. The dashed line in the plots shows the slope of the curves calculated with the TSC-method before correction. The continuous black line shows the slope after the correction. In this example, it can be seen that the sequence correction method, that was calibrated with the relaxation phantom shows good results with this tissue phantom. The uncorrected (dashed box) and the corrected relaxation rates for the pixels are presented in the respective plots.

4.3.3 *in vivo* Correction

The effect of the corrected parameters can be seen by comparison of a pixel time series without correction and a time series with correction. Keeping in mind the parameter fit of Fig. 4.11, where a large fit error can be seen. In Fig. 4.15, the same ROI is evaluated again but with corrected values. The parameter fit is much better, resulting in more realistic values for λ and OEF. In this section, the underestimated parameters¹ of the *in vivo* measurements will be corrected and new parameter maps will be created. Figure 4.16 shows the new R_2^* , R_2 and R_2' maps. These corrected values are then used to calculate the λ and the OEF maps, also presented in Fig. 4.16. Table 4.5 shows the parameter results of gray and white matter.

¹*underestimated* does not imply an absolute underestimation of the values, but a relative underestimation of the values calculated with the separate sequences compared to those calculated with the GESSE sequence. This is further discussed in chapter 5.

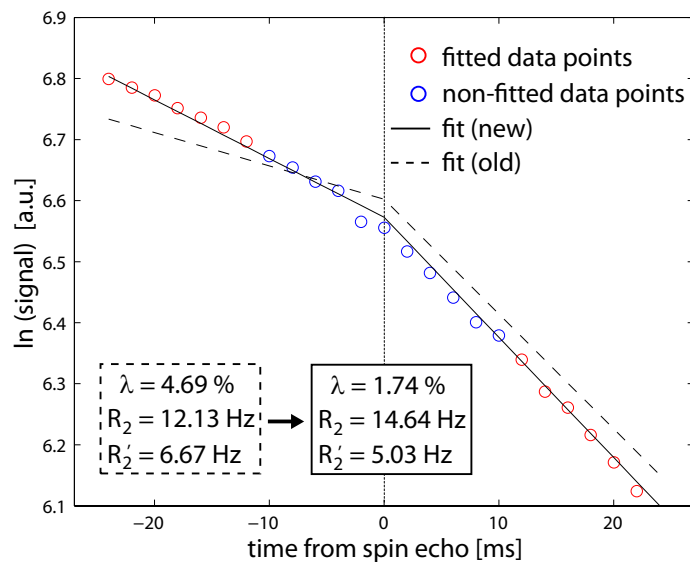


Figure 4.15 Signal decay in a ROI: Corrected TSC-method. The dashed line shows the result from the uncorrected TSC-method, The solid line shows the result from the corrected TSC-method. It can be seen that the fit accuracy is much higher after the sequence correction.

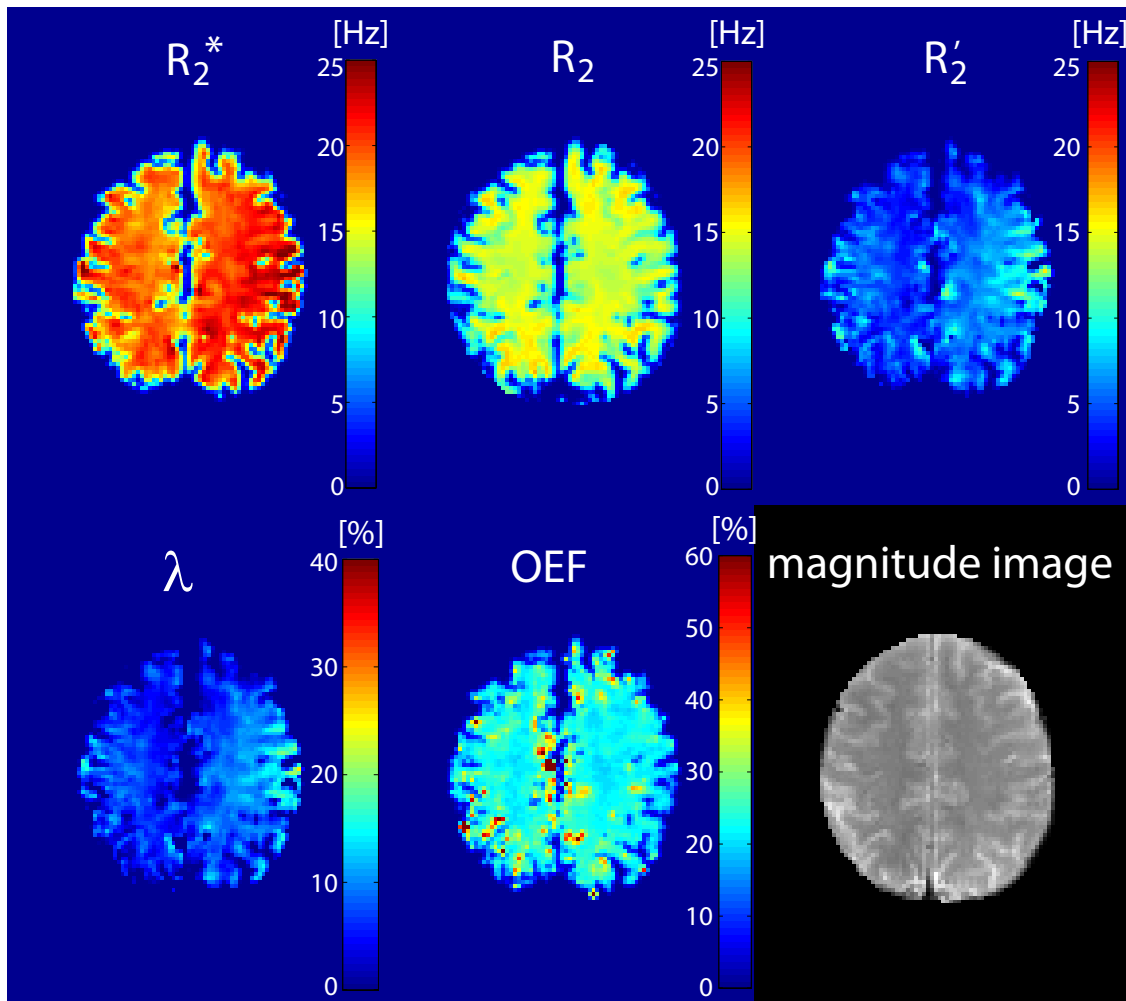


Figure 4.16 Corrected parameter maps of the TSC-method. **Top:** The different relaxation rates R_2^* , R_2 and R_2' are illustrated. **Bottom:** The parameters λ and OEF, resulting from the TPF fit, are illustrated. The comparison with Fig. 4.10 shows the attenuation of the previous overestimated blood volume and a higher OEF value than before correction. The last image shows a T_2^* -weighted reference image of the same slice.

Table 4.5 Parameters of an *in vivo* experiment before and after sequence correction. The parameters are presented in Hz (R_2 and R_2') and in % (λ and OEF).

	WM	WM _{corr}	GM	GM _{corr}
R_2	14.41 ± 0.78	17.40 ± 0.94	12.78 ± 1.79	15.43 ± 2.16
R_2'	7.34 ± 1.44	4.45 ± 1.29	7.99 ± 2.23	5.22 ± 2.01
λ	9.73 ± 1.94	6.79 ± 2.13	7.05 ± 5.58	5.03 ± 4.88
OEF	20.61 ± 1.64	21.99 ± 3.44	23.71 ± 3.04	26.91 ± 6.51

4.4 Velocity-Selective Spin Labeling

This section presents phantom as well as *in vivo* experiments with the VSSL technique. Linearly directed flow was used to qualitatively demonstrate the influence of a VSM, because the flow through randomized cylinders is difficult to realize in a phantom measurement. Afterwards, the results of the VSSL technique in an *in vivo* measurement is presented.

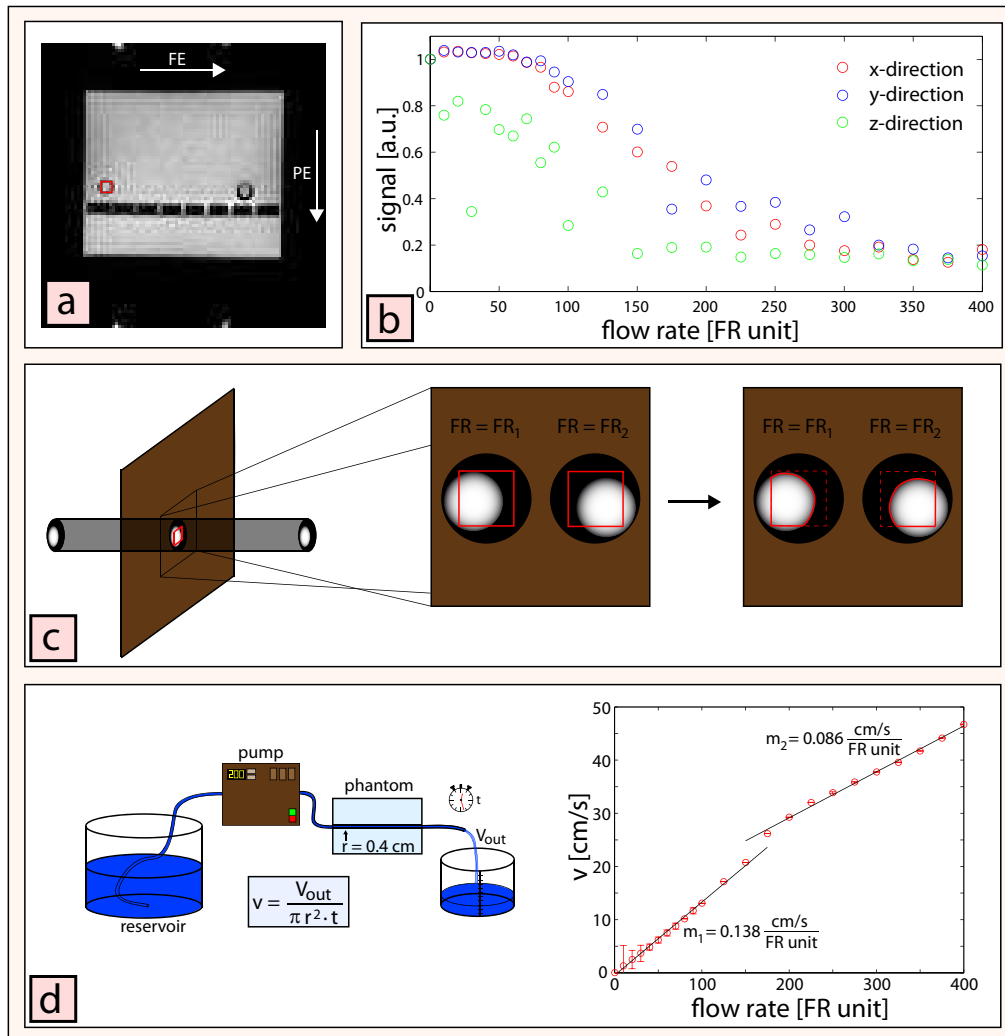


Figure 4.17 Flow phantom experiments. a) Magnitude image of the investigated slice. The red square marks the ROI investigated in this study. b) ROI signal intensity acquired at water flow at different flow rates. The image shows the normalized intensity values of flow encoding in *x*- *y*- and *z*-direction, while the flow direction is aligned with the *z*-axis. c) Data postprocessing. Since it is problematic to use the same ROI in every image, the ROI has to be adjusted to every image, further discussed in the text. d) Sketch of the pump calibration setup and the resulting FR-velocity calibration curve.

Table 4.6 Signal decay due to flow rate increment. The table shows the values for encoding in all three dimensions. The critical velocity was adjusted to 4 cm/s.

flow rate	$S_x/S_{x,0}$	$S_y/S_{y,0}$	$S_z/S_{z,0}$	flow rate	$S_x/S_{x,0}$	$S_y/S_{y,0}$	$S_z/S_{z,0}$
0	1.00	1.00	1.00	150	0.60	0.70	0.16
10	1.03	1.04	0.75	175	0.54	0.35	0.19
20	1.03	1.03	0.82	200	0.37	0.48	0.19
30	1.03	1.03	0.34	225	0.24	0.37	0.15
40	1.03	1.03	0.78	250	0.29	0.38	0.16
50	1.02	1.03	0.70	275	0.20	0.27	0.16
60	1.01	1.02	0.67	300	0.18	0.32	0.15
70	0.99	0.99	0.74	325	0.19	0.20	0.16
80	0.97	0.99	0.55	350	0.14	0.18	0.13
90	0.88	0.95	0.62	375	0.12	0.15	0.14
100	0.86	0.90	0.28	400	0.18	0.15	0.11
125	0.71	0.85	0.43				

4.4.1 Phantom Measurements

In this section, the influence of a single VSM on the signal is investigated. Therefore the imaging sequence was modified by the application of the VSM and subsequent EPI readout. The flow phantom presented in section 3.2.3.3 is used. As already mentioned, the statistical approach can not really be used because of no existing randomized orientated cylinders in this phantom, but the influence of the velocity-selective gradients on linear flow is investigated. The phantom was placed in the scanner in a way in which the flow direction was coinciding with the main magnetic field. The phantom was connected with the pump by long tubes and a cut-off velocity $v_c = 4$ cm/s was adjusted. Then, the signal was acquired for different flow rates FR. A transverse slice was acquired and the ROI was chosen according to Fig. 4.17a. For each flow adjustment, the images with applied encoding gradients in all three directions were acquired. The results for the signal intensities are illustrated in Fig. 4.17b. Here, the values are normalized to the respective image with $FR = 0$. Figure 4.17c shows a sketch of the data post processing. The exact ROI has to be chosen individually for each image, because not all pixels inside the ROI show the same intensity, resulting from laminar and partially turbulent flow. Otherwise pixel with a very low intensity would falsify the qualitative result. For each image all voxels in the ROI with at least one fourth of the maximum signal intensity value of the investigated ROI were used. Figure 4.17b shows the signal intensity for the three dimensions. It can be seen that the signal intensity in the voxel decreases with an increasing FR. As expected, the signal for flow in z -direction and encoding gradients in x - and y -direction is much less attenuated than the signal for encoding in z -direction. Equations 3.54 and 3.65 show the relationship between the input parameters and the critical velocity. Because of the duration of the adiabatic pulses and the hardware limitations (e.g. maximum slew rate), these parameters are not arbitrary. In this work the following fixed values were used: $\Delta = 1.5$ ms, $\delta = 19$ ms. For a VSM with the critical

Table 4.7 Sequence parameters of the VSSL sequence. The gradient strength was chosen to apply a critical flow velocity of 4 cm/s.

Sequence	$\Delta x, \Delta y$ [mm]	d [mm]	BW [Hz/Px]	ΔTE_{eff} [ms]	G [T/cm]	TI [ms]
VSSL	2	5	2367	24	$5.15 \cdot 10^{-5}$	800

velocity $v_c = 1$ cm/s the required gradient strength can be calculated,

$$\begin{aligned}
 G &= \frac{\pi}{2 \cdot \gamma \cdot \delta \cdot \Delta \cdot v_c} \\
 &= \frac{\pi}{2 \cdot 2\pi \cdot 42.58 \cdot 10^6 \frac{\text{Hz}}{\text{T}} \cdot 1.5 \text{ ms} \cdot 19 \text{ ms} \cdot 1 \frac{\text{cm}}{\text{s}}} \\
 &= 2.06 \cdot 10^{-4} \frac{\text{T}}{\text{cm}},
 \end{aligned} \tag{4.5}$$

The factor 2 in the denominator results from the fact that not only one bipolar gradient is applied but rather a pair of bipolar gradients. According to Eq. 4.5 the gradient strength has to be divided by 4, when the critical velocity is increased to 4 cm/s. This results in the field strength² $G = 5.15 \cdot 10^{-5}$ T/cm. To quantify the flow velocity inside the tube, the volume flow was measured. With a tube diameter of 8 mm, the mean flow velocity inside the cylinder could then be calculated. The relationship between FR and flow velocity is presented in Fig. 4.17d. The calibration curve shows two different regimes. The first regime ranges from a FR of 0 to 150 with a slope of 0.138, cm/(s · FR unit). A higher FR shows a different relationship with a slope of only 0.086 cm/(s · FR unit). The v_c value of 4 cm/s applied in the phantom experiment corresponds to a flow rate between 30 and 40. There exist different reasons why the Fig. 4.17b shows still high pixel intensities even when the flow rate is much higher than 40. This will be further discussed in chapter 5.

4.4.2 *in vivo* Measurements

In the next step, the implemented and developed VSSL technique was used for *in vivo* measurements. Since the signal difference between the control image and tag image was very small, a lot of averages were necessary. Due to this and the fact that two images were subtracted from each other, it was very important that the person in the scanner remained still for a long period of time. Here, the results of a measurement with 15 averages is presented. The most important imaging parameters can be seen in Tab. 4.7. Figure 4.18 shows the single one-dimensional flow encoded images of the first echo. It can be seen that the signal of the difference images is very low. Even after combining the three dimensions to determine 3D flow encoding, the signal is not very high. Due to the low SNR in one measurement, it was necessary to repeat the sequence several times. Figure 4.19a shows an example for a venous blood image at the effective echo time $TE_{\text{eff}} = 24$ ms. The corresponding averaged image and the image after application of a Gaussian filter can be seen in Fig. 4.19b and Fig. 4.19c, respectively. To have an anatomic

²It is important to observe that G is not the input parameter for the IDEA software, but rather the gradient moment A , that is the product of G and δ . In our example A is $9.79 \cdot 10^{-7}$ Ts/cm

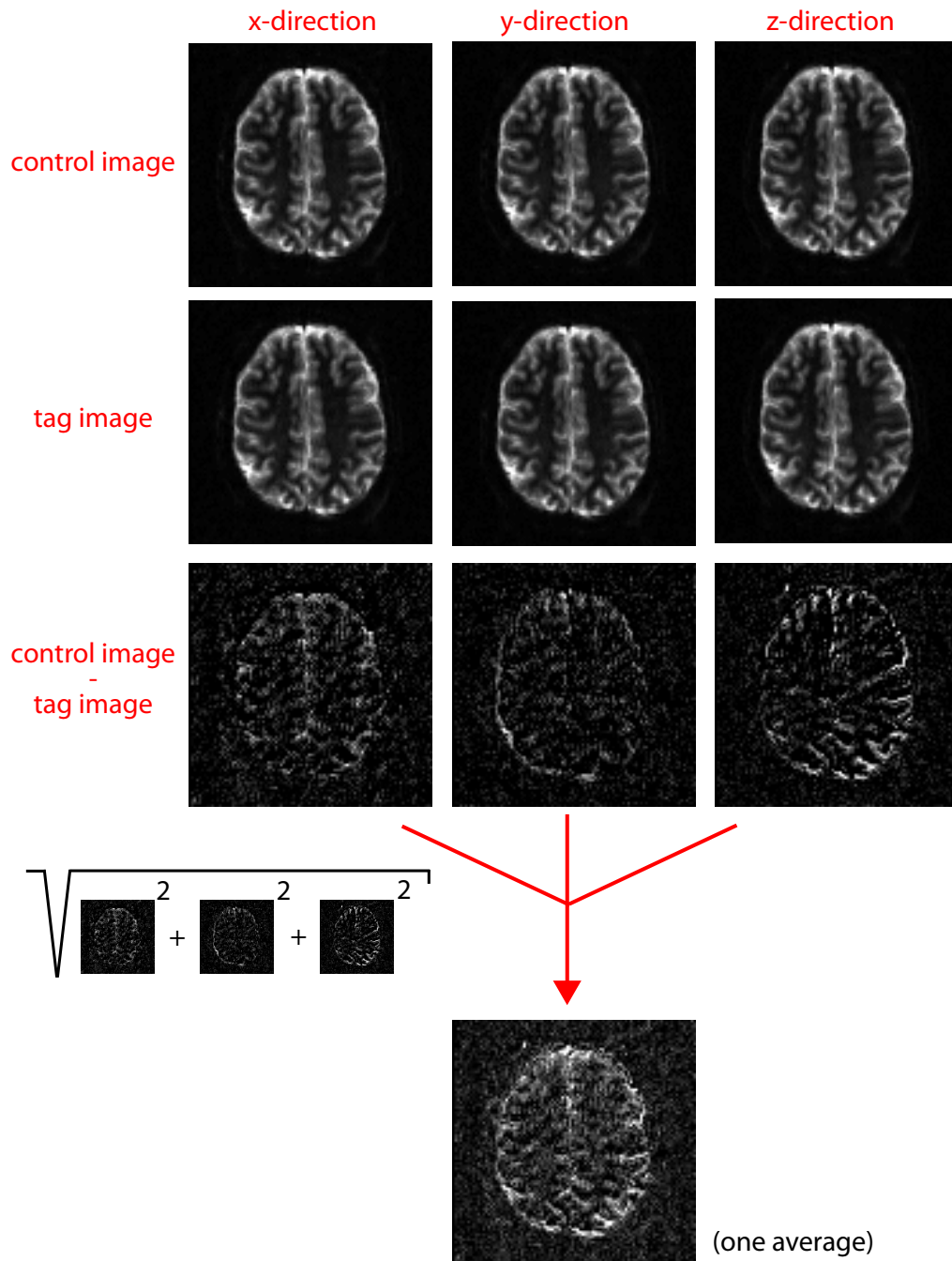


Figure 4.18 VSSL data acquisition. The image shows the different control and tag images of flow encoding in x -, y - and z -direction. Moreover, the difference images are presented. These are combined to the total 3D difference image by quadratic addition.

reference image, a high resolution T_2 -weighted image of the same slice is presented in Fig. 4.19d. The signal decay in each voxel can be exponentially fitted, which yields the relaxation rate of the venous blood. The 5th echo was not taken into account for the data fit, because the signal intensity was too low. Figure 4.19e shows a venous blood image

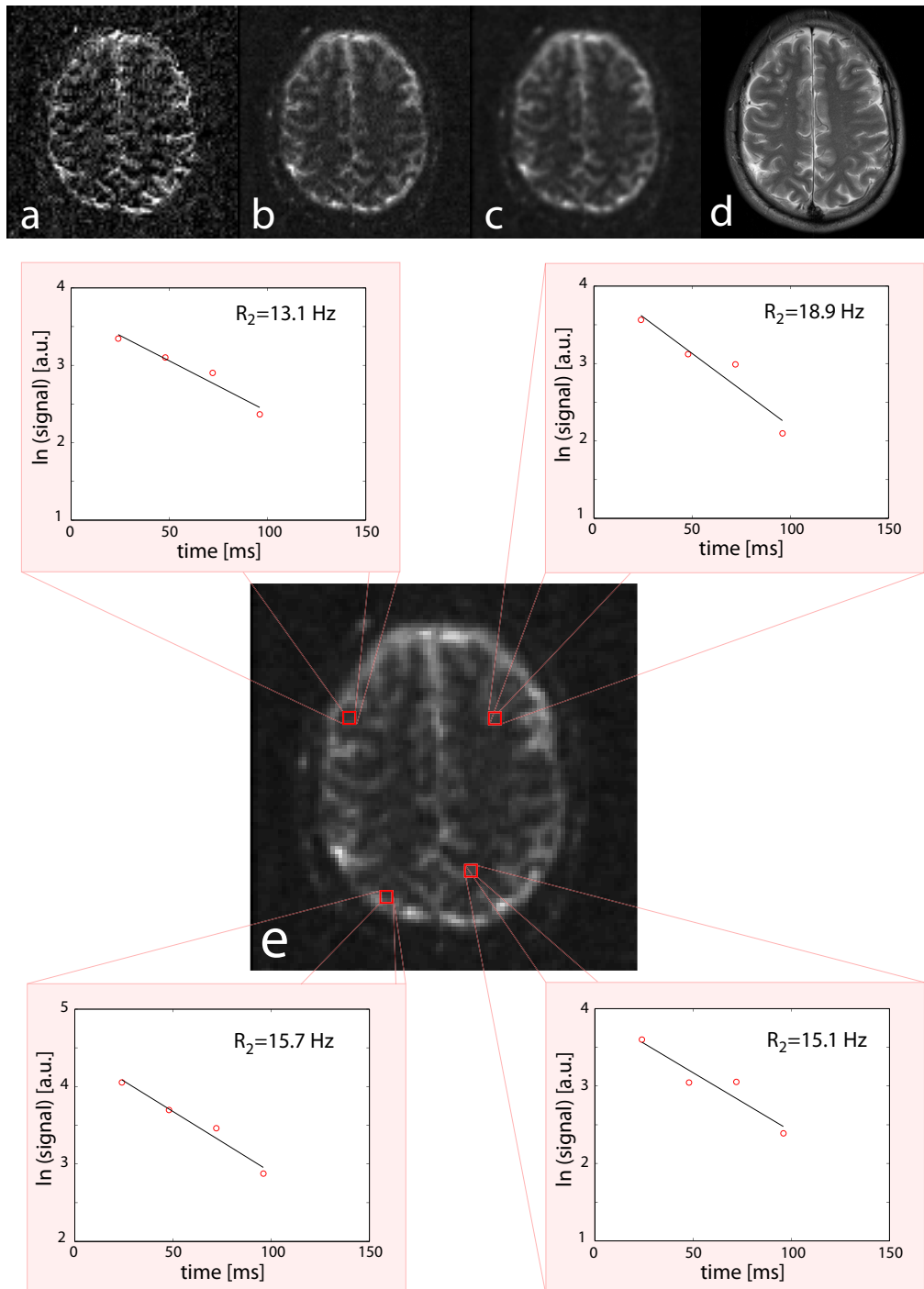


Figure 4.19 VSSL data postprocessing. a) The acquired image at an effective echo time of 24 ms, b) the same image after averaging 15 times and c) Gaussian filtering, d) the anatomical T_2 -weighted reference image.

and the investigated pixels in this study (red squares). Moreover, the four-point fit of each ROI can be seen. The relaxation rates of these ROIs are between 13.1 and 18.9 Hz

resulting in the corresponding relaxation times of 76.3 ms and 52.9 ms, respectively. Using the calibration curve (Eq. 3.73) for a Hct of 0.44 and solving it for the OEF yields

$$\text{OEF}^2 + 0.467 \cdot \text{OEF} = \frac{R_2 - 8.3}{71.9}. \quad (4.6)$$

The OEF values for the chosen data points are then between 11.5 % and 21.5 %. It has to be remarked that Hct is chosen to be 0.44 and, in fact, it can be well below this value resulting in higher OEF values. Moreover, it has to be mentioned that the calibration curve of Zhao et al. [2007] differs from the calibration curve used by Bolar et al. [2009]. The usage of the other calibration curve would result in OEF values between 35 % and 40 %.

4.5 Comparison of the Different Techniques

The quantification of the OEF value depends not only on the measured signal but also on the different models and constants that were used for calculation. In this work, for the analytical methods a hematocrit of 0.4 was used. According to Spees et al. [2001], the susceptibility difference value between fully deoxygenated and fully oxygenated blood was 0.27 ppm. For the TPF-method the corrected average OEF values for white and gray matter were 42.86 % and 43.89 %, respectively. The SQ-method was applied at a tumor patient. Here, OEF values³ of 27.80 % and 37.54 % were calculated for the tumorous region and a healthy region in the white matter, respectively. The application of the TSC-method yielded OEF values of 21.99 % and 26.91 % for white and gray matter, respectively. These values seem to be very high compared to the results from the VSSL-method (values between 11.5 % and 21.5 %), but as already mentioned, the R_2 -Y calibration of the venous blood plays an important role and there exist different calibration curves as further discussed in section 5. Table 4.8 shows an overview of the results of the different methods for OEF determination and the corresponding acquisition times.

³These values have to be interpreted as semi-quantitative, because for the calculation the CBV was used, not only the deoxygenated part of the blood volume, λ .

Table 4.8 Results of the different methods for OEF determination and corresponding acquisition times. The OEF value for GM has not been calculated with the SQ-method due to the high inhomogeneity of the slice, that hampered the choice of a suitable ROI. For the VSSL sequence, the presented values represent the range of the investigated voxels of the whole brain. For comparison, $\text{OEF}_{\text{WM}}/\text{OEF}_{\text{GM}} = (25 - 35)\%/(45 - 50)\%$ can be found in literature [Vaupel et al., 1989]. The large discrepancy in the results of the different techniques is further discussed in chapter 5.

Method	TPF	SQ	TSC	VSSL
OEF_{WM} [%]	42.86 ± 16.29	37.54 ± 4.55	21.99 ± 3.44	(11.5)
OEF_{GM} [%]	43.89 ± 14.44	-	26.91 ± 6.51	(21.5)
TA [min : s]	29 : 26	19 : 01	57 : 02	45 : 00

4.6 SWI of the Kidney

In this section, first results of the SWI technique applied at the kidney are presented [Mie et al., 2010]. The SWI sequence, that was used in this work, was a 3D FLASH sequence with flow compensation in all three dimensions. To have a comparison between abdominal and brain images, at first, SWI brain measurements with well-established

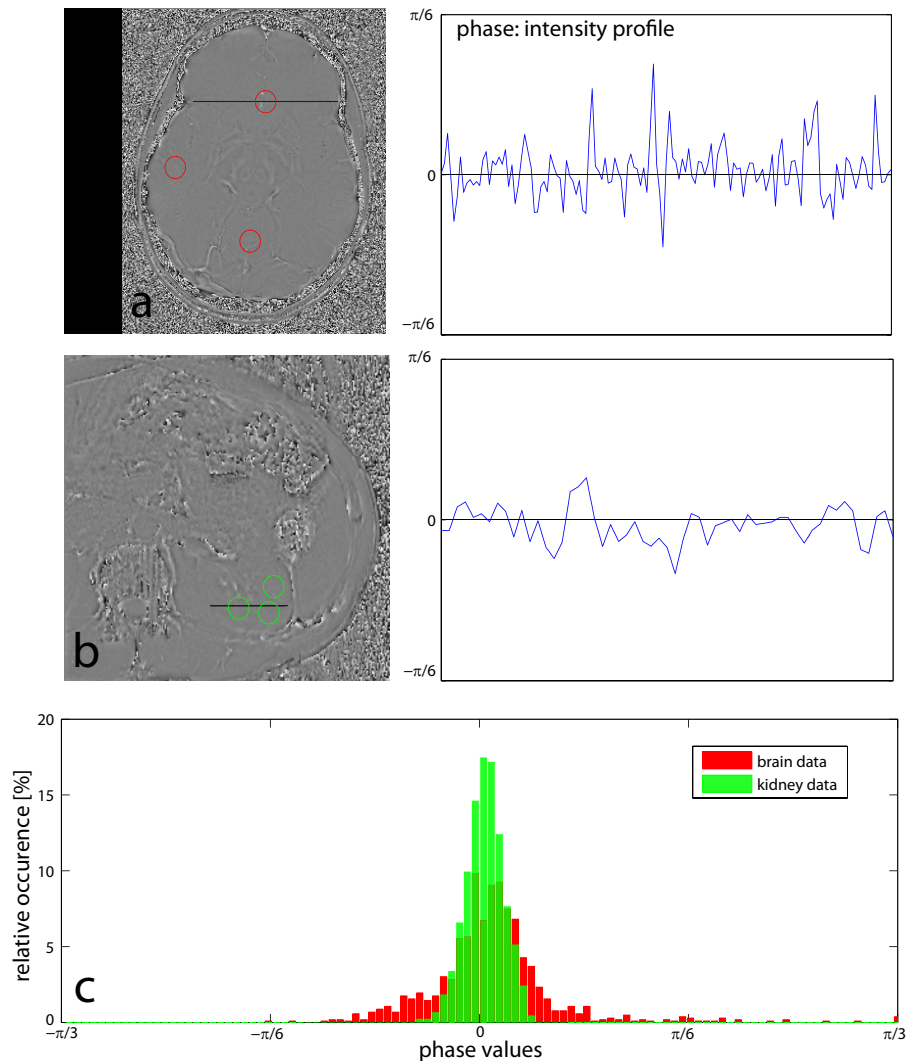


Figure 4.20 Phase images and phase profiles **a)** Filtered phase image of the brain (left). The blue line indicates a profile line. The corresponding phase values along this line can be seen in the plot on the right. One reason for this big phase jump is the large susceptibility variation in the veins due to a high OEF in the brain. **b)** Filtered phase image of the abdomen with a profile line (left). The corresponding phase values are shown on the right. **c)** Relative occurrence of phase values in different ROIs of a) and b). Red phase values represent the brain data, green phase values represent kidney data. Three ROIs were chosen to get phase values from different regions of the respective organ. Both phase images are shown as reconstructed by the scanner.

parameters were performed ($TE/TR/FA = 20\text{ ms}/28\text{ ms}/15^\circ$, slice thickness = 1.5 mm, FOV = $162.5 \times 200\text{ mm}^2$, matrix size = 260×320 , BW = 120 Hz/Px, slices per slab = 56, slice oversampling = 28.6%). The total acquisition time was approximately 9 minutes. To transfer this imaging protocol to the abdomen, several parameters had to be adapted in order to allow for breath-hold acquisition. Scan time reduction was achieved by parallel imaging (generalized autocalibrating partially parallel acquisition (GRAPPA), acceleration factor 2, 24 reference lines) and partial Fourier-imaging (6/8) in phase and in slice direction. In addition, the FOV was kept as small as possible covering only one kidney to shorten the acquisition time even more, while infolding artifacts were avoided. All other imaging parameters, in particular TE and FA as explained in the following, were the same as in the brain protocol.

In the literature, the T_1 relaxation time of kidneys is reported to be 1412 ms in the medulla [de Bazelaire et al., 2004] and 945 – 966 ms in the cortex [O'Connor et al., 2007]. Based on calculation of the Ernst angle [Haacke et al., 1999], the optimal flip angle of $12^\circ - 17^\circ$ was respected by selecting 15° .

In a recent study on brain imaging, Haacke et al. [2009] recommended a TE of at least 20 ms. To obtain an optimal contrast for veins at 1.5 T, a TE of 40 – 80 ms is needed. So, if the field strength increases from 1.5 T to 3 T and the phase effect shall remain the same (constant $\Delta\varphi$), the echo time has to be halved. Therefore, the minimum TE at 3 T becomes 20 ms. In summary, the abdominal SWI protocol comprises the following parameters: $TE/TR/FA = 20\text{ ms}/28\text{ ms}/15^\circ$, slice thickness = 1.8 mm, FOV = $220 \times 220\text{ mm}^2$, matrix size = 256×256 , BW = 120 Hz/Px, slices per slab = 52, phase resolution = 75%, slice resolution = 75%, TA = 67 s. All examinations were acquired in breath-hold. Seven healthy volunteers (3 female / 4 male, range: 25 – 32 yrs., mean age 27 yrs.), who were able to hold their breath at least for 67 s, were included in this pilot study. The subjects were positioned supine head first.

It was very difficult to acquire images without motion artifacts because of the still quite long acquisition time of 67 s. To demonstrate the potential of renal SWI, images from the volunteer with the best breath-holding capacity are shown. Since SWI relies on the phase information, the phase images were investigated in detail. Comparing brain and kidney phase images by taking an arbitrary profile through the respective area showed that there are larger phase changes in the brain (Fig. 4.20a) than in the kidney (Fig. 4.20b). In the latter, hardly any phase changes were observed. The corresponding abdominal magnitude image and the resulting susceptibility weighted image are shown in Figs. 4.21a and 4.21b. The abdominal susceptibility weighted images created with the standard (brain) phase mask (Eq. 2.96) showed only poor vessel contrast, i.e. hardly any obvious and visually detectable contrast enhancement was observed. The susceptibility weighted image created with the new phase mask (Eq. 2.98) showed some areas with venous structures (see arrows, Fig. 4.21d).

4.6.1 Contrast-to-Noise Ratio (CNR) Calculation

To evaluate the contrast enhancement by the modified phase mask, the CNR was calculated in carefully selected regions-of-interest (ROIs). Depending on the size of the ROI, the CNR varies. ROIs were placed inside a vessel by avoiding selection of surrounding tissue. Figure 4.21f depicts the location of the ROIs for SNR and CNR calculation in one subject. The yellow ROI surrounds a vessel, the blue ROI surrounds tissue. ROIs were

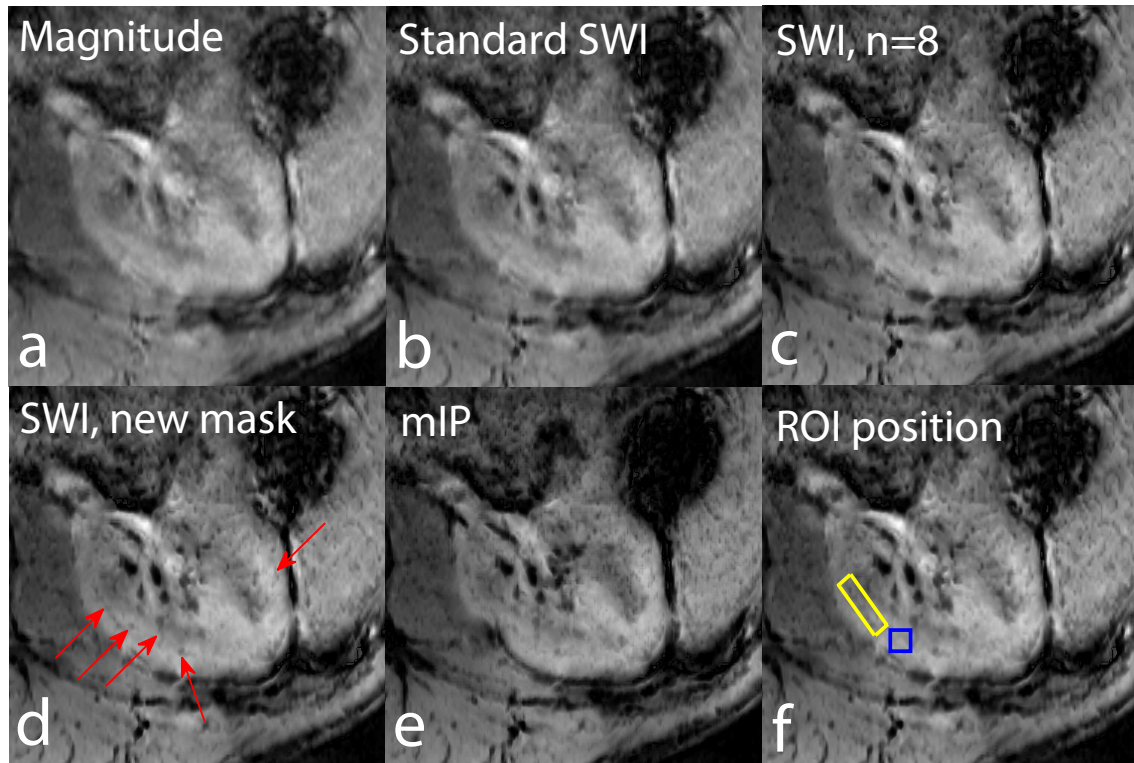


Figure 4.21 SWI postprocessing. a) Magnitude image and b) corresponding susceptibility weighted image reconstructed with standard phase mask using $n = 4$, c) $n = 8$ and d) modified phase mask with $n = 4$. The red arrows mark the spots where venous structures can be seen. e) Minimum intensity projection (mIP) of 3 slices. f) Localization of the ROIs for CNR and SNR calculation. The yellow ROI surrounds a vessel, the blue ROI surrounds tissue. Latter is also used to calculate the SNR.

placed accordingly in the six other data sets.

Table 4.9 summarizes the results of the evaluation of contrast enhancement of all measurements. For all seven exams, an increment in CNR could be obtained by the new phase mask. On average, CNR was increased by a factor of 1.33. SNR calculation yielded an average value of 94.8 and a standard deviation of 40.9. The CNR in SWI images created with either the new phase mask (Fig. 4.21d) or the standard phase mask but with eight multiplications (Fig. 4.21c) was approximately the same, which is not surprising due to the similar shape of the phase masks (Fig. 2.22). Nevertheless, in the susceptibility weighted images obtained with the new phase mask, a differentiation between renal medulla and cortex was possible. Furthermore, small black lines, enhanced by the phase mask, were reviewed by experienced radiologists and could be identified as small renal veins (see arrows, Fig. 4.21d). Since a 3D volume is acquired by the implemented sequence, a minimum intensity projection (mIP) of 3 slices was realized (Fig. 4.21e). Therewith, the already detected structures of Fig. 4.21d were enhanced.

Table 4.9 SNR and CNR of the kidney measurements: $\text{CNR}_{\text{original}}$ was calculated with the standard SWI approach (Eq. 2.96), CNR_{new} was calculated with the new phase mask (Eq. 2.98). ΔCNR is the percentage improvement of CNR. The average ΔCNR is 33.4% with a standard deviation of 17.4%. Absolute CNR values depend strongly on the choice of the ROI. The average SNR is 94.8 with a standard deviation of 40.9.

Measurement	1	2	3	4	5	6	7
SNR	85.4	71.3	139.7	148.3	56.9	44.1	118.5
$\text{CNR}_{\text{original}}$	22.5	14.7	17.2	63.2	8.3	7.3	15.3
CNR_{new}	26.7	18.0	21.4	76.8	10.8	11.6	24.1
ΔCNR [%]	18.7	22.4	24.4	21.5	30.1	58.9	57.6

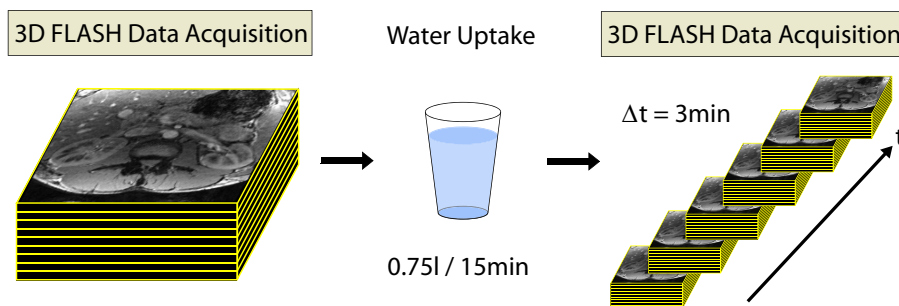


Figure 4.22 Experimental setup for kidney SWI under oxygenation variation. The experiment consists of multiple 3D FLASH acquisitions, one before and six after 15 minutes water uptake. The time interval between the post-water-uptake measurements was 3 minutes.

4.7 Kidney SWI under Oxygenation Variation

Since SWI is based on the usage of blood as an intrinsic marker of blood oxygenation, it is very interesting to investigate the effect of an induced increase of blood flow resulting in a higher blood oxygenation level dependent (BOLD) contrast. In this study, the higher kidney function and the accompanying higher blood flow are realized by water uptake. Images were acquired before and after water uptake in constant time intervals. A quantitative comparison of the state before and after water uptake is possible by CNR calculation. The used imaging sequence was a T_2^* -weighted 3D FLASH. To reduce scan time to allow for breath-hold acquisition, parallel imaging (GRAPPA acceleration factor 3, reference lines: 24) and phase and slice partial Fourier (6/8) were applied. The other imaging parameters were chosen similar to the kidney imaging parameters of section 4.6: $TE/TR/FA = 20\text{ ms}/28\text{ ms}/15^\circ$, matrix size = 256×256 , FOV = $231 \times 231\text{ mm}^2$, slice thickness = 1.8 mm, BW = 120 Hz/Px, slices per slab = 24, TA = 28 s. These measurements were performed on a 3 T Siemens Magnetom Skyra (Siemens, Erlangen, Germany) using a 18 channel phased-array body coil. For data processing, the modified phase mask (Eq. 2.98) and a multiplication factor $m = 4$ was applied. A pixel-wise analysis is not possible because of the difficulties of renal imaging due to respiratory and bulk movement. Nevertheless, this problem can be solved by choosing a distinct vein in the kidney and

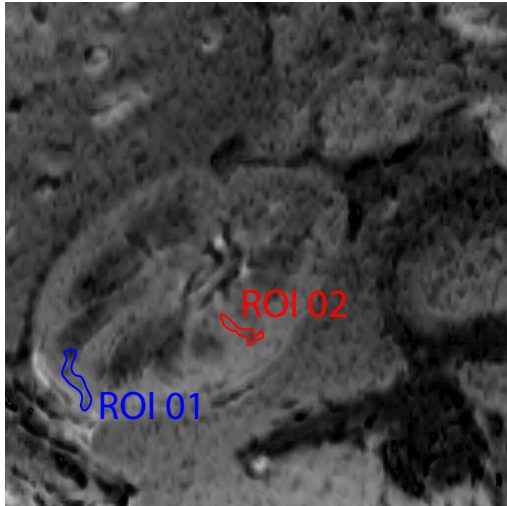


Figure 4.23 Location of the ROIs for CNR calculation during oxygenation variation. Two veins located at different locations in the kidney were chosen for the investigation of CNR variation.

investigate the variation of time of the signal contrast between this vein and the kidney cortex over the time. Figure 4.22 shows a sketch of the experimental setup.

The technique developed in section 4.6 was used to investigate the SWI contrast under the influence of oxygenation variation. To investigate the SWI contrast, two different veins were chosen and the CNR between these veins and the surrounding tissue was calculated. Figure 4.23 shows the location of the ROIs of the investigated veins. The results of the two different ROIs of a volunteer measurement are presented in Fig. 4.24 and Tab. 4.10. It can be observed, that for both ROIs the susceptibility weighted contrast first decreases, and then increases again. This effect can be visualized by kidney SWI post processing [Mie et al., 2010].

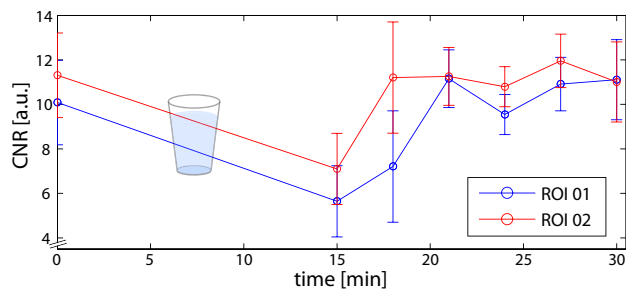


Figure 4.24 CNR variation in time. During water uptake the CNR decreases, and then increases again. The absolute CNR value depends strongly on the choice of the ROIs.

t [min]	CNR_{01}	CNR_{02}
0	10.1 ± 1.9	11.3 ± 1.4
15	5.6 ± 1.6	7.2 ± 2.6
18	7.2 ± 2.5	11.2 ± 2.0
21	11.2 ± 1.3	11.3 ± 2.1
24	9.6 ± 0.9	10.8 ± 1.0
27	10.9 ± 1.2	12.0 ± 1.9
30	11.1 ± 1.8	11.0 ± 2.2

Table 4.10 CNR values of the two different ROIS.

4.8 OEF and SWI

The SWI technique enables the possibility to highlight venous structures in human tissue. As can be seen in section 4.7, the SWI contrast changes if the oxygenation changes. This has already been shown by Sedlacik et al. [2008], where caffeine intake was used to change

the oxygenation in the brain. OEF determination with the mentioned analytical methods is hardly possible at the kidney because these methods are very sensitive to motion and therefore not applicable at the abdomen. Even a triggered acquisition method would not make this technique performable because of the pixel-wise postprocessing and the even longer acquisition time. Nevertheless, SWI was successfully applied at the kidney and oxygen variation by water uptake was qualitatively observed. Therefore, this method shows promising results for further qualitative oxygenation determination.

5 Discussion

In this work, the influence of blood oxygenation on the MR signal was investigated. Different approaches were used to make quantitative or qualitative statements about the oxygen supply of the tissue.

The first and largest part of this work deals with analytical methods to calculate the parameters deoxygenated blood volume and oxygenation level using different methods. The second part shows the implementation of a new approach for OEF determination based on the separation of the venous blood signal from the background signal components [Bolar et al., 2009]. The third part describes the implementation of the SWI technique at the kidneys.

5.1 Analytical Methods for OEF Calculation

5.1.1 Magnetic Field Inhomogeneities

The presented quantification methods are based on an established tissue model [Yablonskiy and Haacke, 1994]. The MR signal is acquired with a sequence sensitive to susceptibility differences. Therefore, other susceptibility changes than the blood susceptibility change due to oxygen delivery also cause unwanted T_2^* decay and falsify parameter calculation. One reason for these magnetic field inhomogeneities are air-tissue interfaces as can be found in the frontal sinus, paranasal sinus or in the region of the nasopharyngeal zone. Another source of magnetic field inhomogeneities are bone-tissue interfaces as can be found in cranial regions. These inhomogeneities can be assumed as a linear magnetic field gradient across each voxel, because the range of these inhomogeneities is much larger than the voxel dimensions. This field gradient leads to an additional signal decay due to a rectangular frequency distribution within each voxel. Fourier analysis yields a sinc-shaped signal decay as a result from these inhomogeneities which may lead to a falsification of the fitted parameters λ , R_2 and R_2' and finally of the OEF values. The knowledge about the sources of magnetic field inhomogeneities may help to identify a slice position in the brain with a homogeneous field distribution. Positioning the slice in areas far away from the mentioned regions is possible for volunteer studies but not for all patient measurements. If a tumorous region shall be investigated close to the frontal sinus, it is not possible to choose a slice with a homogeneous field profile.

Another option to reduce the inhomogeneity effect would be to decrease the slice thickness. Unfortunately, the acquisition of a thinner slice results in less signal and, therefore, requires more averages to achieve the same SNR. To avoid the influence of most of the inhomogeneities, a very accurate shim of the investigated slice is essential. Moreover, a too long shimming time has to be avoided due to the long duration of the measurements presented in this work resulting in a trade-off between shim accuracy and a short shimming time.

Jeppard and Balaban [1995] and Irarrazabal et al. [1996] presented a technique allowing

the calculation of field gradient maps by the acquisition of highly resolved phase maps. Solin [2009] showed that this technique can be used to obtain good results in phantoms. In this study, this technique was applied for *in vivo* data.

5.1.2 TPF-Method

Although the *in vivo* results calculated with the TPF-method look very promising, this technique suffers from some limitations. First, only the signal at the spin echo and in the long-term regime is investigated and used for further parameter calculation. The high signal intensity values of the short-term regime can not be used with this technique, because the signal equation does not describe the signal decay in this time regime. The extrapolation of the data is very SNR sensitive. Due to the limited available acquisition time a too low SNR could lead to a falsification of the calculation of the deoxygenated blood volume λ , which is obtained from the difference of the logarithmical values of the fit curve and the signal intensity at the spin echo. If the R'_2 value is determined correctly and λ is underestimated, a huge overestimation of $\Delta\chi$ and OEF values is possible, because the susceptibility difference between blood and tissue in one voxel depends linearly on the quotient of R'_2 and λ . In analogy to this, an overestimation of λ may lead to an underestimation of the OEF value assuming a correctly determined R'_2 value.

The problem of the simultaneous determination of λ and $\Delta\chi$ is the requirement of a very high SNR. Solin [2009] showed with simulations that a reliable determination of λ and $\Delta\chi$ is only possible if the SNR is very high: A SNR of 600 is necessary to keep the single parameter error below 10%. However, if one parameter is known, a SNR of 100-200 is sufficient to determine the other parameter reliably. Therefore, the main focus of this work was to find a solution for this problem, e.g. a method for a separate parameter estimation. This was realized by the developed SQ- and TSC-method.

5.1.3 SQ-Method

The SQ-method is an interesting approach to reduce the number of fit parameters of the signal equation. DSC measurements are used in clinical routine to determine reliable maps of mean transit time, time to peak, blood flow and blood volume. Although the perfusion postprocessing yields good results, an error might occur by an inappropriate choice of the AIF. As the location of a large artery is not always clearly identifiable due to the potentially limited resolution of the images, partial volume effects might occur resulting in a falsification of the quantitative output parameters. However, the postprocessing of the data usually yields reliable results (measured value: $CBV_{WM} = (4.87 \pm 1.17) \%$, literature value: $CBV_{WM} = (3.8 \pm 1.0) \%$ [Tofts, 2003]). Nevertheless, this technique is limited to certain slices where a large arterial vessel is located. For many investigations of tumor patients a contrast agent injection is administered and, therefore, this technique could be added to clinically routine without much effort. However, the total acquisition time is limited to keep the investigation time of the patients as short as possible. The application of the developed technique takes also a long time. The applied sequences should usually not exceed an additional acquisition time of 30 minutes. The parameters have to be modified to enable an acquisition in the given time interval, because this includes shimming time, field mapping, GESSE sequence and DSC measurement. The number of averages of the GESSE sequence usually has to be reduced resulting in a lower

SNR.

The SQ-method presents a possibility to turn the three-parameter fit of the TPF-method into a two-parameter fit and to determine the blood volume with an independent sequence. However, this method can not be used to give a quantitative value for the tissue oxygenation due to the substitution of λ by CBV. Nevertheless, a qualitative comparison between healthy and tumorous regions, as shown in this work, is possible. The results show a significant relative difference of the CBV and the OEF in the investigated regions. However, an independent technique to determine the deoxygenated blood volume, λ , would be desirable. An approach for such a technique is the TSC-method.

5.1.4 TSC-Method

This work presents a new approach, that reduces the fit parameters of the GESSE data. A method was developed, that determines the three free parameters of the signal equation, R_2 , R'_2 and λ , independently. For R_2 determination a CPMG sequence was used, that applies several spin echoes after the 90° excitation pulse. After each 180° pulse the same line in k-space is sampled, resulting in different contrasts at different echo times. The T_2 -weighted data enabled a R_2 fit. In analogy to this, a MMGE sequence was used, that acquires the same line in k-space at different echo times resulting in T_2^* -weighted gradient echo images. After the application of a R_2^* fit, these two datasets could be used to calculate the maps of the reversible relaxation rate R'_2 , that reflects - after macroscopic inhomogeneity correction - the local oxygenation status. When the R_2 and the R'_2 maps are known, these data can be used as input parameters to fit the signal equation. The relaxation rates determine the slopes of the fit curve before and after the spin echo, while the value of λ is determined by the fit curve value and the signal intensity at the spin echo. The remaining fit of the GESSE data consists only of a vertical movement of the fit curve determined by the relaxation rates. However, first *in vivo* experiments showed a disagreement of the data points and the fit curve. As the slope of the fit curve after the spin echo showed a slight underestimation compared to the slope of the GESSE data it was concluded that the T_2^* -weighted data of the MMGE sequence slightly underestimates the R_2^* value calculated from the GESSE dataset. The curve fit prior to the spin echo reveals that the main error has its origin in the R_2 calculation. By fitting the data points before the spin echo and the signal decay after the spin echo, R_2 maps were calculated. In this work, the R_2^* maps of the GESSE and the MMGE dataset as well as the R_2 maps from the GESSE and the CPMG dataset were evaluated in a phantom experiment. Therefore, several tubes filled with different contrast agent solutions were used. The mentioned sequences were applied to calculate the R_2 and R_2^* maps. Compared to the results of the GESSE sequence, for all ROIs in the tubes, a systematical underestimation of R_2 and R_2^* calculated with the separate sequences (CPMG and MMGE) was found. For further analysis the tubes with a relaxation time similar to white and gray matter were investigated. The average underestimation of the resulting four tubes amounted to 4.65 % for the R_2^* and 20.70 % for the R_2 calculation.

In this work, the results of two different techniques were compared and it was explained that one technique underestimates the results compared to the other technique. In this case, it is more probably that the relaxation rates calculated from the GESSE data are overestimated, which may result from many gradient echoes prior to the spin echo. These applied gradients cause a diffusion weighting that hampers the relaxation rate

calculation. The resulting percentage overestimation of the relaxation rates of the GESSE sequence are 4.44 % and 17.15 % for R_2^* and R_2 , respectively. Since the resulting effect of a sequence correction is based on the adjustment of the different methods, it is not important for the calculation whether one measurement underestimates a certain value or the other sequence overestimates the respective value. In principle, these correction values are relative values, that can be used to "adjust" different sequences. As a next step a validation of the CPMG sequence would be interesting. A source for possible errors even for this well-established technique can be imperfect 180° pulses. This problem might be solved by the application of a so-called Carr-Purcell/Carr-Purcell-Meiboom-Gill (CP/CPMG) sequence [Schad et al., 1989], that applies 180° pulses with different flip directions, resulting in a compensation of the imperfect pulse angles.

In the following calculations, the MMGE and the CPMG sequence were "adjusted" to the GESSE data, by a relative correction of the local R_2 and R_2^* values. This correction was tested in another phantom study. Here, the brain tissue was simulated by long strings coiled in water solutions doped with contrast agent. In this experiment, two different venous blood volume fractions were simulated by two different phantoms. Unfortunately, it is hard to realize a perfectly randomized coiled string network phantom, but the size of the investigated voxel ($2 \times 2 \times 6 \text{ mm}^3$) compared to the vessel diameter ($93 \mu\text{m}$) allows for the assumption that most of the local inhomogeneities average out. It could be shown that even if the R_2 values were lower (5-7 Hz) than the R_2 values of gray (10.10 Hz) and white (14.49 Hz) matter [Stanisz et al., 2005], the correction method worked very reliably. Even in regions of the phantom where the reversible relaxation rate R_2' exceeds the local R_2 value this correction method yields good results. This was tested by comparing the corrected fit curve with the acquired GESSE data.

After this correction method had been validated, it was applied to *in vivo* data. The results showed a much better fit resulting in more reliable parameters.

Another hint for the overestimation of R_2 by the GESSE sequence were the absolute values. Before correction, the T_2 values of white and gray matter were about 69.4 ms and 78.2 ms, respectively, which is in consistence to values found in literature. After correction the values become 57.5 ms and 64.8 ms, respectively. These calculated values are underestimated compared to the literature values. Nevertheless, these values can be used for further oxygenation calibration, because the tissue model can be described by the signal equation. This is the reason why the GESSE data showed a good agreement with the data fit described by the corrected relaxation times. These values could be used to calculate λ and the OEF. The corrected average values for the OEF are 22.0 % and 26.9 % for white and gray matter, respectively. These values seem to underestimate literature values of (25 – 35) % for white matter and (45 – 50) % for gray matter [Vaupel et al., 1989]. Especially the determination of the latter might be hampered by the choice of the ROI and the influence of partial volume effects. These effects occur in the inhomogeneous regions of gray matter and are caused by the acquisition of fine structure with a low image resolution ($2 \times 2 \times 6 \text{ mm}^3$). Here, different compartments that give a contribution to the signal intensity of the investigated voxel can be found, e.g. cerebrospinal fluid (CSF) and white matter. Other reasons for the discrepancy in oxygenation evaluation are described in the following section.

5.1.5 Oxygenation Quantification

When comparing OEF values of the brain in the literature, a large discrepancy between these values in different studies can be found: $\text{OEF}_{\text{WM}}/\text{OEF}_{\text{GM}} = 33.1\%/32.9\%$ [He and Yablonskiy, 2007], $\text{OEF}_{\text{WM}}/\text{OEF}_{\text{GM}} = (25 - 35)\%/(45 - 50)\%$ [Vaupel et al., 1989], $\text{OEF}_{\text{GM}} = 38\%$ [Lu and van Zijl, 2005], $\text{OEF}_{\text{global}} = (30 \pm 6)\%$ [Oja et al., 1999].

The OEF depends on the average susceptibility difference between the venous vessels and the tissue in the investigated voxel, the hematocrit value and the susceptibility difference $\Delta\chi_{\text{do}}$ of fully deoxygenated and fully oxygenated blood. One reason for the discrepancy between values of different studies is the Hct value, that differs from study to study. The main reason for the discrepancy of OEF values in the literature is a different $\Delta\chi_{\text{do}}$ value. To date, there exist two established studies on the quantification of this value. Weisskoff and Kiihne [1992] calculated a value of 0.18 ppm, while Spees et al. [2001] calculated a higher value of 0.27 ppm. The absence of a general reference value of $\Delta\chi_{\text{do}}$ makes a comparison of OEF values of different studies difficult, because this requires the exact description of the calculation technique and the used constants. Haacke et al. [1995] found an OEF value of 46% in small veins in the brain assuming values of $\text{Hct} = 0.4$ and $\Delta\chi_{\text{do}} = 0.18$ ppm.

In this work, a Hct value for small vessels of 0.34 was used [Eichling et al., 1975], and $\Delta\chi_{\text{do}}$ of 0.27 ppm given by Spees et al. [2001] was used. Exchanging the $\Delta\chi_{\text{do}}$ value by the value found by Weisskoff and Kiihne [1992] yields OEF values of 33% and 40.4% for white and gray matter, respectively. The value found by Haacke et al. [1995] was measured in veins, where different OEF values than in the tissue are expected. This effect can be explained by taking the structure of the vascular tree into account. The oxygen exchange happens in the capillary bed of the tissue. In contrast to a voxel that is completely covered by a large vein, a voxel that is covered by brain tissue consists of many small vessels with different oxygenation states. Therefore, the oxygenation state in this area can be assumed as an average over different oxygenation states. This results in a higher oxygenation in tissue than in veins, resulting in a lower OEF value as it was found in this study.

5.2 Venous Blood Isolation Method

With the QUIXOTIC technique [Bolar et al., 2009] implemented in this work some interesting initial results could be obtained, but the interpretation of these results has to be done carefully. The phantom experiment that is presented in this work can not be used for a direct translation of the results to a capillary network like the brain. The theoretical model behind this technique assumes statistically distributed and randomly orientated cylinders. The phantom enables one-dimensional flow inside of one tube. Nevertheless, the influence of a VSM on this flow was studied and the measured signal showed a similar behavior as the predicted behavior by a capillary network. The images with the VSM in flow direction showed a more rapid signal decay than those with the VSM in the other two dimensions. The experiment showed that the flow encoding gradients in the other dimensions does not affect the signal until a certain flow rate. The flow rate was another problem in this experiment as especially at lower flow rates pulsating flow occurred. For higher flow rates this behavior was not visible, but it was assumed that the flow at high flow rates was not continuous, too. Although this pulsating flow behavior

might be realistic for blood vessels, it hampers the interpretation of the results, because the vessel model assumed continuous flow. These problems confirm the statement that a quantitative analysis is hardly realizable with this experimental setup. The problem of the pulsating flow could be solved by the application of gravity-based continuous water flow caused by different water reservoirs. Although the presented phantom experiment comes along with several problems, a qualitative interpretation of the results is possible. The flow in the phantom is affected by the encoding gradients if they are switched in encoding direction. This causes an attenuation of the signal resulting from the spins in the tube.

For *in vivo* experiments other problems occur. The most obvious difficulty is the fact that in this method different images are subtracted from each other, combined and averaged. Therefore, patient movement would result in huge errors. To deal with this problem, the head of the patient was fixed in the coil. Nevertheless, a slight movement of the head could not be excluded. The errors were most prominent at the boundary of the brain. Another source for errors is the imperfect non-selective refocusing pulse between VSM1 and VSM2. For imperfect pulses, the signal of the blood with a flow velocity larger than v_c is not perfectly nulled, so that subtraction errors might appear. The calculated OEF for the investigated regions amounted to 11.5 – 21.5 %. These values seem to underestimate the results of the other techniques, e.g. $\text{OEF}_{\text{global}} = (30 \pm 6) \%$ [Oja et al., 1999]. This might result from the mentioned instability of this method or from the fact that more averages seem to be necessary. Another possibility to reduce the head motion during the measurement is a head stabilisation as can be seen in stereotactic surgery. Moreover, the application of motion correction algorithms could improve the image postprocessing.

However, the theory behind this technique shows an interesting approach to isolate the signal from the venous part of the blood from the rest of the signal. Bolar et al. [2009] showed *in vivo* results, where an OEF value of 39.1 % was calculated for gray matter. As the calibration curve depends on many factors, it is problematic to use the same calibration curve for different experiments. The T_2 value of blood depends on biophysiological parameters related to susceptibility difference between erythrocytes and plasma, relaxation times of erythrocytes and plasma and the time span between the adiabatic 180° pulses in the VSM2. While the OEF values in this work were calculated from the calibration curve of Zhao et al. [2007], the calibration curve used by Bolar et al. [2009] would lead to reliable OEF values between 35 % and 40 %. This technique shows a completely different method to calculate the OEF value in the brain compared to the techniques presented before. Even if a quantitative statement is difficult due to the discrepancy of the calibration curves, the QUIXOTIC technique shows very promising *in vivo* results.

5.3 SWI of the Kidney

As SWI is sensitive to motion, one of the main challenges of SWI in abdominal organs is the presence of motion, which has to be addressed to obtain reliable results. Not only respiratory motion, but also motion due to peristaltic and air-filled bowel loops lead to artifacts. The original SWI sequence used in the brain takes up to 9 minutes, a too long duration for breath-hold acquisitions.

In this approach, the acquisition time was substantially shortened by a reduction of the image resolution. Furthermore, parallel imaging and partial Fourier techniques were ap-

plied for further acceleration. By applying these techniques, the scan time could be reduced, but SNR was reduced as well leading to pronounced image artifacts. Such artifacts may hamper the quality of SWI data. The resulting acquisition time of 67s was acceptable for healthy volunteers, so that a feasibility study of SWI in the kidneys was possible. Nevertheless, the acquisition time has to be further reduced in order to allow for breath-hold examinations in patients. Therefore, a 2D SWI sequence could be used. However, compared to a 3D sequence a 2D sequence yields lower SNR and suffers from a imperfect slice profile which may reduce the quality of the resulting images. Furthermore, several slices have to be acquired to cover the whole kidney and to create mIPs. These images should be acquired in the same phase of the respiratory cycle to be able to reconstruct a 3D volume from the data. A solution for this problem might be the application of navigator or respiration-triggered techniques [Attenberger et al., 2010]. Alternatively, radial readout techniques, that are less susceptible to motion, could be used. This would reduce motion artifacts in images at longer scan times.

An essential difference between the cerebrum and the kidney is the different oxygen level. The kidney has a much smaller OEF (8 – 10 %) than the brain (white matter: 25 – 35 %, gray matter: 45 – 50 %) [Vaupel et al., 1989]. Therefore, the concentration of deoxygenated blood in renal venous blood is lower compared to cerebral venous blood. This leads to a smaller effect in SWI. In this work, it was shown that either the increase of the number of phase mask multiplications or the optimization of the phase mask could partly compensate for this effect resulting in an increase of the CNR.

It is difficult to identify the most suitable phase mask. In this work, the commonly used linear phase mask was compared to a new one with a different slope. In the future, other possible phase masks, such as exponential, sigmoidal, or asymmetric triangular [Brainovich et al., 2009] could be used as well. As the phase values are very close to zero a threshold was introduced. Although big vessels could be illustrated even without a threshold value, noise could also cause a contrast, which does not originate from susceptibility differences. Therefore, this unwanted contrast was empirically removed by iterative increment of the threshold value.

In brain imaging, the number of multiplications $n = 4$ showed the best results with respect to CNR [Haacke et al., 2004]. A higher number of multiplications ($n = 8$) enhanced the image contrast and vessel-like structures were highlighted. However, a high multiplication number results in the enhancement of susceptibility artifacts other than the desired "BOLD artifact". These unwanted artifacts might result from air-tissue interfaces or noise. A similar contrast to the mentioned mask with $n = 8$ could be obtained using the modified phase mask and $n = 4$. It is important to mention that the choice of the ROIs, which are used for CNR calculation, has a strong influence on the absolute CNR value and explains the variation of CNR for the different examinations (cf. Tab. 4.9). However, CNR analysis showed that within the kidney structures a CNR increase by a factor of 1.33 was achieved on average. Further improvement might lead to an application of this technique in clinical routine, e.g. to diagnose diseases leading to an impaired function of the kidney or acute and chronic rejection after renal transplantation [Michaely et al., 2008].

5.3.1 Kidney SWI under Oxygenation Variation

First results of abdominal SWI were very promising. The observable effect of kidney oxygen consumption could be measured by SWI analysis. In contrast to experiments where the blood flow is reduced and the SWI contrast was increased [Sedlacik et al., 2008], the opposite effect was observed. This signal behavior is consistent with the expectations: When the blood flow is increased due to a higher oxygen consumption, a lower vessel contrast results. After a certain time interval, the CNR increases until the kidney has reached its equilibrium oxygenation state. Other studies showed that water diuresis led to a local T_2^* increase in the renal medulla [Nissen et al., 2010].

In this work, the sensitivity of SWI to a higher blood flow induced by an increase of the kidney function was presented. The relative contrast change could visualize the response of the veins due to a higher organ function. However, a temporal signal variation of a region affected by respiratory or bulk motion is very difficult to observe. Moreover, the high oxygenation of the kidney in the resting state [Vaupel et al., 1989] makes SWI of this organ very difficult. In conclusion, the effect of the change of the kidney oxygenation is qualitatively detectable by the SWI contrast.

6 Conclusion and Outlook

This work consists of three different parts that have one common property: For each of the presented techniques the oxygenation of the blood influences the acquired MR signal. The postprocessing of the signal allows a quantitative or qualitative determination of the local oxygen supply.

The MR signal around a spin echo can be used to determine the tissue oxygenation by means of an established tissue model. This model, derived by Yablonskiy and Haacke [1994], describes the influence of a paramagnetic vessel network on the MR signal. After the acquired data has been corrected for background inhomogeneities, the model allows a pixel-wise calculation of the OEF value in the tissue. This can be done by a three-parameter fit of the signal equation. The free parameters - the deoxygenated blood volume λ , the irreversible relaxation rate R_2 and the reversible relaxation rate R'_2 - can be determined by one signal fit. Two of these parameters, λ and R'_2 , are further used to calculate the susceptibility difference ($\Delta\chi$) between blood and tissue inside the voxels. This value enables the calculation of the OEF in the tissue. This comfortable technique comes along with a problem: The simultaneous determination of the three parameters causes a uncertainty of the single parameters. Solin [2009] showed that this method requires a very high SNR to allow reliable statements about the single parameters.

In this work, new approaches for OEF determination are presented, because the required SNR can not be achieved with the limited acquisition times for *in vivo* measurements. Here, two methods were developed that reduce the number of fit parameters of the signal equation.

The SQ-method allows a separate determination of the blood volume, that can be realized by a DSC-perfusion measurement. The number of fit parameters of the signal equation reduces to two and the fit becomes more stable, but the oxygenation can not be quantified because λ is substituted by the whole blood volume in the signal equation. Nevertheless, the results can be used to give qualitative statements, as presented in this work. Here, different regions of the brain were compared in a tumor patient measurement.

The TSC-method allows the separate determination of the fit parameters, R_2 and R'_2 . This reduces the initially three-parameter fit to a one-parameter fit of the signal equation. This method was tested in phantom measurements and a correction technique was implemented. This sequence correction was necessary because the different sequences showed a slight difference in the resulting calculated relaxation times. It was shown that the signal equation that describes the signal around a spin echo, overestimates the relaxation times R_2^* and R_2 . This has been evaluated and validated by different phantom measurements. The resulting correction method showed very reliable results for the *in vivo* data. The presented method results in one left fit parameter of the signal equation

causing an increased fit accuracy and reliable fitted parameter. The TSC-method shows very promising results for phantom and *in vivo* measurements.

As a next step, the TSC-method could be validated with the results of a PET measurement. Investigations that use FMISO as a tracer to detect tissue hypoxia [Rasey et al., 1996] seem to be appropriate, because the tracer accumulates in regions of the brain where the oxygenation level is low. Therefore, the regional oxygen supply can be illustrated and compared with the MR results. One long-term aim might be that the application of the expensive PET-technique, that suffers from the short half-life period of certain tracers (e.g. ^{15}O : $t_{1/2} \approx 125\text{s}$) and the low spatial resolution, can partially be substituted by a MR-based technique, which is cheaper, more comfortable and less harmful to health.

In the second part of the work, a recently developed technique [Bolar et al., 2009] was implemented and the influence of a VSM on linear flow was investigated with phantom experiments. The *in vivo* results show that this technique has a lot of potential but still has to be optimized with respect to patient motion. For further measurements, the head has to be fixed even better. Moreover, the number of averages (in this work: 15) has to be increased, which results in a longer acquisition time. The increase of averages can be compensated by the application of parallel image acquisition and partial Fourier. The disadvantage of these techniques is the decrease of SNR. Another possibility for improvement of the used technique is the modification of the VSM. A shorter Δ value of the encoding module would allow a shorter echo distance resulting in more acquired echoes in the same sampling time. This can be realized by shortening of the adiabatic 180° pulses and/or an increase of the encoding gradient amplitudes. However, although many improvements can be done in the future, the presented *in vivo* results look very promising.

The last part of this work shows the successful implementation of SWI at the kidney. Although radiologists identified small veins in our images, a comparison with histological data of the organ would be desirable to validate our preliminary findings. However, this is not realizable with healthy volunteers. It would be interesting to test our approach in patients, who are scheduled for kidney transplantation, and these data become available. Besides visualization of veins in the kidneys, other applications of kidney SWI are possible, like enhancement of tumors or cortical-medullary differentiation in the diagnostics of renal diseases. In summary, the results represent initial experiences with SWI of the abdomen, which proof at least the feasibility of the principle. Further research has to be performed to make this technology available for clinical abdominal MRI.

Experiments with a changing oxygenation level induced by water uptake showed that a modification of the SWI contrast is realizable and presentable by this technique. This method shows a new approach to give a qualitative statement about the tissue oxygenation.

This work shows different approaches to calculate the tissue oxygenation, which is an indicator for tissue viability. The TSC-method presents a robust technique that enables the determination of this parameter non-invasively. If this method is successfully validated with PET experiments, it possibly replaces the invasive ^{15}O PET technique used in radiotherapy for irradiation planning and therapy monitoring.

Bibliography

- A Abragam. *Principles of Nuclear Magnetism*. Oxford University Press, London, 1961.
- CB Ahn, SY Lee, O Nalcioglu, and ZH Cho. The effects of random directional distributed flow in nuclear magnetic resonance imaging. *Med Phys*, 14(1):43–48, 1987.
- H An and W Lin. Quantitative measurements of cerebral blood oxygenation saturation using magnetic resonance imaging. *J Cereb Blood Flow Metab*, 2:1225–1236, 2000.
- UI Attenberger, SP Sourbron, HJ Michaely, MF Reiser, and SO Schoenberg. Retrospective respiratory triggering renal perfusion MRI. *Acta Radiol*, 51(10):1163–1171, 2010.
- M Barth, I-M Nöbauer-Huhmann, JR Reichenbach, V Mlynárik, A Schögl, C Matula, and S Trattng. High-resolution three-dimensional contrast-enhanced blood oxygenation level-dependent magnetic resonance venography of brain tumors at 3 Tesla: first clinical experience and comparison with 1.5 Tesla. *Invest Radiol*, 38(7):409–414, 2003.
- WR Bauer, W Nadler, M Bock, LR Schad, C Wacker, A Hartlep, and G Ertl. Theory of the BOLD effect in the capillary region: an analytical approach for the determination of T2 in the capillary network of myocardium. *Magn Reson Med*, 41(1):51–62, 1999.
- G Benga and T Borza. Diffusional water permeability of mammalian red blood cells. *Comp Biochem Physiol B Biochem Mol Biol*, 112(4):653–659, 1995.
- MA Bernstein, KF King, and XJ Zhou. *Handbook of MRI Pulse Sequences*. Elsevier, 2004.
- F Bloch. Nuclear Induction. *Phys. Rev.*, 70(7-8):460–474, 1946.
- DS Bolar, BR Rosen, AG Sorensen, and E Adalsteinsson. QUantitative Imaging of EXtraction of Oxygen and TIssue Consumption (QUIXOTIC) Using Velocity Selective Spin Labeling. In *Proc ISMRM*, 2009.
- A Bongers. *Ortsaufgelöste Messung der Gewebe-Sauerstoffversorgung mittels BOLD-sensitiver MR-Bildgebung*. PhD thesis, Ruprecht-Karls-Universität Heidelberg, 2004.
- JM Bonny, W Laurent, and JP Renou. Detection of susceptibility effects using simultaneous T(2)* and magnetic field mapping. *Magn Reson Imaging*, 18(9):1125–1128, 2000.
- JL Boxerman, LM Hamberg, BR Rosen, and RM Weisskoff. MR contrast due to intravascular magnetic susceptibility perturbations. *Magn Reson Med*, 34(4):555–566, 1995.
- RN Bracewell. *The Fourier Transform And Its Applications*. McGraw-Hill, 1999.

- V Brainovich, U Sabatini, and GE Hagberg. Advantages of using multiple-echo image combination and asymmetric triangular phase masking in magnetic resonance venography at 3 T. *Magn Reson Imaging*, 27(1):23–37, 2009.
- JM Brown and AJ Giaccia. The unique physiology of solid tumors: opportunities (and problems) for cancer therapy. *Cancer Res*, 58(7):1408–1416, 1998.
- RJS Brown. Distribution of Fields from Randomly Placed Dipoles: Free-Precession Signal Decay as Result of Magnetic Grains. *Phys. Rev.*, 121(5):1379–1382, 1961.
- HY Carr and EM Purcell. Effects of diffusion on free precession in nuclear magnetic resonance experiments. *Phys Rev*, 94:630–638, 1954.
- CMJ de Bazelaire, GD Duhamel, NM Rofsky, and DC Alsop. MR imaging relaxation times of abdominal and pelvic tissues measured in vivo at 3.0 T: preliminary results. *Radiology*, 230(3):652–659, 2004.
- A Deistung, H-J Mentzel, A Rauscher, S Witoszynskyj, WA Kaiser, and JR Reichenbach. Demonstration of paramagnetic and diamagnetic cerebral lesions by using susceptibility weighted phase imaging (SWI). *Z Med Phys*, 16(4):261–267, 2006.
- G Duhamel, C de Bazelaire, and DC Alsop. Evaluation of systematic quantification errors in velocity-selective arterial spin labeling of the brain. *Magn Reson Med*, 50(1):145–153, 2003.
- HM Duvernoy, S Delon, and JL Vannson. Cortical blood vessels of the human brain. *Brain Res Bull*, 7(5):519–579, 1981.
- JO Eichling, ME Raichle, RL Grubb, KB Larson, and MM Ter-Pogossian. In vivo determination of cerebral blood volume with radioactive oxygen-15 in the monkey. *Circ Res*, 37(6):707–714, 1975.
- MA Fernández-Seara, A Techawiboonwong, JA Detre, and FW Wehrli. MR susceptometry for measuring global brain oxygen extraction. *Magn Reson Med*, 55(5):967–973, 2006.
- M Ferrari, L Mottola, and V Quaresima. Principles, techniques, and limitations of near infrared spectroscopy. *Can J Appl Physiol*, 29(4):463–487, 2004.
- B Folkow and E Neil. *Circulation*. Oxford University Press, New York, 1971.
- GB Folland. *Fourier Analysis and its Applications*. Brooks/Cole Publishing Company, 1992.
- J Frahm, A Haase, and D Matthaei. Rapid NMR imaging of dynamic processes using the FLASH technique. *Magn Reson Med*, 3(2):321–327, 1986.
- X Golay, MJ Silvennoinen, J Zhou, CS Clingman, RA. Kauppinen, JJ Pekar, and PC van Zij. Measurement of tissue oxygen extraction ratios from venous blood T(2): increased precision and validation of principle. *Magn Reson Med*, 46(2):282–291, 2001.
- DN Guilfoyle, P Gibbs, RJ Ordidge, and P Mansfield. Real-time flow measurements using echo-planar imaging. *Magn Reson Med*, 18(1):1–8, 1991.

- EM Haacke, S Lai, DA Yablonskiy, and W Lin. In vivo validation of the BOLD mechanism: A review of signal changes in gradient echo functional MRI in the presence of flow. *Int J Imag Syst Technol*, 6:153–163, 1995.
- EM Haacke, Y Xu, Y-CN Cheng, and JR Reichenbach. Susceptibility weighted imaging (SWI). *Magn Reson Med*, 52(3):612–618, 2004.
- EM Haacke, S Mittal, Z Wu, J Neelavalli, and Y-CN Cheng. Susceptibility-weighted imaging: technical aspects and clinical applications, part 1. *AJNR Am J Neuroradiol*, 30(1):19–30, 2009.
- ME Haacke, RW Brown, MR Thompson, and R Venkatesan. *Magnetic Resonance Imaging: Physical Principles and Sequence Design*. Wiley-Liss, 1st edition, 1999.
- EL Hahn. Spin Echoes. *Phys. Rev.*, 80(4):580–594, 1950.
- L Harrison and K Blackwell. Hypoxia and anemia: factors in decreased sensitivity to radiation therapy and chemotherapy? *Oncologist*, 9 Suppl 5:31–40, 2004.
- X He and DA Yablonskiy. Quantitative BOLD: mapping of human cerebral deoxygenated blood volume and oxygen extraction fraction: default state. *Magn Reson Med*, 57(1):115–126, 2007.
- X He, M Zhu, and DA Yablonskiy. Validation of oxygen extraction fraction measurement by qBOLD technique. *Magn Reson Med*, 60(4):882–888, 2008.
- M Hermier and N Nighoghossian. Contribution of susceptibility-weighted imaging to acute stroke assessment. *Stroke*, 35(8):1989–1994, 2004.
- MA Herráez, DR Burton, MJ Lalor, and MA Gdeisat. Fast two-dimensional phase-unwrapping algorithm based on sorting by reliability following a noncontinuous path. *Appl Opt*, 41(35):7437–7444, 2002.
- P Irarrazabal, CH Meyer, DG Nishimura, and A Macovski. Inhomogeneity correction using an estimated linear field map. *Magn Reson Med*, 35(2):278–282, 1996.
- H Ito, I Kanno, C Kato, T Sasaki, K Ishii, Y Ouchi, A Iida, H Okazawa, K Hayashida, N Tsuyuguchi, K Ishii, Y Kuwabara, and M Senda. Database of normal human cerebral blood flow, cerebral blood volume, cerebral oxygen extraction fraction and cerebral metabolic rate of oxygen measured by positron emission tomography with ^{15}O -labelled carbon dioxide or water, carbon monoxide and oxygen: a multicentre study in Japan. *Eur J Nucl Med Mol Imaging*, 31(5):635–643, 2004.
- P Jezzard and RS Balaban. Correction for geometric distortion in echo planar images from B_0 field variations. *Magn Reson Med*, 34(1):65–73, 1995.
- JHAM Kaanders, J Bussink, and AJ van der Kogel. Clinical studies of hypoxia modification in radiotherapy. *Semin Radiat Oncol*, 14(3):233–240, 2004.
- CA Keele, E Neil, and N Joels. *Applied Physiology*. Oxyford University, New York, 13th edition, 1982.

- VG Kiselev. On the theoretical basis of perfusion measurements by dynamic susceptibility contrast MRI. *Magn Reson Med*, 46(6):1113–1122, 2001.
- VG Kiselev and S Posse. Analytical model of susceptibility-induced MR signal dephasing: effect of diffusion in a microvascular network. *Magn Reson Med*, 41(3):499–509, 1999.
- PC Lauterbur. Image formation by induced local interactions: Examples employing nuclear magnetic resonance. *Nature*, 242:190–191, 1973.
- S Ljunggren. A Simple Graphical Representation of Fourier-Based Imaging Methods. *J Magn Reson*, 54:338–343, 1983.
- H Lu and PCM van Zijl. Experimental measurement of extravascular parenchymal BOLD effects and tissue oxygen extraction fractions using multi-echo VASO fMRI at 1.5 and 3.0 T. *Magn Reson Med*, 53(4):808–816, 2005.
- H Lu, C Clingman, X Golay, and PCM van Zijl. Determining the longitudinal relaxation time (T₁) of blood at 3.0 Tesla. *Magn Reson Med*, 52(3):679–682, 2004.
- J Ma and FW Wehrli. Method for image-based measurement of the reversible and irreversible contribution to the transverse-relaxation rate. *J Magn Reson B*, 111(1):61–69, 1996.
- P Mansfield. Multi-planar image formation using NMR spin echoes. *Journal of Physics C: Solid State Physics*, 10(3):L55–L58, 1977.
- P Mansfield. Imaging by nuclear magnetic resonance. *Journal of Physics E: Scientific Instruments*, 21(1):18, 1988.
- S Meiboom and D Gill. Modified spin-echo method for measuring nuclear relaxation times. *Rev Sci Instrum*, 29:688–691, 1958.
- I Mendichovszky, M Pedersen, J Frøkiaer, T Dissing, N Grenier, P Anderson, K McHugh, Q Yang, and I Gordon. How accurate is dynamic contrast-enhanced MRI in the assessment of renal glomerular filtration rate? A critical appraisal. *J Magn Reson Imaging*, 27(4):925–931, 2008.
- HJ Michaely, M Reichert, S Weckbach, and SO Schoenberg. Vascular and parenchymal diseases of the kidney. *Radiologe*, 48(2):185–200; quiz 201–2, 2008.
- MB Mie, JC Nissen, FG Zöllner, M Heilmann, SO Schoenberg, HJ Michaely, and LR Schad. Susceptibility weighted imaging (SWI) of the kidney at 3T—initial results. *Z Med Phys*, 20(2):143–150, 2010.
- M Molls, P Stadler, A Becker, HJ Feldmann, and J Dunst. Relevance of oxygen in radiation oncology. Mechanisms of action, correlation to low hemoglobin levels. *Strahlenther Onkol*, 174 Suppl 4:13–16, 1998.
- YE Moskalenko. *Biophysical aspects of cerebral circulation*. Pergamon Press, Oxford, 1980.

- GC Newman, E Delucia-Deranja, A Tudorica, FE Hospod, and CS Patlak. Cerebral blood volume measurements by T*2-weighted MRI and contrast infusion. *Magn Reson Med*, 50(4):844–855, 2003.
- JC Nissen, MB Mie, FG Zöllner, S Haneder, SO Schoenberg, and HJ Michaely. Blood oxygenation level dependent (BOLD)–renal imaging: concepts and applications. *Z Med Phys*, 20(2):88–100, 2010.
- H Nyquist. Thermal Agitation of Electric Charge in Conductors. *Phys. Rev.*, 32(1):110–113, 1928.
- JPB O’Connor, A Jackson, GA Buonaccorsi, DL Buckley, C Roberts, Y Watson, S Cheung, DM McGrath, JH Naish, CJ Rose, PM Dark, GC Jayson, and GJM Parker. Organ-specific effects of oxygen and carbogen gas inhalation on tissue longitudinal relaxation times. *Magn Reson Med*, 58(3):490–496, 2007.
- S Ogawa, TM Lee, AR Kay, and DW Tank. Brain magnetic resonance imaging with contrast dependent on blood oxygenation. *Proc Natl Acad Sci U S A*, 87(24):9868–9872, 1990.
- S Ogawa, TM Lee, and B Barrere. The sensitivity of magnetic resonance image signals of a rat brain to changes in the cerebral venous blood oxygenation. *Magn Reson Med*, 29(2):205–210, 1993.
- JM Oja, JS Gillen, RA Kauppinen, M Kraut, and PC van Zijl. Determination of oxygen extraction ratios by magnetic resonance imaging. *J Cereb Blood Flow Metab*, 19(12):1289–1295, 1999.
- L Pauling and CD Coryell. The Magnetic Properties and Structure of Hemoglobin, Oxyhemoglobin and Carbonmonoxyhemoglobin. *Proc Natl Acad Sci U S A*, 22(4):210–216, 1936.
- EM Purcell, HC Torrey, and RV Pound. Resonance Absorption by Nuclear Magnetic Moments in a Solid. *Phys. Rev.*, 69(1-2):37–38, 1946.
- JS Rasey, WJ Koh, ML Evans, LM Peterson, TK Lewellen, MM Graham, and KA Krohn. Quantifying regional hypoxia in human tumors with positron emission tomography of [18F]fluoromisonidazole: a pretherapy study of 37 patients. *Int J Radiat Oncol Biol Phys*, 36(2):417–428, 1996.
- A Rauscher, J Sedlacik, A Deistung, H-J Mentzel, and JR Reichenbach. Susceptibility weighted imaging: data acquisition, image reconstruction and clinical applications. *Z Med Phys*, 16(4):240–250, 2006.
- JR Reichenbach and EM Haacke. High-resolution BOLD venographic imaging: a window into brain function. *NMR Biomed*, 14(7-8):453–467, 2001.
- JR Reichenbach, R Venkatesan, DJ Schillinger, DK Kido, and EM Haacke. Small vessels in the human brain: MR venography with deoxyhemoglobin as an intrinsic contrast agent. *Radiology*, 204(1):272–277, 1997.

- JR Reichenbach, M Essig, EM Haacke, BC Lee, C Przetak, WA Kaiser, and LR Schad. High-resolution venography of the brain using magnetic resonance imaging. *MAGMA*, 6(1):62–69, 1998.
- JR Reichenbach, M Barth, EM Haacke, M Klarhöfer, WA Kaiser, and E Moser. High-resolution MR venography at 3.0 Tesla. *J Comput Assist Tomogr*, 24(6):949–957, 2000.
- BR Rosen, JW Belliveau, JM Vevea, and TJ Brady. Perfusion imaging with NMR contrast agents. *Magn Reson Med*, 14(2):249–265, 1990.
- LR Schad, G Brix, I Zuna, W Härtle, WJ Lorenz, and W Semmler. Multiexponential proton spin-spin relaxation in MR imaging of human brain tumors. *J Comput Assist Tomogr*, 13(4):577–587, 1989.
- JF Schenck. The role of magnetic susceptibility in magnetic resonance imaging: MRI magnetic compatibility of the first and second kinds. *Medical Physics*, 23(6):815–850, 1996.
- RF Schmidt and G Thews. *Physiologie des Menschen*. Springer, Heidelberg, 1995.
- SO Schoenberg, MV Knopp, M Bock, F Kallinowski, A Just, M Essig, H Hawighorst, I Zuna, L Schad, JR Allenberg, and G van Kaick. Classification of hemodynamic changes in renal artery stenosis using cine magnetic resonance phase contrast flow measurements. *Radiologe*, 37(8):651–662, 1997.
- J Sedlacik. *New Advances in Susceptibility Weighted MRI to Determine Physiological Parameters*. PhD thesis, Technische Universität Ilmenau, 2007.
- J Sedlacik, K Helm, A Rauscher, J Stadler, H-J Mentzel, and JR Reichenbach. Investigations on the effect of caffeine on cerebral venous vessel contrast by using susceptibility-weighted imaging (SWI) at 1.5, 3 and 7 T. *Neuroimage*, 40(1):11–18, 2008.
- CE Shannon. Communication in the Presence of Noise. *Proceedings of the IRE*, 37(1):10–21, 1949.
- EA Slichter. *Principles of Magnetic Resonance*. Springer, Heidelberg, 1963.
- M Solin. *Mapping of Tissue Oxygenation using Quantitative BOLD Methods: Stability under non-static conditions*. PhD thesis, Heidelberg University, 2009.
- WM Spees, DA Yablonskiy, MC Oswood, and JJ Ackerman. Water proton MR properties of human blood at 1.5 Tesla: magnetic susceptibility, $T(1)$, $T(2)$, $T^*(2)$, and non-Lorentzian signal behavior. *Magn Reson Med*, 45(4):533–542, 2001.
- GJ Stanisz, EE Odrobina, J Pun, M Escaravage, SJ Graham, MJ Bronskill, and RM Henkelman. $T1$, $T2$ relaxation and magnetization transfer in tissue at 3T. *Magn Reson Med*, 54(3):507–512, 2005.
- L Stryer. *Biochemie*. Spektrum Akad. Verlag, Heidelberg, 1998.
- P Tofts, editor. *Quantitative MRI of the Brain*. John Wiley & Sons, 2003.

- KA Tong, S Ashwal, BA Holshouser, JP Nickerson, CJ Wall, LA Shutter, RJ Osterdock, EM Haacke, and D Kido. Diffuse axonal injury in children: clinical correlation with hemorrhagic lesions. *Ann Neurol*, 56(1):36–50, 2004.
- DB Twieg. The k-trajectory formulation of the NMR imaging process with applications in analysis and synthesis of imaging methods. *Med Phys*, 10(5):610–621, 1983.
- P Vaupel and A Mayer. Hypoxia in cancer: significance and impact on clinical outcome. *Cancer Metastasis Rev*, 26(2):225–239, 2007.
- P Vaupel, F Kallinowski, and P Okunieff. Blood flow, oxygen and nutrient supply, and metabolic microenvironment of human tumors: a review. *Cancer Res*, 49(23):6449–6465, 1989.
- RM Weisskoff and S Kiihne. MRI susceptometry: image-based measurement of absolute susceptibility of MR contrast agents and human blood. *Magn Reson Med*, 24(2):375–383, 1992.
- EC Wong, M Cronin, W-C Wu, B Inglis, LR Frank, and TT Liu. Velocity-selective arterial spin labeling. *Magn Reson Med*, 55(6):1334–1341, 2006.
- DA Yablonskiy and EM Haacke. Theory of NMR signal behavior in magnetically inhomogeneous tissues: the static dephasing regime. *Magn Reson Med*, 32(6):749–763, 1994.
- DA Yablonskiy and EM Haacke. An MRI method for measuring T2 in the presence of static and RF magnetic field inhomogeneities. *Magn Reson Med*, 37(6):872–876, 1997.
- T Yamaguchi, I Kanno, K Uemura, F Shishido, A Inugami, T Ogawa, M Murakami, and K Suzuki. Reduction in regional cerebral metabolic rate of oxygen during human aging. *Stroke*, 17(6):1220–1228, 1986.
- JM Zhao, CS Clingman, MJ Närväinen, RA Kauppinen, and PCM van Zijl. Oxygenation and hematocrit dependence of transverse relaxation rates of blood at 3T. *Magn Reson Med*, 58(3):592–597, 2007.

List of Figures

2.1	Zeeman effect for a hydrogen nucleus ($I = 1/2$) in a magnetic field	8
2.2	Motion of the magnetization vector	10
2.3	Spin-lattice relaxation	12
2.4	Spin-spin relaxation	13
2.5	Lorentzian and Gaussian density of state of the magnetic field and the resulting signal decay	16
2.6	Dependency of T_2^* on T_2 and R_2'	16
2.7	Spin echo	17
2.8	Excitation of the magnetization and excitation profile	20
2.9	Slice selection I	20
2.10	Slice selection II	21
2.11	Frequency encoding	22
2.12	Shah function	25
2.13	Schematic view of the relationship between k-space and image space	27
2.14	Spin echo sequence and corresponding k-space trajectory	28
2.15	Gradient echo sequence and corresponding k-space trajectory	29
2.16	EPI sequence	30
2.17	Three contrasts in MRI	31
2.18	Heme molecule	33
2.19	Oxygen saturation curve of hemoglobin	33
2.20	Energy states of the 3d orbitals of the iron ion	35
2.21	Cortical blood vessel network recorded by an electron microscope	36
2.22	Phase dependence of different phase masks	39
3.1	Cylinder in an external magnetic field	41
3.2	Magnetic field distribution around a paramagnetic vessel with different orientations	43
3.3	MR hardware: Scanner and coils	47
3.4	Scheme of the gradient echo sampled spin echo (GESSE) sequence	47
3.5	Relaxation phantom	49
3.6	Tissue phantom	49
3.7	Flow phantom and pump	50
3.8	Calculation of ΔB	52
3.9	Signal around a spin echo	54
3.10	The effect of paramagnetic contrast agent on the MR signal	55
3.11	Dynamic susceptibility contrast	56
3.12	Experimental setup of the TSC-method	57
3.13	Velocity encoding in one dimension	58
3.14	Capillary Modeling	59

3.15	Different flow types: Plug flow and laminar flow	61
3.16	Velocity-selective module (VSM)	62
3.17	Velocity-selective spin labeling (VSSL)	63
3.18	Acquisition order of the VSSL measurement	64
3.19	Important sequence parameters	66
3.20	Modification of VSM2	67
3.21	R_2 -oxygenation-calibration curve	67
4.1	Data from the GESSE sequence	69
4.2	Magnetic field inhomogeneities: Wrapped and unwrapped phase images of the second slice	71
4.3	Phase development in two different ROIs	71
4.4	Magnetic field inhomogeneity maps for the four acquired GRE-slices	72
4.5	Gradient map calculation	72
4.6	Three-dimensional correction function	73
4.7	Parameter maps calculated with the TPF-method	74
4.8	Experimental setup, location of the ROIS and corresponding CBV and OEF histograms	76
4.9	TSC-Method	77
4.10	Parameter maps of the TSC-method	78
4.11	Data fit of the TSC-method	79
4.12	Comparison of the different sequences using the relaxation phantom	80
4.13	Underestimation of the MMGE and CPMG sequence compared to the GESSE sequence	82
4.14	Tissue phantom: Results	84
4.15	Signal decay in a ROI: Corrected TSC-method	85
4.16	Corrected parameter maps of the TSC-method	86
4.17	Flow phantom experiments	87
4.18	VSSL data acquisition	90
4.19	VSSL data postprocessing	91
4.20	Phase images and phase profiles	93
4.21	SWI postprocessing	95
4.22	Experimental setup for kidney SWI under oxygenation variation	96
4.23	Location of the ROIs for CNR calculation during oxygenation variation	97
4.24	CNR variation in time	97

List of Tables

2.1	List of different nuclei with corresponding spins, magnetic moments and gyromagnetic ratios	6
2.2	Longitudinal and transverse relaxation times for ^1H at 1.5 T	11
2.3	Water content of various human tissues	26
4.1	Measurement parameters of the TPF- and the SQ-method	70
4.2	Parameters of white matter and gray matter	75
4.3	The imaging parameters of the four sequences of the TSC-method	79
4.4	Relaxation rates in dependency of the contrast agent concentration calculated with different sequences	81
4.5	Parameters of an <i>in vivo</i> experiment before and after sequence correction	86
4.6	Signal decay due to flow rate increment	88
4.7	Sequence parameters of the VSSL sequence	89
4.8	Results of the different methods for OEF determination and corresponding acquisition times	92
4.9	SNR and CNR of the kidney measurements	96
4.10	CNR values of the two different ROIS.	97

Acknowledgment

This part I would like to write in my native language.

Ich möchte als erstes Herrn Prof. Dr. Lothar Schad danken, der es mir ermöglicht hat, die Arbeit in dieser Arbeitsgruppe durchzuführen und bei Problemen stets ein offenes Ohr hatte. Des Weiteren bedanke ich mich bei Herrn Prof. Dr. Peter Bachert, der freundlicherweise die Rolle des Erstgutachters übernahm.

Maja Solin danke ich für das Einarbeiten ins Thema und die Betreuung in den ersten Monaten, Simon Konstandin für die Hilfe bei allen möglichen fachlichen Fragen und Programmier-Problemen, Philipp Krämer für das mehrfache Ausleihen des Tobias-Phantoms.

Als nächstes möchte ich der gesamten CKM-Arbeitsgruppe für die sehr angenehme Arbeitsatmosphäre danken. Im Speziellen bedeutet dies: Ich danke Simon und Flo für die lustigen Abende in Honolulu, Stockholm und Heidelberg, Philipp für seine Massivität, Sebastian B. für die lockere Atmosphäre im kleinsten Exzellenzcluster der Welt, Sebastian D. für seine Käsebrötchen-Runde. Andi danke ich für den biexponentiellen Fit, Patrick für das Erklären der Welt, Jascha für eine einmalige Schnorchel-Suchaktion auf Maui, Fabian fürs Kickern, Christina für ihr Hautvergilbungsexperiment, Frank für das Beantworten jeglicher fachlicher Fragen und Scheuer für seinen legendären Kicker-Move.

Ich danke Axel, Belli, Lili, Reschi, Joe, Simon, Frank und Philipp für das Korrekturlesen meiner Arbeit.

Einen wichtigen Beitrag am Gelingen dieser Arbeit hatten durch ihre Anwesenheit in Heidelberg: Franzi, Axel, Silke, Joe, Reschi, Belli, Lili, Bernd, Nina, Uli (inkl. Hannes), Tobi, Maylie, Micha und viele mehr.

Nicht zu kurz kommen sollen die langjährigen Kumpels aus Kiel, mit denen der Kontakt trotz der Entfernung regelmäßig gepflegt wurde und die auch in Zukunft eine wichtige Rolle in meinem Leben spielen werden. Hervorheben möchte ich hier Jörni, Ulf, Yorck und Charly.

Ich danke Hannah und Axel und ihren jeweiligen Familien für schöne Zeiten in Kiel, Westerwohld, Freiburg und Stockholm vor und während meiner Promotionszeit.

Der größte Dank gilt meinen Eltern, die mir diese Ausbildung erst ermöglicht haben und denen ich für ihre Unterstützung und ihr Vertrauen nicht genug danken kann.